6

SCHOOL OF ENGINEERING
DUKE UNIVERSITY
DURHAM, NC 27706

CENTER FOR SOLID-STATE POWER CONDITIONING AND CONTROL

Chapters 1-4

Modeling Multiwinding Transformers for High-Frequency Applications

Part I: Analysis

Van A. Niemela, Glenn R. Skutt, Audrey M. Urling
Thomas G. Wilson, Ronald C. Wong

Prepared for Digital Equipment Corporation
Maynard, Massachusetts

July 7, 1989

Contents

Appendices

Appendices

Glossary of Symbols

The common set of symbols used throughout this report is listed in this glossary. Appearing with each symbol is its name and the page number where it is defined, discussed, or first used.

Some of these symbols appear in the text of the report in several different forms, e.g., in boldface or italic type, in upper or lower case, with or without an underline, or possibly subscripted in different ways. The form of a symbol usually conveys additional meaning beyond the basic meaning given in the table below. This additional meaning is explained in Section 1.3 or in the text where a particular form is used. As an additional aid to understanding some of the more complicated notation, examples of the different forms used with vector phasors and ratios of phasors are reviewed below.

Vector phasors such as $\underline{\mathbf{B}}$, $\underline{\mathbf{D}}$, $\underline{\mathbf{E}}$, $\underline{\mathbf{H}}$, and $\underline{\mathbf{J}}$ are directed quantities which vary in space and time as described in Section 1.3. The notational conventions associated with vector phasors are shown below for the symbol $\underline{\mathbf{E}}$, defined in the table of symbols as "electric field intensity." In Section 1.3, several different forms of this symbol are described with reference to a three-dimensional space. To understand the notation, it is helpful to keep in mind that boldface type signifies a vector with three spatial components, and an underline means "complex."

- $\underline{\mathbf{E}}$ electric-field-intensity vector phasor consisting of a phasor (complex number) in each of the three spatial coordinate directions

- $\underline{E}_y$ (complex number) phasor that is the y-directed component of the electric-field-intensity vector phasor

- $\mathbf{E}$ electric-field-intensity vector at some instant in time, consisting of three time-varying quantities, one in each of the spatial coordinate directions

- E_y (real number) y-directed component of the electric-field-intensity vector at some instant in time

- $|\underline{E}_y(x)|$ (real number) rms magnitude of the phasor that is the y-directed component of the electric-field-intensity vector phasor, as a function of x

- $\mathrm{Re}(\underline{E}_y)$ (real number) real part of the phasor that is the y-directed component of the electric-field-intensity vector phasor

Another set of notational conventions applies to ratios of phasors such as the impedance $\underline{Z}$ and the admittance $\underline{Y}$. For example, $\underline{Z}$ appears in Chapter 7 in several forms:

- $[\underline{Z}]$ complex impedance matrix
- $\underline{Z}_{34}$ complex impedance of element in 3rd row 4th column of $[\underline{Z}]$
- $[\underline{Z}']$ "referred" form of $[\underline{Z}]$
- $[\underline{Z}_r]$ "reduced" complex impedance matrix obtained from $[\underline{Z}']$
- $\underline{Z}_{r,23}$ complex impedance element of the matrix $[\underline{Z}_r]$. The element is a linear combination of short-circuit impedances involving windings 3 and 4.
- $\underline{Z}_{(34)}$ complex short-circuit impedance between windings 3 and 4
- $\underline{z}_{34}$ complex impedance element in a circuit. This symbol is not actually found in the report, but its inverse, the complex admittance element $\underline{y}_{34}$, does appear.

The table of symbols is alphabetized as follows. The relative order of two symbols is determined by the first pair of non-matching characters in the two symbols being compared. The order of the symbols is the same as the order of the two characters in an outline with the following hierarchy of headings:

1. **Alphabet:** Arabic, Greek, numerals, other characters
2. **Case:** upper, lower
3. **Style:** bold, italic, special, Roman
4. **Letter:** No next character, meaning the end of a symbol, comes before additional characters.

To form the outline, the four items in the third level "**Style:**" appear as subheadings for each of the items in the next higher level "**Case:**", and so on. According to this outline, the italicized upper-case W comes before the upper-case special character (subscript) w, which comes before the lower-case w. Greek letters follow all Arabic letters.

If a particular symbol is not found in the table, its root and subscript are probably listed separately. The page numbers refer to Part I of this report. If "Part II" is given in the page-number column, the symbol first appears in Part II of the report, and a page reference is listed instead in the glossary near the front of Part II. SI units are used throughout.

Glossary of Symbols

Symbol	*Meaning*	*Page*
A	cross-sectional area	19
AWG	American Wire Gauge	156
$\mathbf{\hat{a}_x}$, $\mathbf{\hat{a}_y}$, $\mathbf{\hat{a}_z}$	unit vectors in the reference directions x, y, and z	9
$\mathbf{B}$	magnetic flux density, a vector	A-1
$_{BASE}$	(subscript) basis value for normalizing a variable	9
b	breadth	36
b_{cu}	breadth of each conductor in a winding layer	15
b_{max}	maximum breadth available in which to place a winding	15
b_w	breadth of a winding layer	15
b_{win}	breadth of the core window; $b_{win} \geq b_{max} \geq b_w$	15
$_{bob}$	(subscript) "bobbin"	156
$_C$	(subscript) "cross-section"	31
$_c$	(subscript) "critical"	89
c.m.	units of circular mils; 1 c.m. $= 5.067 \times 10^{-10}$ m^2	156
$_{cu}$	(subscript) copper, or more generally, the conductor	15
$\mathbf{D}$	electric flux density, a vector	A-1
$_d$	(subscript) "dissipated"	56
d_{cu}	diameter of the conductor alone in a round wire	16
d_o	outside diameter of a wire, including insulation	16
$\underline{\mathbf{E}}$	electric field intensity, a vector phasor	58
$_\mathrm{E}$	(subscript) "eddy-current"	45
	(subscript) "excited-winding"	137
e	constant, 2.71828	8
F_1, F_2	dimensionless functions of Δ, where $\Delta = h_{cu}/\delta$	118
F_3, F_4	dimensionless functions of Δ, where $\Delta = h_{cu}/\delta$	123
f	frequency	72
$\underline{\mathcal{F}}$	magnetomotive force, a vector phasor	136
g_a	"additional" interlayer gap, a length used to correct the calculations	159
g_{inters}	gap between surfaces of conducting layers of adjacent winding	159
g_{intras}	gap between surfaces of conducting layers within a winding	159
g_n	gap height between winding layers n and $n+1$	147

(continued)

Symbol	*Meaning*	*Page*
$_{g_n}$	(subscript) "in interlayer gap number n"	136
$\underline{\mathbf{H}}$	magnetic field intensity, a vector phasor	53
$\mathcal{H}_{jk}$	gain of the voltage source in secondary j that is controlled by the current in secondary k	226
$H_{(jk)}$	magnetic field intensity in the z-direction with winding j excited and winding k short-circuited	133
$H_{(jk)(lm)}$	product of $H_{(jk)}$ and $H_{(lm)}$	232
HF	"high-frequency"	179
h_{cu}	height of copper in a layer of foil, strip, or equivalent rectangular conductors	15
h_t	height of insulating tape	156
I	a constant value of current, rms unless indicated otherwise by a subscript	8
$\underline{I}$	complex current phasor	8
[I]	identity matrix	216
I_j	integral expression j	G-2
$\underline{I}_m$	magnetizing current phasor	131
Im	"imaginary" operator to signify "imaginary part of ..."	67
i	instantaneous current	8
$\underline{\mathbf{J}}$	current density, a vector phasor	60
j	$\sqrt{-1}$	8
	winding number	129
	row index of a matrix	191
$_{(jk)}$	(subscript) refers to a short-circuit test where winding j is excited and winding k is short-circuited	129
K	total number of windings in a transformer	190
K_T	temperature coefficient of resistivity; $K_T = 3.93 \times 10^{-11}$ Ω-m/°C for annealed copper wire [22, p. E-88]	156
k	winding number	129
	column index of a matrix	191
$\underline{k}$	complex wave number	58
L	inductance	130
LF	"low-frequency"	179

(continued)

Glossary of Symbols (continued)

Symbol	*Meaning*	*Page*
$L_{(jk)}$	short-circuit inductance at winding j with winding k short-circuited	149
$L_{\ell n}$	leakage inductance associated with winding n	130
L_m	magnetizing inductance	130
ℓ	length	19
l	loop	34
ℓ_{gn}	"length of turn" for the interlayer gap number n	147
ℓ_m	magnetic path length	Part II
ℓ_T	length of turn in a winding layer	16
ℓ	(subscript) "layer"	16
	(subscript) "leakage"	130
M	mutual inductance	191
N_c	number of current-carrying conductors in a winding layer; $N_c = n_s N_\ell$	16
N_j	number of turns in winding j	26
N_ℓ	number of turns in one winding layer	16
$_{-N}$	(subscript) "normalized"	9
n	number of turns per meter across the breadth of a winding	37
	layer or interlayer-gap number, counted from the innermost outward	112
n_s	number of electrically-paralleled conductors with the same height coordinate	16
n	(subscript) layer number	112
oc	(subscript) "open-circuit"	130
P	power	139
$< P_D >$	average power dissipated in all the windings of a transformer	139
$P_{R(jk)}$	power dissipated in a resistance $R_{(jk)}$	139
P_n	total power dissipated in winding layer n	112
$\mathcal{P}$	permeance	Part II
p_d	power dissipated per unit volume (power density)	56
$< Q_H >$	average magnetic energy storage per square meter in the y-z plane	123

(continued)

Glossary of Symbols (continued)

Symbol	*Meaning*	*Page*
$< Q_J >$	average power dissipated per square meter of current sheet in the y-z plane	119
$< Q'_H >$	normalized average magnetic energy storage in a layer, a dimensionless function of α, β, and Δ	123
$< Q'_J >$	normalized average power dissipation in a layer, a dimensionless function of α, β, and Δ	119
R	resistance	19
	radius	31
R_c	core loss resistance	130
$R_{(jk)}$	short-circuit resistance at winding j with winding k short-circuited	149
R_{wn}	resistance of winding n	130
$_R$	(subscript) "ring"	31
$\mathcal{R}$	reluctance	24
Re	"real" operator to signify "real part of ..."	8
r	"radius" direction in a cylindrical coordinate system where a point is specified as (r, ϕ, z); distance in the radius direction	34
$_r$	(subscript) "reduced"	200
S	surface	34
S_ℓ	center-to-center distance between two adjacent layers of the same winding section	18
$S_{\ell s}$	center-to-center distance between two adjacent layers of different winding sections	18
S_s	center-to-center distance between two adjacent sections of the same winding	18
$_S$	(subscript) "secondary"	226
$_{SC}$	(subscript) "short-circuit"	8
$_{S,j}$	(subscript) "secondary j"	226
T	period of a waveform	113
	temperature	Part II
T_S	switching period	Part II
TEM	"transverse electromagnetic"	105
$_T$	(subscript) "total"	144

(continued)

Glossary of Symbols (continued)

Symbol	*Meaning*	*Page*
^{T}	(superscript) transpose of a matrix or vector	200
t	time	7
$\_(t)$	"time" as an independent variable; indicates that the preceding quantity is instantaneous or time-varying	7
$[\underline{V}_{d4}]$	vector of differential voltages $\underline{V}_{j4}$, all referenced to terminal 4	200
$\underline{V}$	complex voltage phasor	8
$\underline{V}_{jk}$	differential-voltage phasor between terminals j and k	199
V_n	volume of winding layer n	113
v	instantaneous voltage	177
	distance from $\chi = h_{cu}$, in the negative χ direction, in units of skin depth; $v = (h_{cu} - \chi)/\delta$; $v = w - \Delta$	E-3
W	energy	112
w	distance measured along the χ-axis in units of skin depth δ; $w = \chi/\delta$	117
$< W_g >$	time-average magnetic energy stored in all the interlayer gaps of a transformer	144
$W_{L(jk)}$	magnetic energy stored in an inductance $L_{(jk)}$	144
$< W_\ell >$	time-average magnetic energy stored in all the winding layers of a transformer	144
W_n	magnetic energy stored in winding layer n	112
$< W_T >$	total time-average magnetic energy stored in a transformer	144
w_m	magnetic energy stored per unit volume (energy density)	56
X_{bob}	height of the center leg of the bobbin	156
x, y, z	the three axes in a right-handed Cartesian coordinate system which correspond to the dimensions of *height*, *depth*, and *breadth* respectively; distance in the corresponding reference direction; as subscripts, a quantity in the designated direction	55
χ	(actually the Greek letter chi) variable denoting a position across the finite dimension of an infinite current sheet	66
$\underline{Y}$	admittance	190
Y_{bob}	depth of the center leg of the bobbin	156
$\underline{Y}_{jk}$	admittance element between terminals j and k of the admittance-link equivalent circuit	205

(continued)

Glossary of Symbols (continued)

Symbol	*Meaning*	*Page*
Y_o	distance across the windings in the y direction	158
y_j	expression j	F-1
$\underline{y}_{jk}$	admittance of branches or "links" in equivalent circuit	205
$\underline{Z}$	impedance	8
$\underline{Z}_{(jk)}$	short-circuit impedance with winding j excited and winding k short-circuit	149
$[\underline{Z}_S]$	coupled-secondaries equivalent-circuit impedance matrix	228
z_n	(subscript) component in z-direction in layer n	136
α	real part of the boundary-condition ratio $\underline{\Gamma}$	67
β	imaginary part of the boundary-condition ratio $\underline{\Gamma}$	67
$\underline{\Gamma}$	boundary-condition ratio; $\underline{\Gamma} = \alpha + j\beta$	67
Δ	height of a winding layer in skin depths; $\Delta = h_{cu}/\delta$	117
δ	skin depth; $\delta = \sqrt{2/\omega\mu\sigma}$	59
ε	variable which is either 1 or 0 depending upon the magnetic-field-intensity boundary conditions	68
ϵ	permittivity	58
ϵ_r	relative permittivity; $\epsilon_r = \epsilon/\epsilon_0$	A-2
ϵ_0	permittivity of free space, 8.854×10^{-12} [F/m]	58
η	layer porosity; $\eta = N_c b_{cu}/b_{win}$	22
θ	phase angle	8
Λ	flux linkage	Part II
λ	wavelength	D-8
μ	permeability	23
μ_r	relative permeability; $\mu_r = \mu/\mu_0$	A-2
μ_0	permeability of free space, $4\pi \times 10^{-7}$ [H/m]	23
ν	volume; $d\nu$ is a differential volume element	112
π	constant, 3.14159	72
ρ	resistivity in general, which could be the actual resistivity of a material or an "effective" resistivity; $\rho = 1/\sigma$	
	charge density	A-1

(continued)

Glossary of Symbols (continued)

Symbol	*Meaning*	*Page*
ρ_{cu}	resistivity of copper; for annealed copper wire: 1.7241×10^{-8} Ω-m at 20°C with temperature coefficient 3.93×10^{-11} Ω-m/°C [22, p. E-88]; $\rho_{cu} = 1.8813 \times 10^{-8} \Omega$-m at 60°C	164
σ	conductivity in general, which could be the actual conductivity of a material or an "effective" conductivity	19
σ_{cu}	conductivity of copper; $\sigma_{cu} = 1/\rho_{cu} = 5.315 \times 10^{-7}$ S/m at 60°C	164
σ_{eff}	effective conductivity; replaces the σ in the equations of Part I when calculating for equivalent-foil windings; $\sigma_{eff} = \eta\sigma_{cu}$	126
$\underline{\Phi}$	flux phasor	Part II
ϕ	instantaneous magnetic flux	24
	the angle dimension in a cylindrical coordinate system where a point is specified as (r, ϕ, z)	53
χ	variable denoting a position across the finite dimension of an infinite current sheet	66
ω	angular frequency of a periodic waveform	8
$'$	prime, the identifier for a circuit-element value which has been multiplied by a transformer turns ratio to reflect it from its original-winding location to a location in another winding circuit	195
*	(superscript) "star," meaning the complex conjugate of the preceding quantity	116
$< \_ >$	angle brackets, denoting the time average of the enclosed quantity	8
$\tilde{}$	block-partitioned matrix	216
	complex quantity	D-3

This page has been left blank intentionally.

Acknowledgments

The authors would like to acknowledge and thank several members and former members of the Center for Solid-State Power Conditioning and Control for their contributions to the research and documentation represented by this report.

First, we wish to acknowledge those former members of the research group who contributed to the writing of this report: Glenn Skutt[1] and Charles Hawkes.[2] Part I of this report, *Modeling Multiwinding Transformers for High-Frequency Applications: Analysis*, incorporates many ideas and figures plus some text originally presented in the Master's Thesis, *Modeling Multiwinding Transformers for High-Frequency Applications*, by Glenn Skutt. Glenn's work laid the cornerstone for much of the research presented in this report. As part of his master's degree work, Charles Hawkes wrote Sections 4.3 and 4.4, Appendix D, and the computer program which generated the phasor distribution plots of Chapter 4. In addition, he oversaw revisions to Sections 4.1 and 4.2 and Appendices A, B, and C of Part I, and coauthored a paper for the 1989 Power Electronics Specialists Conference which is included as Appendix K of Part I.

Second, we wish to acknowledge those persons whose contributions have been primarily toward the research presented in this report and to the mechanics of producing this document: Yain-Nan Chang[3], Dr. Harry A. Owen, Jr., and Margrid Krueger. The acquisition of most of the laboratory data presented in this report was carried out by Yain-Nan (Steve) Chang. Steve wrote the computer program to generate the calculated short-circuit impedance data presented in Chapter 6, and spent numerous hours in the Macintosh cluster drawing and revising figures. A special thanks goes to Dr. Owen whose advice on the laboratory measurements and on the interpretation of the resultant data were invaluable. Lastly, we wish to thank our administrative assistant, Margrid Krueger, for her LaTeX advice and expertise and for her time spent generating the various versions of this report.

Additionally, we would like to thank Dr. Anil K. Ohri and Dr. Joseph V. Thottuvelil of Digital Equipment Corporation for their guidance and direction in the conduct of this research, and to Mr. P. S. Venkatraman for consultation on many of the fine points of magnetics and for providing numerous sample transformers for testing and evaluation.

---

[1]Now with Digital Equipment Corporation, Northboro, MA.
[2]Now with Harris Corporation, Melbourne, FL.
[3]Now with Deltron, Inc., North Wales, PA.

This page has been left blank intentionally.

Chapter 1

Introduction

There are many advantages to using high excitation frequencies in power conditioning circuits. One of the most important of these advantages is the reduction in transformer size that can be achieved as the frequency increases. Other benefits which are not related to the transformer magnetic structure include a decrease in the size of output filter inductors and capacitors, faster output response to changes in input voltage, and easier filtering of radiated switching noise.

High-frequency excitation clearly has advantages in power conditioning circuits, but as with all things there must also be associated drawbacks. In this case, the drawbacks arise due to the so-called skin and proximity effects which cause the currents in the transformer windings to distribute unevenly over the cross-sectional areas of these windings. The results of these redistributions of current are an increase in the copper losses in the windings of the transformer and a reduction in the magnetic energy stored in the window of the transformer core.

The increase in the copper losses in the transformer windings appears in a circuit as an increase in the resistance of each of the transformer windings. This increase in the apparent winding resistance is often referred to as *ac winding resistance* and is a deleterious effect that results in more power dissipation in a winding that carries a given current. The increased power dissipation translates into an increase in the heat generated in the winding space. This increased thermal stress can affect the performance of the transformer enough to outweigh other advantages of high-frequency operation; in fact, the thermal problems related to high-frequency winding losses can place an upper limit on the frequency that can be used in a given device. Since transformer performance is so heavily influenced by dissipative loss, the quantification of ac winding resistance effects has been the major focus of most of the recent work that has appeared concerning the high-frequency operation of transformers.

The reduction of the amount of magnetic energy in the transformer window area that results from high-frequency excitation can be related to a corresponding decrease in the inductance of the various windings of the transformer. This winding inductance is often referred to as transformer *ac leakage inductance*. We must be clear however that the concept of leakage inductance or more specifically leakage flux is defined only as leakage *between two windings.* There is no way to designate what the leakage inductance of a winding is in and of itself, but rather this must always be defined in reference to some other winding. In this report we refer to the inductances associated with the leakage flux between any two windings as the reactive component of the leakage *impedance* between the two windings.

The reduction of magnetic energy in the transformer window area is a more benign and generally a more beneficial phenomenon than the corresponding increase in apparent winding resistance. It has not, therefore, received a great deal of attention in the literature. However, this inductance of transformer windings warrants closer examination. At sufficiently high frequencies the winding inductance may interact with other stray elements in the circuit and significantly affect the circuit operation. In certain types of circuits such as quasi-resonant switching converters, this is a desirable and important interaction.

In other applications, however, the inductances in the windings cause undesirable effects. Such a situation exists in the multioutput voltage regulator where the inductances in the secondary windings of a multisecondary transformer create cross-regulation problems that impact the steady-state output voltages that appear on unregulated outputs. The analysis presented in this report is aimed more toward quantifying these cross-regulation effects than toward describing the interaction between transformer winding inductances and other parasitic circuit parameters. The focus of this analysis influences many of the assumptions used in deriving a suitable model for multiwinding transformers with high-frequency current excitations.

1.1 OVERVIEW OF THE REPORT

This report is divided into two separate parts: *Part I: Analysis*, and *Part II: Literature Review.* The document you are reading currently is *Part I: Analysis.* Throughout the rest of this report *Part I: Analysis* is called "Part I" or "Part I of this report" and *Part II: Literature Review* is called "Part II" or "Part II of this report." Part I of this report deals primarily with deriving the field solution to determine the redistribution of currents in high-frequency transformer windings and how this redistribution affects the power dissipation and energy storage of the transformer windings. It is designed to aid the reader's understanding of high-frequency effects in transformer windings and to provide the reader with simple equivalent circuits for the transformer which account for these effects. Part II of this report is an in-depth review of several important articles pertaining to high-frequency transformer windings and describes the strengths, weaknesses and significant contributions of each article. It is designed to aid the reader's comprehension of the reviewed articles.

1.1.1 Overview of Part I of the Report

Part I of this report provides a means by which the impedances which characterize a multiwinding transformer can be calculated for high-frequency sinusoidal excitations. The general aim of this analysis is to replace laboratory measurements of transformer characteristics with calculated values that are based on the geometry of the transformer and the excitation conditions in the transformer windings. The results of such an analysis hopefully will provide the foundation for determining via computer simulation the interactions between the various windings of a multiwinding transformer. The ability to simulate the behavior of a given transformer design without actually building the device should prove useful in the design of multiwinding transformer circuits for use in high-frequency applications.

Another and perhaps equally significant purpose of Part I of this report is to review critical concepts of high-frequency transformer analysis and to familiarize the reader with the set of assumptions that are used in such an analysis. This should provide the reader with the tools necessary to understand similar derivations presented in recently published articles such as [19]. In deriving the full solution for the field distribution in an infinite current sheet used to model a transformer winding layer, Part I of this report fills in many of the details that are often left out of shorter journal articles. The mathematical detail presented herein should allow the reader to follow the trail of analysis without having to derive the intermediate steps and should aid the reader's understanding of the journal articles discussed in Part II. Also, the sections on modeling an actual transformer winding structure should provide a guideline for applying these results to specific transformers. At the outset of the solution for the fields associated with the transformer winding space, certain assumptions are made and the winding layers of the physical transformer are replaced by infinite current sheets to make the solution tractable. At the conclusion of the field solution, two equivalent circuits are proposed to model the transformer's behavior in an electrical system.

1.1.2 Goals and Assumptions of Part I

Generally it is very difficult if not impossible to calculate the leakage impedance values between transformer windings, so the measurement of these parameters in the laboratory is usually the only reasonable alternative. This is rather inconvenient to the design engineer who would like to predict the performance of a certain transformer design without first building the device. In addition, the dependency of the leakage impedances of a transformer on the excitation conditions that exist in the windings means that it is usually not sufficient to measure the transformer characteristics only once; rather, the measurements must be performed over the expected range of harmonics for the excitation waveform.

The goal of Part I of this report, therefore, is to develop appropriate methods for calculating the values of the various winding impedances of a multiwinding transformer based on the geometry of the winding structure and the winding excitation conditions.

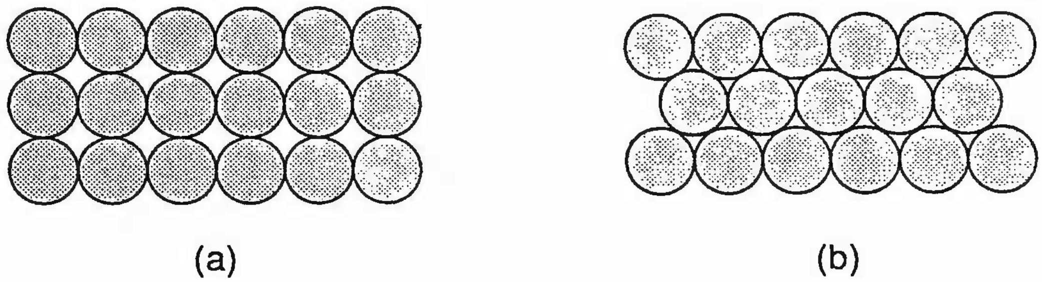

Figure 1.1: Definition of winding arrangements (a) square and (b) hexagonal [17, page 338].

To accomplish this goal, we must make several simplifying assumptions about the transformer that allow us to analyze the magnetic field distribution in and around the windings of the transformer in a single dimension. The main assumption that we use to perform such a one-dimensional analysis—indeed it is with the purpose of allowing this one assumption that other approximations are made—is that throughout the winding space of a pot- or EE-core transformer, the magnetic leakage flux is parallel to the surfaces of the various layers of conductors that comprise the transformer windings. We specify our assumptions and define the geometry of the winding structures in detail later in this report. We make no attempt in this report to address the variations of the magnetic fields in the windings in more than one dimension.

In this report, we are interested only in the high-frequency behavior of the transformer windings. No attempt is made to model core loss, nor analyze the frequency dependence of core loss. Rather, it is assumed that the magnetizing current of the transformer core is negligible and that the core appears to be ideal, i.e., it is lossless and stores no energy. Also, the analysis presented herein predicts only the apparent winding resistances and leakage inductances of the transformer windings. Throughout this analysis, capacitive effects caused by voltage gradients between adjacent conductors are ignored. For the frequencies of interest, this does not seriously affect the agreement between the measured transformer impedances and the predicted values as is shown in Chapter 6. At higher frequencies though, capacitance in the transformer windings will cause the measured and predicted values to diverge.

For the analysis presented in Part I of this report, certain assumptions are made about the configuration of the windings in the transformer window. It is assumed that winding layers are arranged in a "square" configuration as in Fig. 1.1(a) rather than a "hexagonal" arrangement as in Fig. 1.1(b). Hence, turns from one layer are not permitted to sink into the spaces between the turns of an adjacent layer. Likewise, it is assumed that transformer winding layers contain only conductors of one transformer winding. Bifilar windings, where wires from two separate windings are wound simultaneously, are not considered. However, no restriction is placed on the relationship between the conductors in adjacent layers, and conductors of the same winding may be paralleled and wound simultaneously.

The analysis presented in this report is based solely on sinusoidal-current-excitation conditions in the windings of a transformer. Nonsinusoidal-current excitations can be accommodated by applying Fourier analysis to the nonsinusoidal waveforms. Such Fourier analysis is discussed in [2,19,20],[1] but we do not examine it any further in Part I. From the purely sinusoidal analysis, we derive expressions for the resistance and inductance values between two windings and then use these results in two different equivalent-circuit models of a multiwinding transformer. These circuit models are intended to be used in a circuit simulation tool such as SPICE for predicting the behavior of a multiwinding transformer under load. We have not performed such simulations and we can make no claim about the adequacy of the equivalent-circuit models discussed in this report.

The assumptions used in the analytical development limit the applicability of the results. Although measurement verification for different transformers operated under various excitation conditions is not complete, the analysis should apply to transformers wound on pot- or EE-core structures. Of particular interest are multiwinding transformers for use in multioutput dc-to-dc converters with PWM control. It should be stressed that the fundamentals of the analysis techniques employed here can be found in many early references on transformer analysis; however, the particulars of the analysis are adapted toward predicting and modeling the effects of high-frequency current excitations on the leakage impedances of multiple-winding transformers.

We should remember that the analysis of transformers and the calculation of transformer device characteristics is one of the oldest and most thoroughly investigated topics in electrical engineering. The reader should recognize that many of the ideas and solutions that are addressed in Part I were investigated in much earlier work. The primary advantage that the present analysis enjoys that earlier works could not incorporate is computer calculation of complex magnetic field equations. In essence, the major contribution of the following analysis is our ability to calculate and display the distributions of magnetic energy and current density inside a transformer winding space, thus increasing the reader's understanding of high-frequency effects in transformer windings.

1.2 OUTLINE OF ANALYTICAL STEPS PRESENTED IN PART I

In Chapter 2, we show how an actual transformer winding structure can be converted into the geometrical model of a transformer that we use in the analysis of Chapter 4. This chapter concentrates on the definition of certain winding parameters and provides detailed explanations for terms encountered in the rest of this report and in recently

[1] We list all references in Part I of this report alphabetically. See the bibliography for the specific reference.

published articles. In addition, Chapter 2 addresses the term *leakage flux* and what is meant by this term throughout this report.

Chapter 3 sets up the problem we address in the analytical development of later chapters. In this chapter, we initially assume that we can model the transformer as a multilayer, infinitely long solenoid. We then describe the magnetic-field-intensity distribution that exists in a two-layer infinite solenoid when the currents in the windings are constant or varying at low-frequencies. Following the development of the low-frequency field distribution in the solenoid, we discuss the effect that time-varying magnetic fields have on conductors in general. This discussion provides detailed qualitative explanations of both the skin and proximity effects that occur in the conductors of the transformer windings. Following this general discussion of the eddy-current effects in conductors, we introduce the infinite current sheet as an approximate representation of the infinitely long cylindrical conducting layers of the infinite solenoid. We conclude Chapter 3 by setting up the geometry of the current sheet which we proceed to analyze in Chapter 4.

Chapter 4 presents the bulk of the mathematical work in this report. In this chapter, we begin with Maxwell's field equations and apply them to the infinite current sheet under sinusoidal field variations. From these equations, we derive one-dimensional differential equations for the magnetic field intensity and current density inside a current sheet. We then solve these differential field equations to determine expressions for the distribution of magnetic field intensity and current density as functions of excitation frequency and the values of the magnetic field intensity on the boundaries of the sheet. An extensive number of plots are presented in this chapter to illustrate the impact of the skin and proximity effects on the distribution of the magnetic field intensity and current density in the conducting layers. The remainder of Chapter 4 shows how these two field distributions are used to calculate the power dissipated and energy stored in any winding layer.

Chapter 5 takes the general expressions for the power dissipated and energy stored in any winding layer, developed in Chapter 4, and applies them to the calculation of the apparent resistance and inductance for transformer windings under specific hypothetical short-circuit tests. The low-frequency field-intensity diagrams developed in Chapter 3 are used to determine the boundary conditions of field intensity for each layer in the winding space. The boundary conditions are used with the layer-based expressions of Chapter 4 to determine the total dissipated power and energy stored in the winding space. Finally, the total power loss and energy stored are represented in an equivalent circuit by a resistor and an inductor, respectively.

An example calculation of the short-circuit resistance and inductance for an actual transformer at a specific frequency is presented in Chapter 6. This chapter takes the reader through the steps necessary to determine these values given the geometry of the transformer winding and the specific short-circuit excitation. Many of the more important concepts of the previous chapters are recapitulated in Chapter 6 and clarified by use. Calculated short-circuit resistance and inductance data are plotted versus frequency and compared with measured data to demonstrate the validity of the analytic results.

Two equivalent circuits which fully characterize a four-winding transformer for sinusoidal excitation at a specific frequency are the subjects of Chapters 7 and 8. The elements of these equivalent circuits are determined using the short-circuit impedances calculated using the expressions derived in Chapter 5. Chapter 7 focuses on the admittance-link model which is also discussed in [1,13,18]. At the beginning of Chapter 7, we review the general K-port-network description of a transformer with K windings and express the winding voltages and currents using port voltages and currents of the K-port network. This K-port network description is used to derive expressions for the admittance-link-circuit elements in terms of the transformer short-circuit impedances. Chapter 7 concludes with a sample calculation of the admittance links for the example transformer used in Chapter 6. Chapter 8 focuses on a coupled-secondaries equivalent circuit which is an extension of a model proposed by Rosa in [15]. The relationship between the admittance-link model and the coupled-secondaries model and the relative merits of each are also discussed in Chapter 8.

Finally, Chapter 9 reviews some of the major assumptions made in this analysis, and provides some general guidelines for reducing the leakage impedances of multiwinding transformers. In this chapter we also comment on the future prospects for the application of the type of analysis presented here.

The analysis methods presented in this report have been summarized in two papers which are to be presented at the 1989 Power Electronics Specialists Conference. Preprints of these papers are included in this report as Appendices J and K.

1.3 NOTATIONAL CONVENTIONS USED IN THE REPORT

While writing Parts I and II of this report, a consistent set of symbols and nomenclature was adopted by the authors. A summary of these symbols and their definitions appears in the Glossary of Symbols which is located immediately after the Table of Contents. Throughout this report, all quantities are presented in SI units. The adopted nomenclature is defined throughout the text of Part I but primarily in Chapter 2. To cue the reader on the specific usage of the adopted symbols, certain notational conventions are used throughout Parts I and II of this report.

Variables that represent time-varying density functions are given lower case symbols, as shown below. The corresponding total time-varying variables resulting from integrating these density functions over space are given upper case symbols. For these variables, the case of the subscript follows no convention and is defined upon the first use of the variable. The time-varying nature of these functions is emphasized by the presence of (t) in the variable. Examples are:

- $p_d(t)$: instantaneous power dissipated per unit volume (power density)
- $w_m(t)$: instantaneous magnetic energy stored per unit volume (energy density)
- $P_n(t)$: total instantaneous power in the n^{th} layer of a transformer

- $W_g(t)$: total time-varying energy stored in the interlayer gaps

The time average value of any of these variables is represented by enclosing the symbol in angle brackets $\langle\,\rangle$. An example of this is $\langle p_d \rangle$, the time-average power density at a point.

With the above density functions as an exception, a time-varying quantity is generally designated as a lower-case variable with an upper-case subscript, and the corresponding time-average variable is given in angle brackets. For example, i_{SC} or $i_{SC}(t)$ might represent the instantaneous current under short-circuit (SC) conditions, and $\langle i_{SC} \rangle$ represent the time-average short-circuit current. Variables that refer to rms values of currents or voltages are written in upper case with an upper-case subscript. For example, an rms current in a short-circuited transformer winding is designated I_{SC}.

In the special case of sinusoidally varying waveforms, time-varying quantities may alternatively be written using phasor notation. Phasor notation is a shorthand notation used to represent the magnitude and phase information of a sinusoidally varying quantity. A phasor is a complex number with a magnitude equal to either the peak value or the rms value of a sinusoidal waveform and a phase angle that corresponds to the difference in phase between the particular time-varying quantity and some chosen sinusoidal reference. *In this text, we choose the magnitude of a phasor quantity to be equal to the rms value of the sinusoidally varying quantity that it represents.* We designate phasor quantities as upper-case letters with an underline. For example, the symbol $\underline{I}_{SC}$ denotes the phasor for the sinusoidally varying short-circuit current $i_{SC}(t)$. A phasor can be written as a complex number in terms of its real and imaginary components, or in terms of its magnitude and phase angle. In the latter case, called the polar form, two conventions are commonly encountered—either $\underline{I}_{SC} = I_{SC}\angle\theta$ or $\underline{I}_{SC} = I_{SC}\, e^{j\theta}$—where the magnitude of the phasor, which in this report is equal to the rms value I_{SC} of the sinusoid, is followed either by the angle symbol $\angle$ and the phase angle θ or by the expression $e^{j\theta}$. Phasor quantities are converted from polar to rectangular form using the Euler identity

$$e^{j\theta} = \cos\theta + j\sin\theta \tag{1.1}$$

Phasor quantities are transformed into their corresponding time functions by multiplying the phasor by the time function $e^{j\omega t}$, then taking the real part (for the case of a cosinusoidal reference function) and multiplying the result by $\sqrt{2}$. That is,

$$\begin{aligned} i_{SC}(t) &= \sqrt{2}\,\mathrm{Re}(\underline{I}_{SC}\, e^{j\omega t}) \\ &= \sqrt{2}\,\mathrm{Re}(I_{SC}\, e^{j\theta}\, e^{j\omega t}) \\ &= \sqrt{2}\, I_{SC}\cos(\omega t + \theta) \end{aligned} \tag{1.2}$$

In addition to being used in the symbols for phasor quantities, underlines are used to denote all complex variables. This includes any complex numbers that are the ratio of phasor quantities which are written as upper case letters with an underline. An example of this is an impedance that is determined from the ratio of a phasor voltage $\underline{V}$ and a phasor current $\underline{I}$. For this case, we write $\underline{Z} = \underline{V}/\underline{I}$.

Another notational convention in this report is the use of boldface characters to designate vector quantities. An example of this is $\mathbf{E}(x, y, z, t)$ which is the three-dimensional time-varying vector electric field. If this electric field is varying sinusoidally in time, then we can combine the phasor and vector notations and write

$$\mathbf{E}(x, y, z, t) = \sqrt{2}\,\mathrm{Re}(\underline{\mathbf{E}}(x, y, z)e^{j\omega t}) \tag{1.3}$$

where $\underline{\mathbf{E}}(x, y, z)$ is a vector phasor quantity. This vector phasor can be written in terms of its phasor components as

$$\underline{\mathbf{E}}(x, y, z) = \underline{E}_x\hat{\mathbf{a}}_\mathbf{x} + \underline{E}_y\hat{\mathbf{a}}_\mathbf{y} + \underline{E}_z\hat{\mathbf{a}}_\mathbf{z} \tag{1.4}$$

where $\underline{E}_x$ can be expressed as $E_x\angle\theta_x$ or $E_x e^{j\theta_x}$ and can be a function of x, y and z. In the text of this report, the explicit argument dependence of a vector quantity is sometimes dropped if the vector nature of the quantity is clear. For example, in writing Maxwell's equations, we may write $\nabla \times \mathbf{E} = -\partial\mathbf{B}/\partial t$ where the spatial and time dependencies of $\mathbf{E}$ and $\mathbf{B}$ are understood.

Finally, an expression that represents a normalized value is written with an additional N subscript appended, if necessary, by a hyphen to any preexisting subscript. For example, the magnetic field intensity in the n^{th} layer $\underline{H}_{z_n}(x)$ can be normalized to some base value $\underline{H}_{BASE}$, to yield the normalized field intensity for the layer $\underline{H}_{z_n\text{-}N}(x) = \underline{H}_{z_n}(x)/\underline{H}_{BASE}$.

This page has been left blank intentionally.

RidleyWorks® Lifetime License

- Power Stage Designer
- Power Stage Waveforms
- Magnetics Designer
- Transfer Function Bode Plots
- Closed Loop Design
- Automated FRA Control
- LTspice® Automated Link
- PSIM® Automated Link

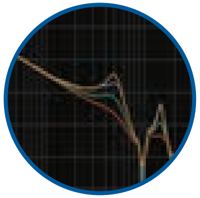

4-Channel Frequency Response Analyzer

- Frequency Range 1 Hz - 20 MHZ
- Source Control from 1 mV - 4 V P-P
- Built-In Injection Isolator
- Bandwidth 1 Hz - 1 kHz
- Automated Setup from RidleyWorks®
- Direct Data Flow into RidleyWorks®

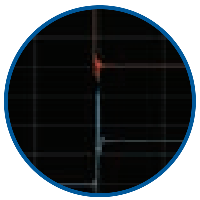

4-Channel 200 MHz Oscilloscope

- Picoscope® 5444D 4-Channel Oscilloscope
- 200 MHz Bandwidth
- 1 GS/s at 8-bit res; 62.5 MS/s at 16-bit res
- Signal Generator up to 20 MHZ
- Computer Controlled

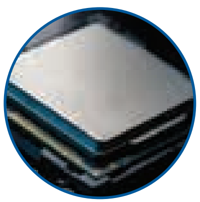

Embedded Computer

- Intel® Computer with 32 GB RAM, 256 GB SSD
- Intel® HD Graphics 620
- Integrated Dual Band Wireless, Bluetooth 4.2
- Dual HDMI and USB Ports, Ethernet

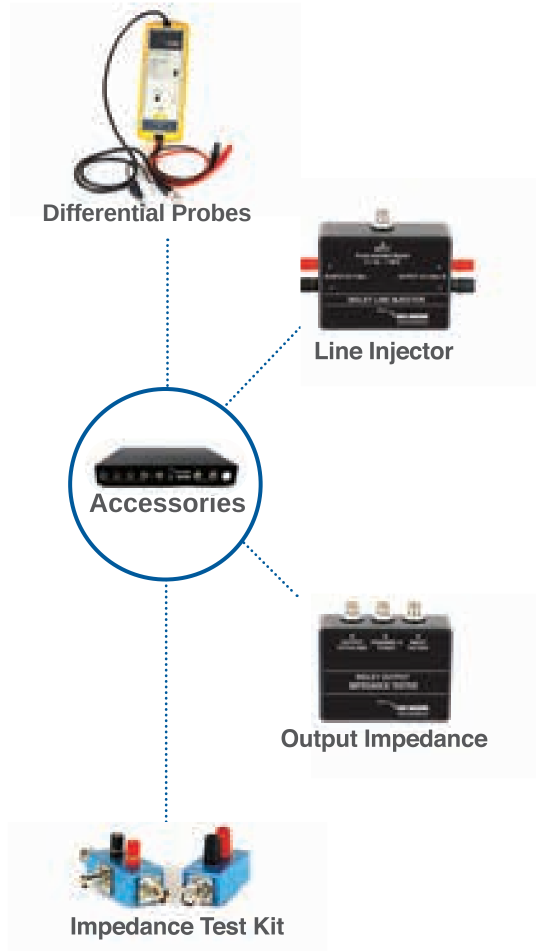

Chapter 2

Deriving a Model Transformer Structure From An Actual Transformer Winding Arrangement

Any analysis of high-frequency effects in transformer windings must, of course, begin with a determination of the fields in and around the windings which is based upon Maxwell's equations. Before this can be done though, certain assumptions must be made so that the transformer windings can be modeled and the field solution made tractable. Also, a set of terminology must be adopted to facilitate discussion of the transformer windings and any resultant model. In this chapter, we demonstrate the techniques and terminology used to transform an actual winding structure that consists of round wire, rectangular conductors, or foil windings into a model structure which we use in subsequent chapters that contains only equivalent foil conductors which extend across the full breadth of the core window. We also examine two aspects of leakage flux and clarify what is meant by this term in subsequent chapters.

2.1 EXAMPLE WINDING STRUCTURES

The key to the transformer analysis presented in this report lies in the geometry and layout of the transformer winding structure. Therefore, it is important to state clearly what types of devices are addressed here and to define clearly a set of variables that can be used in the analytical expressions. Much of the published work that addresses the issue of ac winding impedances uses somewhat conflicting terminology when referring to both transformer geometry and winding parameters. In the following discussion, we choose a single set of definitions and conventions to refer to the magnetic structures. Some terms are taken directly from the literature where a relatively clear consensus

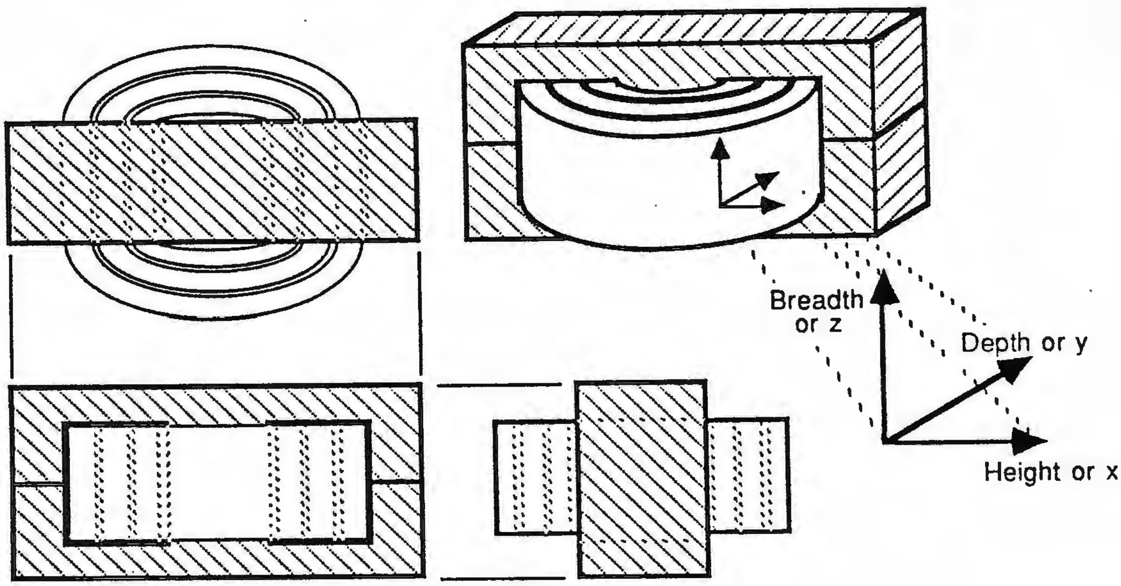

Figure 2.1: Wound EE-core transformer with shell windings.

exists among several authors. Where no such clear agreement exists, we pick a suitable symbol and use this symbol throughout our discussion. Not all of the symbols that we define in this chapter are necessarily used in any calculations given in this report. The justification for providing the specific and detailed definitions for all geometrical quantities is that such definitions should prove useful in the future for such pursuits as developing any type of computer program for the analysis of devices such as those examined in this report. For ease of reference, the symbols defined within this chapter and in later parts of this report have been collected in the Glossary of Symbols which follows the Table of Contents.

2.1.1 Transformer Configuration of Interest

The focus of our analysis is transformers with windings that are wound on pot cores although it is our opinion that the analysis is equally valid for EE cores such as those shown in Fig. 2.1. A transformer of the type shown in Fig. 2.1 has windings which form concentric cylindrical "shells" with the outer layers of wire completely surrounding the inner winding layers. Such a structure is referred to as a shell transformer in [13], and we shall use that designation in the discussion which follows. In a shell winding arrangement, the flux in the window of the transformer is assumed to be parallel to the axis of the winding. This leakage flux pattern is shown for an example transformer in Fig. 2.2.

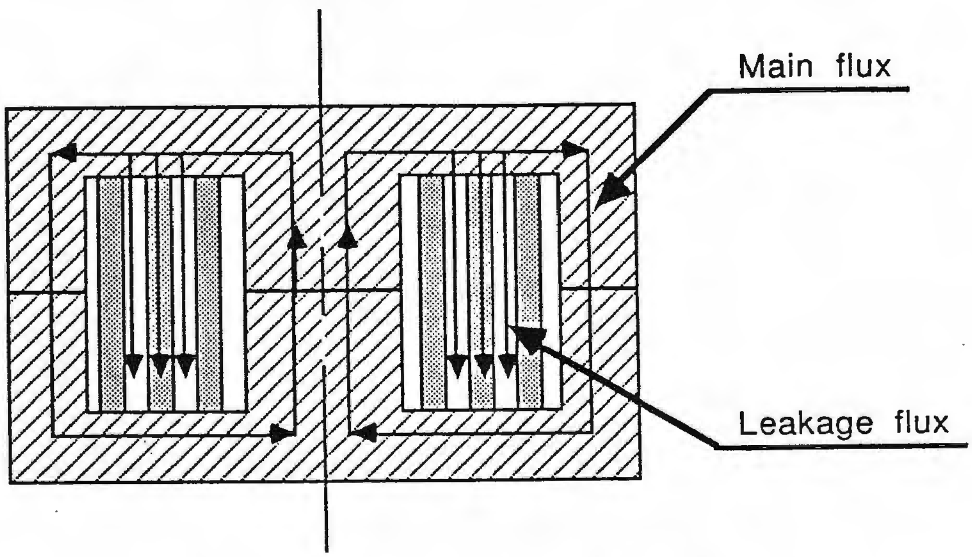

Figure 2.2: Window flux pattern in a shell winding structure.

2.1.2 Dimension Directions

The coil dimensions shown for the winding structure of Fig. 2.1 employ the following conventions:

- The **breadth** direction is in the same direction as the flux in the transformer window. For a shell winding structure, this direction is parallel to the axis of the center leg of the core. This is later referred to as the z-axis direction. This convention is indicated in Fig. 2.1.

- The **height** direction is normal to the direction of the flux in the window of the transformer and in the direction of the buildup of the windings. For the shell windings in Fig. 2.1, the height direction is normal to the core center leg. The height direction is later referred to as the x-axis direction. Figure 2.1 shows the height direction definition for the structure.

- The **depth** direction is always normal to the plane of the core window and is later referred to as the y-axis direction.

Figure 2.3 shows the cross section of the core and windings of a shell winding structure in greater detail. In this figure, there are three different types of windings illustrated. The innermost winding is made up of insulated round wire as shown in the upper detailed view of the winding. The center winding consists of insulated rectangular wire or insulated "strip conductor" as shown in the left-side detailed view; and the outermost winding is made of foil. The following definitions and features of this figure are of importance and

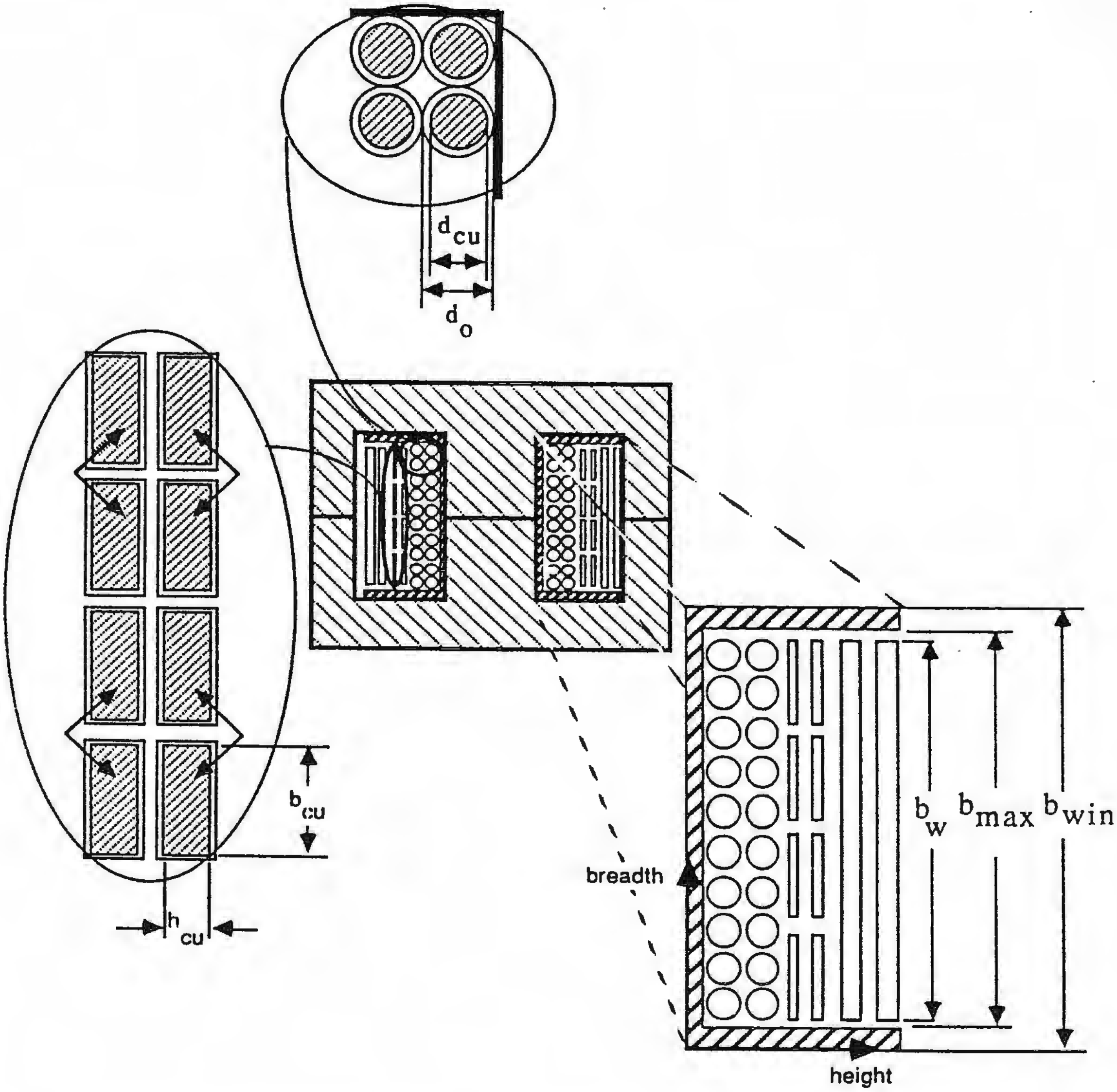

Figure 2.3: Detailed view of the cross-section of an EE-core transformer with shell windings. The innermost winding is made up of insulated round wire as shown in the upper detailed view of the winding. The center winding consists of insulated rectangular wire as shown in the left-side detailed view; and the outermost winding is made of foil.

should be clearly understood before proceeding to model the transformer for analysis purposes.

2.1.3 Definition of Winding Geometry Terms

Winding layer: A conductor or set of conductors that occupy the same window-height position is called a winding layer. This could also be stated as any set of conductors that are collinear in the direction of breadth.

Multi-conductor winding: Any winding that is wound so that more than one separately insulated but electrically paralleled conductor occupies the same window-height position is said to be a multiple-conductor winding. If the middle winding of the winding structure shown in Fig. 2.3, for example, were fabricated as a four-turn winding where two side-by-side conductors at the same window height were connected electrically in parallel, then this would be a two-conductor winding. This situation is indicated by the arrows in the left-side detailed view. The arrows point to electrically paralleled conductors. The term multi-conductor winding does not refer to Litz wire windings or to twisted-strand windings which are not considered in Part I of this report; these types of windings are discussed briefly in [2,11,12,20].

The following symbols are defined with respect to the drawing of Fig. 2.3:

b_{win} = the breadth of the core window itself.

b_{max} = the maximum breadth available in which to place a winding. This dimension is limited by a bobbin or a winding former or by the core itself. In the latter case, $b_{max} = b_{win}$.

b_w = the breadth of a winding layer. This is the actual physical extent of a winding layer including the insulation on the conductors. It cannot exceed the maximum available winding breadth b_{max} as shown in Fig. 2.3.

b_{cu} = the breadth of each of the copper conductors in a winding layer. For a foil conductor such as used in the outermost winding in Fig. 2.3 or a rectangular conductor such as used in the center winding, b_{cu} is simply the breadth of the conductive material in the foil or the rectangular wire. This does not include any insulation on the conductor. For round conductors, b_{cu} is computed by considering each round wire in the winding layer to be equivalent to a square conductor of equal cross-sectional area as discussed in detail later in connection with Fig. 2.5.

h_{cu} = The height of copper in a winding layer. For a foil conductor such as used in the outermost winding in Fig. 2.3 or a rectangular conductor such as used in the center winding, h_{cu} is the height of the conductive material in the foil or the rectangular wire. This does not include any insulation on the conductor. For round conductors, h_{cu} is computed by considering each round wire in the winding layer to be equivalent to a square conductor of equal cross-sectional area as discussed in detail later in connection with Fig. 2.5.

d_o = the outside diameter of a round wire. This includes wire insulation.

d_{cu} = the diameter of the copper alone in a round wire.

ℓ_T = the length-of-turn of the layer. Often called the mean length-of-turn because it is calculated using the center of the layer in the x-direction, this value depends upon the actual shape of the windings of any particular transformer. Also, it is often assumed that the length-of-turn for each layer can be approximated by the length-of-turn for an entire winding or for an entire winding structure.

N_ℓ = the number of turns of winding wire in a winding layer. For a foil conductor winding, $N_\ell = 1$. For other winding types, N_ℓ is always the number of *turns* of the winding that have the same height coordinate.

N_c = the number of current-carrying conductors in a winding layer. The number of conductors in a layer may be the same as, or an integer multiple of the number of turns in a layer N_ℓ.

n_s = the number of electrically paralleled conductors in a multi-conductor winding.[1] In the cross-section shown in Fig. 2.3, the rectangular-conductor winding has two conductors per turn (i.e., $n_s = 2$). This is indicated by the connected arrows that point to the electrically paralleled conductors in the detailed view of the winding at the left of the figure. In terms of the above definitions, we can write $N_c = n_s N_\ell$. We assume throughout Part I of this report that the n_s electrically paralleled conductors each carry the same amount of current, i.e., they share the winding current equally.

There are other features of the windings yet to be defined, but for this we need another figure. Figure 2.4 shows a shell winding transformer with three windings. One winding is of foil conductors and consists of the inner three layers plus the sixth layer. A second winding consists of two layers of round wires, layers number four and five; and a third winding consists of the outermost layer of round wire. From Fig. 2.4, we can define the concepts of winding section, build, layer spacing, and section spacing.

Winding section: A winding section is any set of layers of a particular winding that are located next to each other with no layers of other windings separating them. If all the layers of a winding are physically next to each other then there is only one winding section for that winding. In Fig. 2.4 we see that the winding composed of foil layers has two winding sections, whereas each of the round-wire windings has only one section. The maximum number of winding sections a winding can have is equal to the number of layers in the winding.

[1]Multi-conductor windings are defined on page 15.

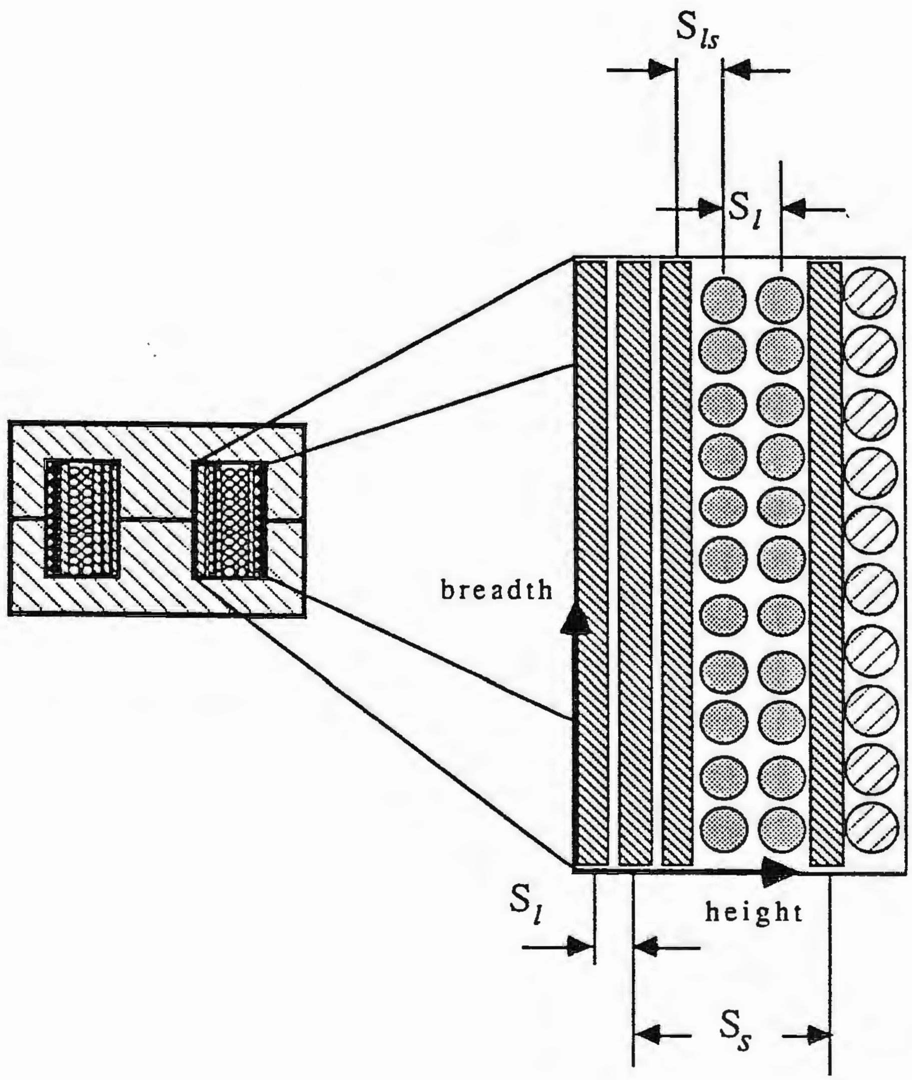

Figure 2.4: Detailed view of section and layer spacing in a three winding EE-core transformer with shell windings. One winding is of foil conductors and consists of the innermost three layers plus the sixth layer. A second winding consists of the fourth and fifth layers of round wire; a third winding consists of the outermost layer of round wire.

Build: The build of a winding is simply the total height—wire height plus wire insulation height—of all the layers of the winding. The sum of the builds of the different windings is limited by the core window height minus any allowance for a bobbin, insulating tape between layers or windings, shields, etc. The build of the foil winding in Fig. 2.4 is four times the total height of the individual foil layers including insulation.

S_ℓ = the center-to-center distance between two adjacent layers of the same winding section.

S_s = the center-to-center distance between two adjacent sections of the same winding.

$S_{\ell s}$ = the center-to-center spacing between adjacent layers of different winding sections.

2.2 GEOMETRICAL WINDING STRUCTURES

The figures in the previous section illustrate the actual winding structures for a variety of shell windings made of differing conductor types including round wire, rectangular and foil conductors. For the purpose of analysis, we would like to treat each of these winding types as though they are made up of foil windings that extend across the entire breadth of the core window. *This approximation allows us to relate the actual winding structure to the model transformer structure we employ in Section 3.1.*

2.2.1 Converting Real Windings to Model Windings

2.2.1.1 Round Wires Modeled as Foils

One key to the process of converting the actual winding types into their model winding equivalents is the method by which round wire windings are transformed into foil windings. The assumptions in this process were introduced in [6] and have been used extensively in other works [11,12,17,19,20]. The steps involved in going from a round-wire winding to an equivalent foil winding are shown in Fig. 2.5.

In the modeling process, the round wires are first replaced by square conductors of equal copper cross-sectional area. These square conductors are then brought together to form an equivalent foil winding with a height[2] equal to that of the square-wire height and a breadth equal to the number of conductors in the layer times the breadth of the equivalent square conductors. This foil winding, which does not extend the entire breadth of the core window, is then in effect "stretched" in the breadth direction and is replaced by a foil of equal height that does extend across the entire window breadth. This stretching increases the total area of the foil layer which must be compensated for in some fashion in the analysis process. This is discussed further below.

[2]Remember that winding *height* is defined in the direction of winding buildup.

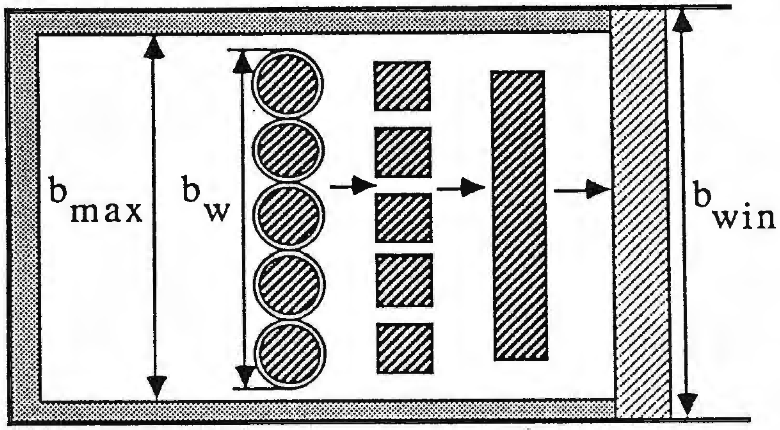

Figure 2.5: Steps in transforming a layer of a round-wire winding into a foil layer [19].

2.2.1.2 Rectangular and Foil Winding Models

A similar modeling process is involved in changing rectangular-conductor windings into foil windings. In this case, the only steps that are required are first to replace the rectangular conductors that make up a layer of the winding by a foil layer of equal height with a cross-sectional area equal to the number of rectangular conductors times the area of each conductor, and then secondly to stretch this foil so that it extends across the entire window breadth. The height of the "stretched" foil of copper conductor is the same as the height of the rectangular conductors.

Finally, all of the copper foil windings in the actual transformer are represented in the model transformer by foils of equal height which extend the entire window breadth. In the case of foil windings, the "stretching" step of the modeling process is all that is needed to go from the real winding to the model winding.

2.2.1.3 Layer Porosity

In the last step of transforming the actual winding structures in a transformer to foil windings (that is, when we "stretch" the equivalent foil winding so that it crosses the *entire window breadth*), we are in effect increasing the cross-sectional area of each of the layers in the winding. In order for this transformation to be valid, there must be some compensating factor introduced which will insure that the dc resistance of the model winding is the same as the dc resistance of the original winding that it replaces.

Since, for any conductor with a given conductivity σ, copper cross-sectional area A_{cu} and length ℓ the resistance R is given as

$$R = \frac{\ell}{\sigma A_{cu}} \tag{2.1}$$

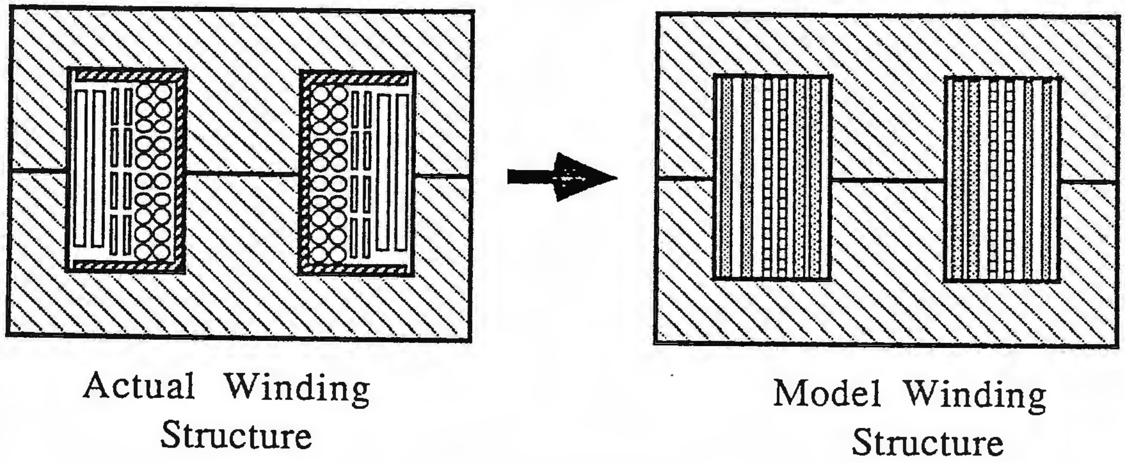

Figure 2.6: Modeling a real winding structure as a set of stretched foil windings that extend across the entire core-window breadth.

we can compensate for the increase in cross-sectional area by dividing this relationship by a factor which will offset the increase. That is, since resistance is inversely proportional to both conductivity and cross-sectional area, we can offset an increase in area by decreasing the conductivity by a corresponding amount. This multiplicative factor is called the *layer porosity* η. The layer porosity is simply the percentage of the total core-window breadth b_{win} that is occupied by conductive material in any winding layer. The value of η is always positive and less than unity. Using this compensating factor we can rewrite (2.1) as

$$R = \frac{\ell}{\eta \sigma A} \tag{2.2}$$

where A is the effective cross sectional area of the stretched foil. A general value of conductivity σ is used in the fields analysis of Chapter 4, but the significant resultant equations are recast in terms of the effective conductivity $\sigma_{eff} = \eta\sigma$ in Section 4.6.

The transformers shown in Fig. 2.6 illustrate how a practical winding structure that contains different kinds of windings is modeled by a transformer with porous-foil windings stretched across the full breadth of the core window. Figure 2.7 shows this type of geometric model in greater detail for a three-winding seven-layer transformer. The parameters shown in the geometric model of the transformer in Fig. 2.7 are defined as follows:

h_{cu} = height of a winding layer modeled as a foil winding. For rectangular and foil windings this is exactly the same as the height of the conductive material in the conductor. In round-wire windings, this is the height of the equal-area square conductors. For a round conductor with a diameter of copper d_{cu} this height is

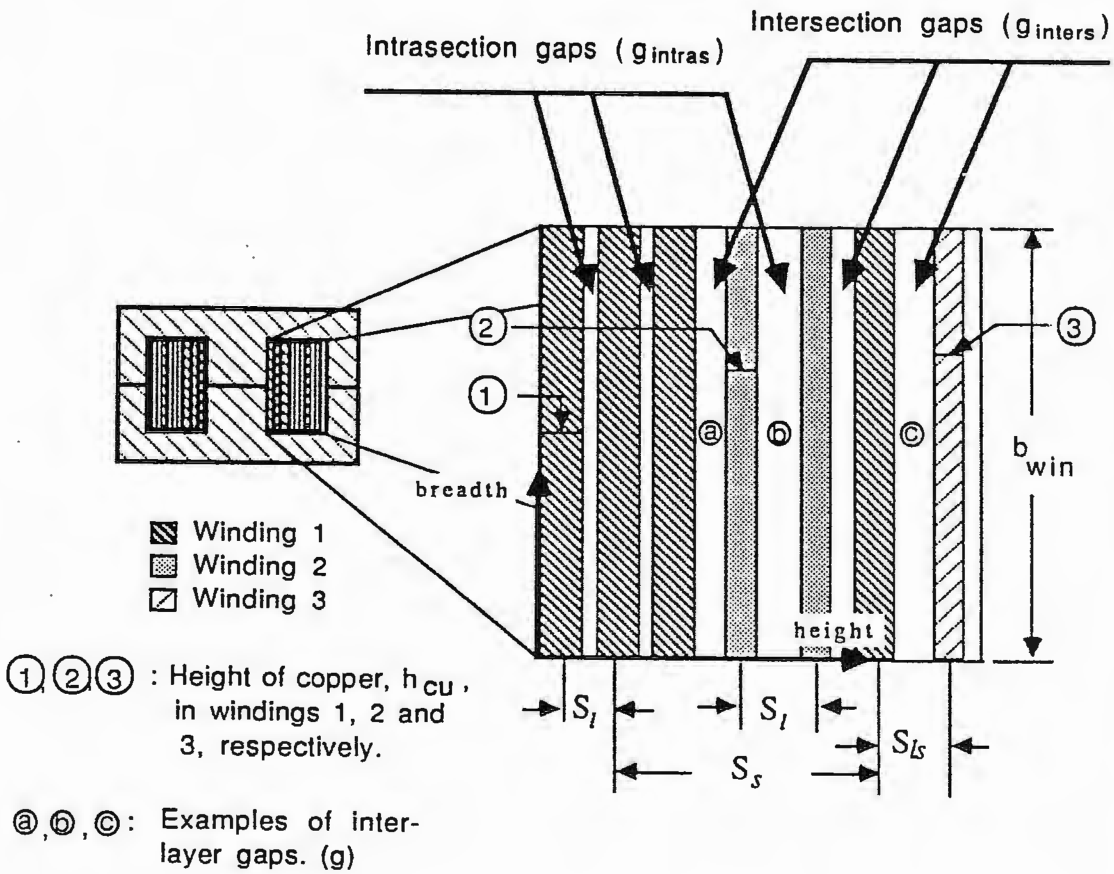

Figure 2.7: Detailed view of the structure of a transformer modeled as a set of foil windings that extend across the entire core-window breadth.

given by

$$h_{cu} = \sqrt{\frac{\pi}{4}}\, d_{cu} \tag{2.3}$$

g_{intras} = intrasection layer gap. This is the distance between adjacent layers of a winding section after the transformer has been modeled as a set of foil windings.

g_{inters} = intersection gap. This is the amount of space there is between any two adjacent winding sections in the model transformer.

g = interlayer gap. This is the distance between any two adjacent layers in the model transformer regardless of whether they are in the same section.

η = layer porosity. As defined in the text above, this is the ratio of the breadth of the conductive material in a winding layer to the breadth of the core window b_{win}. For a winding layer with N_c current-carrying conductors each of a height h_{cu} and a breadth b_{cu}, the porosity η is given by

$$\eta = \frac{N_c b_{cu}}{b_{win}} \tag{2.4}$$

The intersection gap g_{inters} and intrasection gap g_{intras} are both examples of interlayer gaps, i.e., gaps between two layers. The term interlayer gap describes the gap between two layers whether they are members of the same or different winding section(s).

Note that when transforming an actual winding into a foil equivalent, it is the layer and section center-to-center spacings in the direction of winding buildup which are held constant. For a round-wire winding, the height h_{cu} is different from the conductor diameter d_{cu} and the outer diameter d_o of the wire. For all types of windings, there is a "stretching" process which changes the breadth of the winding layer. However, in all cases the center-to-center spacing between layers S_ℓ in a winding section, the center-to-center distance S_s between winding sections and the center-to-center spacing $S_{\ell s}$ between layers of different sections are all retained.

2.2.2 Admonitions Concerning the Use of Layer Porosity η

Although the concept of layer porosity[3] is generally accepted in the reviewed literature [6,11,12,20], the reader should be warned that the indiscriminate use of layer porosity can lead to erroneous results. The analyses performed here and in [6] are "reliable" only for values of η which are not "too small" [17, pages 322,323]. A cornerstone of the analysis presented in Chapters 3, 4 and 5 is that the flux in the core window is parallel to the winding layers across the entire breadth of the core window as shown in Fig. 2.2. When discrete conductors constitute the winding layers, the validity of the assumption of parallel flux depends largely on the value of η. When conductors in a layer

[3]Layer porosity is also referred to as layer space factor and horizontal porosity in the literature reviewed in Part II.

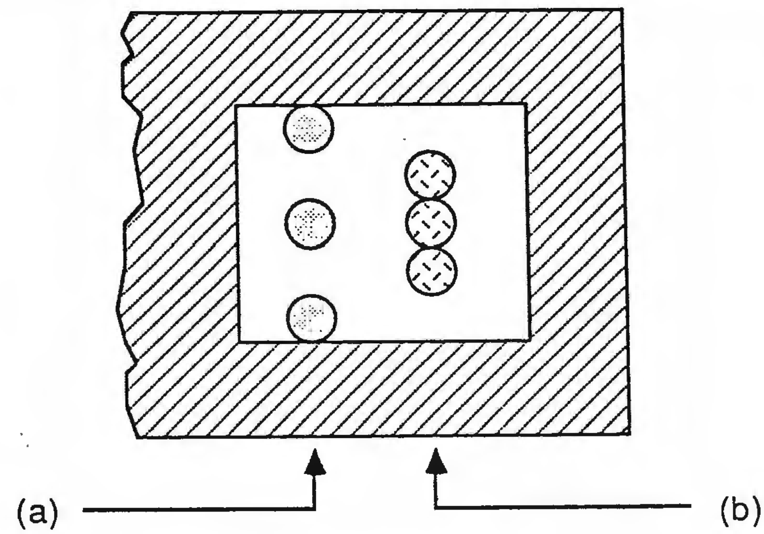

Figure 2.8: Example of conductor layers where η may be too small. In (a) the conductors are spaced throughout the breadth of the window but have significant distances between them. In (b) the conductors are contiguous but there is significant distance between the transformer-core yolk and the layer of conductors.

are spread throughout the window breadth and have significant distances between the conductors, as in Fig. 2.8(a), or if all the conductors in the layer are bunched together with significant distance between the ends of the layer and either the upper or lower yoke of the transformer core, as in Fig. 2.8(b), considerable bending of the flux lines occurs. Hence, small values of η negate one of the fundamental assumptions of Chapter 3 and call into question the validity of the analysis presented in Chapters 3, 4 and 5. When round-wire conductors are modeled as foil conductors, the maximum possible value of layer porosity is $\eta = 0.89$, which occurs only when the wires are contiguous, entirely fill the core-window breadth b_{win} and have negligible insulation.

2.3 DIFFERENT COMPONENTS OF LEAKAGE FLUX

Throughout Parts I and II of this report, we discuss the effects of leakage flux on transformer windings and how to predict these effects. The use of the term *leakage flux* may lead to some confusion since leakage flux in transformers can be considered to be made up of two components, only one of which is covered in this report and in the literature reviewed in Part II. In a transformer, leakage flux arises because of the following:

1. The effective permeability of the transformer core is low, i.e., not much greater than that of free space ($\mu \not\gg \mu_0$). This occurs when a core has substantial intentional or

unintentional air gaps, or when the core material has a low intrinsic permeability as do some ferrites.

2. The winding height h_{cu} of the transformer windings and the heights of the interlayer gaps between windings and within each winding are of nonzero value.

Since core materials with infinite permeability and winding layers of zero height do not exist in nature, both of these components of leakage flux occur, to some degree, in any physical transformer; however, often one or the other component can be considered negligible depending upon the transformer design and application.

Figure 2.9(a) shows the right half of a transformer where the permeability μ of the core is low and the winding and interlayer-gap heights are nonzero, so both components of leakage flux are present in the winding space. To examine the two separate causes of leakage flux, we modify Fig. 2.9(a) appropriately to produce Fig. 2.9(b) and (d). In Fig. 2.9(b), we examine the condition in item 1 and retain the same permeability for the core material as in (a), but shrink the winding heights so that $h_{cu} = 0$ for both primary and secondary. In Fig. 2.9(d), we examine the condition in item 2 and retain the same winding heights as in (a) but assume an ideal core material with $\mu = \infty$ and zero coercive force.

If we examine Fig. 2.9(b) more carefully, we note the points A and E located in the top and bottom core yolks, respectively, points B and D located in the inner and outer legs of the core, respectively, and point C in the center of the interlayer gap. Magnetic flux ϕ which flows through the center leg of the transformer—path (EBA)—can flow both through path (ADE) in the outer leg of the core and through path (ACE), the air in the transformer window. The amount of flux which flows in each path is dependent upon the relative reluctance values of paths (ADE) and (ACE).

Viewing the transformer as a lumped magnetic circuit as is shown in Fig. 2.9(c), we note that the reluctance $\mathcal{R}$ of a magnetic flux path is

$$\mathcal{R} = \frac{\ell}{\mu A} \tag{2.5}$$

where ℓ is the magnetic path length and A is the cross-sectional area of the magnetic path. In addition, we can describe the magnetic circuit in terms of its magnetomotive force $\mathcal{F}$, the flux in the center leg of the core $\phi_{(EBA)}$, and $\mathcal{R}_{(EBA)}$, $\mathcal{R}_{(ACE)}$ and $\mathcal{R}_{(ADE)}$ the reluctances of the various flux paths marked in Fig. 2.9(b). Viewing flux as the analog of current, mmf as the analog of voltage, reluctance as the analog of resistance and assuming that the inner winding is excited and the outer winding is open-circuited, the flux $\phi_{(EBA)}$ encounters the reluctance $\mathcal{R}_{(EBA)}$ in series with the parallel paths $\mathcal{R}_{(ACE)}$ and $\mathcal{R}_{(ADE)}$. Thus, we can write the magnetic analog of Ohm's law for the transformer.

$$\mathcal{F} = N_1 i_1 = \phi_{(EBA)} \left(\mathcal{R}_{(EBA)} + \frac{\mathcal{R}_{(ACE)} \mathcal{R}_{(ADE)}}{\mathcal{R}_{(ACE)} + \mathcal{R}_{(ADE)}} \right) \tag{2.6}$$

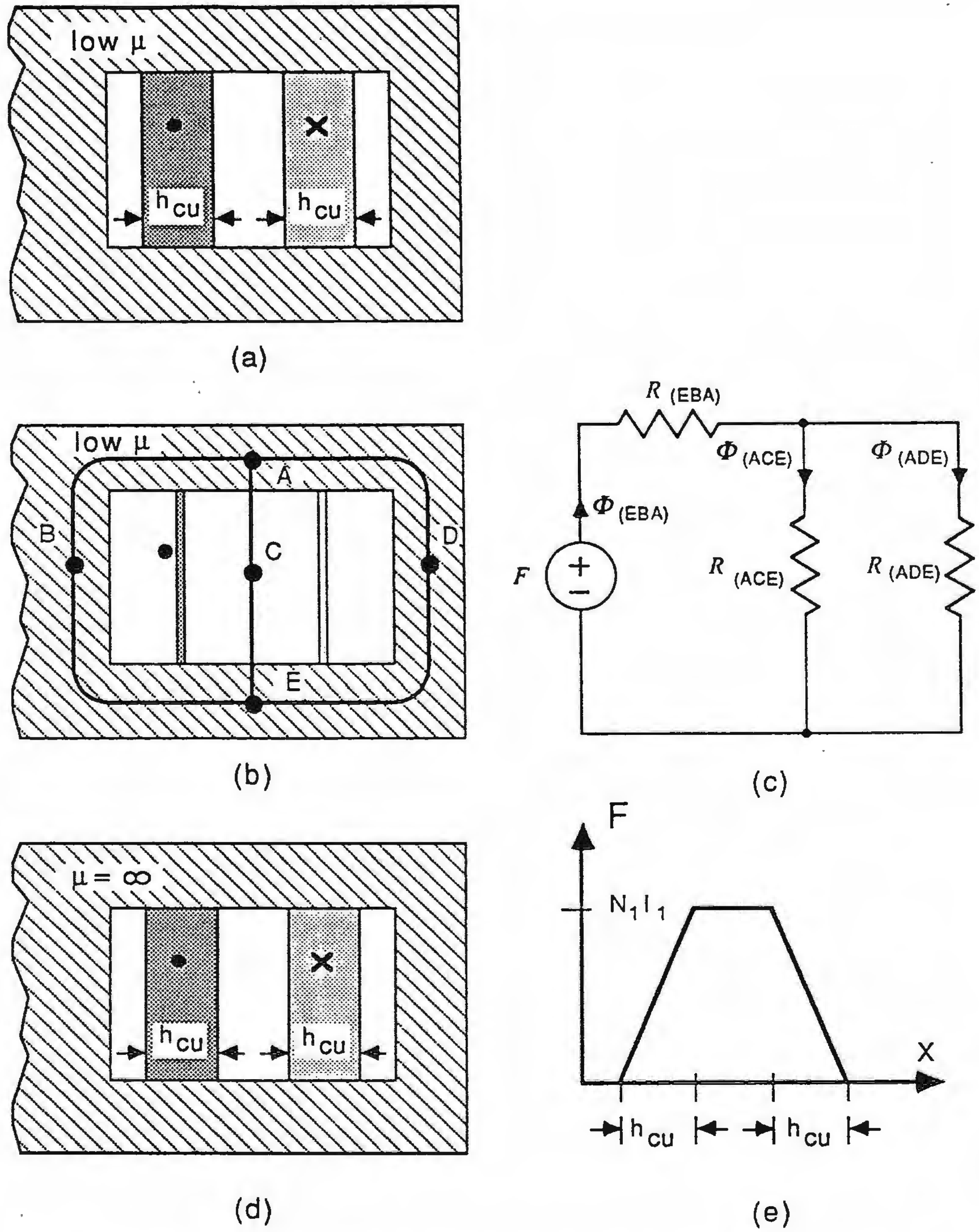

Figure 2.9: Leakage flux in a transformer is due to $\mu \neq \infty$ *and* $h_{cu} \neq 0$. Part (a) shows such a transformer. In (b), $h_{cu} = 0$ but $\mu \not\gg \mu_0$ and the reluctance of flux path (ACE) is on the same order of magnitude as that of path (ADE). (c) shows the magnetic equivalent circuit for the core of (b) when the inner winding is excited. In (d), $h_{cu} \neq 0$ and $\mu = \infty$; leakage flux is due to the variation of mmf shown in (e).

Likewise, we can view the reluctances of paths (ACE) and (ADE) as a flux-divider network which allows us to write the fluxes associated with those paths in terms of $\phi_{(EBA)}$

$$\phi_{(ACE)} = \phi_{(EBA)} \frac{\mathcal{R}_{(ADE)}}{\mathcal{R}_{(ACE)} + \mathcal{R}_{(ADE)}} \tag{2.7}$$

$$\phi_{(ADE)} = \phi_{(EBA)} \frac{\mathcal{R}_{(ACE)}}{\mathcal{R}_{(ACE)} + \mathcal{R}_{(ADE)}} \tag{2.8}$$

Examining (2.5), (2.7), and (2.8) we see that if the effective permeability of the magnetic core is sufficiently low, $\mathcal{R}_{(ACE)}$ and $\mathcal{R}_{(ADE)}$ may be on the same order in which case $\phi_{(EBA)}$ will split more or less evenly between them.

Although the outer winding in Fig. 2.9(c) conducts no current, the voltage which appears across its terminals is determined by Faraday's law, $v_2 = N_2 \, \partial\phi_2/\partial t$ where ϕ_2 is the flux linked by the N_2 turns of the outer winding. From Fig. 2.9, we see that the flux which links the outer winding is not equal to that which links the inner winding, $\phi_{(EBA)}$, by the amount of flux "leaking" through the window, $\phi_{(ACE)}$. In other words, $\phi_2 = \phi_{(EBA)} - \phi_{(ACE)}$. If the effective permeability of the transformer core increases, $\mathcal{R}_{(ADE)}$ and $\phi_{(ACE)}$ decrease, and $\phi_2 = \phi_{(ADE)}$ increases toward $\phi_{(EBA)}$, the flux linked by the inner winding.

The flux following path (ACE) in Fig. 2.9(b) is leakage flux which is caused by an imperfect core material. This is the type of leakage flux commonly discussed with reference to gapped transformers and other low-permeability energy-storage cores. This type of leakage flux is *not* the subject of the present report and is not discussed further in this document or in any of the papers review in Part II of this report.

As is stated above, when the permeability of the transformer core increases, more of the flux $\phi_{(EBA)}$ in Fig. 2.9(b) continues along the path (ADE), since the reluctance of path (ADE) decreases. However, it would be incorrect to take the limit of (2.7) and (2.8) as permeability approaches infinity and use these limits and Fig. 2.9(c) to assume that a perfect core material means that there is perfect coupling between the windings of a general two-winding transformer. In Fig. 2.9(b) and (c) only one winding current is permitted to flow so that we can decouple the two components of leakage flux. In a general two-winding transformer where both windings are conducting, there is a component of leakage flux which occurs even if the core material is perfect.

To illustrate this second source of leakage flux, we present Fig. 2.9(d). Here $\mu = \infty$, $N_1 I_1 = N_2 I_2$, and the transformer windings are represented as having nonzero height h_{cu}. Figure 2.9(e) shows, as a function of distance x along the core's window, the mmf of the transformer for the condition shown in Fig. 2.9(d). We see that as distance increases, the number of ampere-turns increases as the inner winding is traversed. In the interlayer gap, the magnetomotive force $\mathcal{F}$ remains constant and then decreases as the outer winding is traversed. Field-intensity or mmf diagrams such as that shown in Fig. 2.9(e) are discussed in detail in Section 3.1.2, but for now it is sufficient to note that since flux is proportional to mmf, the leakage flux in the winding space varies with distance in the same fashion as does $\mathcal{F}$ in Fig. 2.9(e), and is due to the current in the windings and the nonzero heights of the windings and interlayer gaps. If the winding heights in Fig. 2.9(d) were reduced to zero and the windings placed infinitesimally close together, then no flux would appear in the core window since both components are equal to zero. However, just the opposite is true for the transformer pictured in Fig. 2.9(a), where both components of leakage flux exist. Throughout the analysis presented in Part I we assume that the core material has such a high permeability that the leakage flux due to the nonzero heights of the winding layers and interlayer gaps is dominant. Therefore, we are interested only in leakage flux in the core window which is caused by the variation of $\mathcal{F}$ with distance. This type of leakage flux is also the focus of the papers reviewed in Part II.

This page has been left blank intentionally.

4-Day Design Workshops Learn how to design, build, test and measure faster and with more precision from the leader in power electronics design education since 1991.

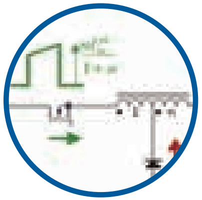

Choose a Topology
Learn about popular topologies used worldwide for modern applications.

Apply Basic Magnetics
Understand the single equation needed to begin design execution.

Apply Advanced Magnetics
Optimize magnetics losses and incorporate advanced analyses.

Model and Measure
Learn how to model non-linear circuits and measure the results.

Voltage- and Current-mode Control
Measure the response and apply control and loop design techniques.

Design Transformers
Design, build and test transformers and inductors in a hands-on lab.

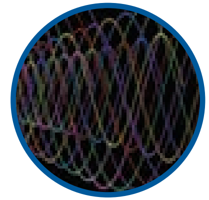

Design Snubber
Optimize a snubber in one pass using software and hardware applications.

Measure Efficiency
Compete with fellow classmates to accurately measure efficiency.

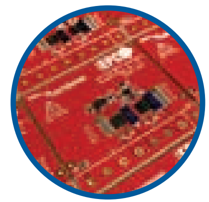

Design GaN
Learn first-hand how to design with the latest GaN technologies for converters.

Design Synchronous Rectifiers
Become familiar with synchronous rectifiers and design applications.

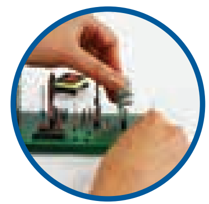

Optimize Control
Intuitively and visually shape and adjust loops for optimal performance.

Prototype with SwitchBit®
Develop a working prototype for multiple applications in just a few hours.

Chapter 3

Magnetic-Field Distribution in the Winding Space of a Transformer

The leakage impedance between each pair of windings is important information for modeling high-frequency effects in a transformer. The resistive part of the leakage impedance arises from the resistivity of the conducting material and the uneven distribution of current in the conductors at high frequency. The inductive part exists because part of the magnetic flux generated by a current in any one winding fails to link with all the turns of both windings. In the following discussion, the infinite-solenoid model is introduced as a way of representing the essential structure of a multiwinding transformer. Because the magnetic-field distribution in such a solenoid is similar to that in a shell-winding transformer wound on a relatively high-permeability core, an understanding of the leakage-flux pattern in an actual transformer may be gained by examining the leakage flux in a multilayer infinite solenoid.

It is shown in Chapter 5 how the two components of leakage impedance, ac winding resistance and leakage inductance, are calculated from the power dissipated and the magnetic energy stored in the windings of a transformer. In Section 4.5, equations are derived by which values for power dissipation and energy storage can be calculated from the spatial distribution of magnetic field intensity in the volume occupied by the transformer windings. That magnetic-field-intensity distribution is derived for the air-and-insulation spaces between winding layers in this chapter, and for the interior of each winding layer in Chapter 4. Also in this chapter, the basic principles that govern the behavior of the magnetic field in the transformer winding space are explained.

In Section 3.1 below, it is shown how a hypothetical infinite solenoid carrying dc current is used to predict the frequency-*independent* magnetic-field distribution between the winding layers of a real transformer. That distribution depends only on the net current flowing in each winding, not how the current is distributed within each winding layer. Section 3.2 contains a qualitative discussion of eddy-current effects, which cause a frequency-*dependent* redistribution of magnetic field intensity and current density inside each winding layer. Finally, Section 3.3 shows how an infinite current sheet is used to model each winding layer to solve for the magnetic-field-intensity distribution inside each layer as a function of frequency. The magnetic-field-intensity distribution and the associated current-density distribution in an infinite current sheet are derived in the next chapter. Here and throughout Part I of the report, all time-varying currents and fields are assumed to be sinusoidal.

3.1 INFINITE-SOLENOID MODEL OF A TRANSFORMER

To simplify the problem of calculating the fields present in the winding space of a real transformer, it is shown in Section 2.2.1 how actual winding layers are modeled as foil layers that extend the entire breadth of the core window. Here, it is asserted that the leakage-flux pattern in and between those model winding layers, *when surrounded by a pot core of infinite permeability*, is exactly the same as the flux pattern present in a slice of a hypothetical infinite solenoid. An *infinite solenoid* is defined as a *tightly* wound torus with a finite circular cross section and a ring radius that approaches infinity, illustrated in Fig. 3.1. A *loosely* wound torus is shown instead in the figure to avoid obscuring the flux lines, which never leave the inside of the torus.

The magnetic flux in the infinitely long solenoid of Fig. 3.1(c) is said to follow a return path "at infinity." If a finite section of such a single-layer infinite solenoid is enclosed in infinitely permeable magnetic material as shown in Fig. 3.2, the leakage flux in the winding space is unchanged. The reason is that the axially directed flux of the infinite solenoid already satisfies the boundary condition required by Maxwell's equations, that is, the flux must be perpendicular to the surface of the ideal magnetic material where it enters the material. Essentially, the ideal magnetic material provides a return path for the flux that is equivalent to the path "at infinity" in Fig. 3.1(c).

With a magnetic yoke of less than infinite permeability, the leakage-flux pattern is close to that in an infinite solenoid as long as the component of the primary current that excites the core is small with respect to the component that supplies the loads. This condition is used as the definition of "high" permeability.

The structure of the model pot-core transformer in Fig. 3.3(b) is basically the same as that of Fig. 3.2. The only differences are multiple conducting layers, addressed in Section 3.1.2.2 below, and a center leg of the core. Although adding the center leg substantially increases the permeance of the core by eliminating a large air gap, it does not affect the distribution of the leakage flux in the winding space outside of the center leg.[1] If the transformer being modeled has an EE core of high permeability instead of a pot core, the infinite-solenoid model is less accurate, but it is shown in Chapter 6 that

[1] This leakage flux is due to the second cause discussed in Section 2.3, namely, layer current distributed over the finite height of the conductor.

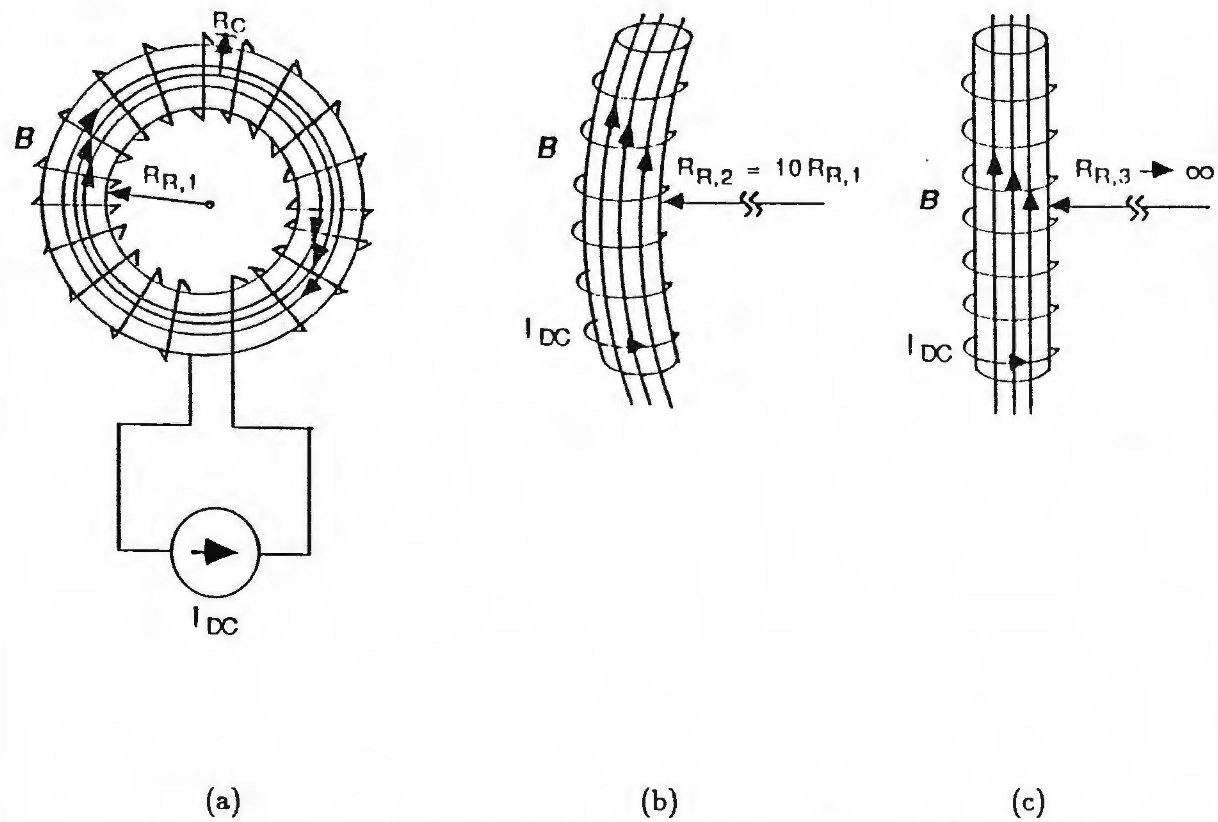

Figure 3.1: Steps of the limiting process which defines the term *infinite solenoid*. (a) A toroidal solenoid of ring radius $R_{R,1}$, which may or may not have a core present. A current I_{DC} flowing in the solenoid produces a magnetic field intensity B inside the torus. (b) If the ring radius is increased by a factor of ten, but the current in the winding and the number of turns per meter along the solenoid remain constant, the same magnetic field intensity B is produced inside the solenoid. (c) As the ring radius approaches infinity, the device approaches an infinite solenoid.

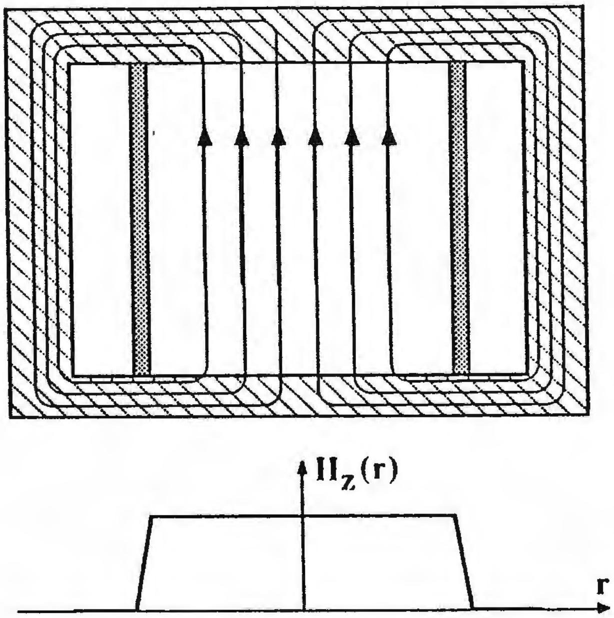

Figure 3.2: (a) Section of a one-layer infinite solenoid surrounded by a magnetic "yoke" with infinite permeability. The magnetic material provides a return path for the flux that is equivalent to a return path "at infinity."

the model still gives good results.

As seen in this discussion, the multilayer infinite solenoid in Fig. 3.3(a) may be analyzed to determine the magnetic-field distribution in the winding space of the transformer model in Fig. 3.3(b), which has equivalent-foil windings surrounded by a high-permeability magnetic core. The value of the magnetic field outside an infinite solenoid, the starting point of any analysis, is established in Section 3.1.1. Then dc field distributions are analyzed in Section 3.1.2, followed by a brief discussion of ac field distributions in Section 3.1.3.

3.1.1 The Magnetic Field Outside an Infinite Solenoid

In the infinite solenoid of Fig. 3.1(c), all of the magnetic flux generated by current flowing in the solenoid remains inside the torus, which implies that the magnetic field is zero everywhere outside the infinite solenoid regardless of the current flowing. For this statement to be true, is must be assumed that no externally generated magnetic fields are present. Another necessary assumption is that the component of the current along the axis of the solenoid is negligible, which requires that the solenoid be tightly wound. Both of these assumptions are made throughout this report.

The fact that the magnetic field is zero everywhere outside an infinite solenoid can also be proven rigorously from the Biot-Savart law, which gives the magnetic field produced at any point in space by a differential current element at another point in space. By

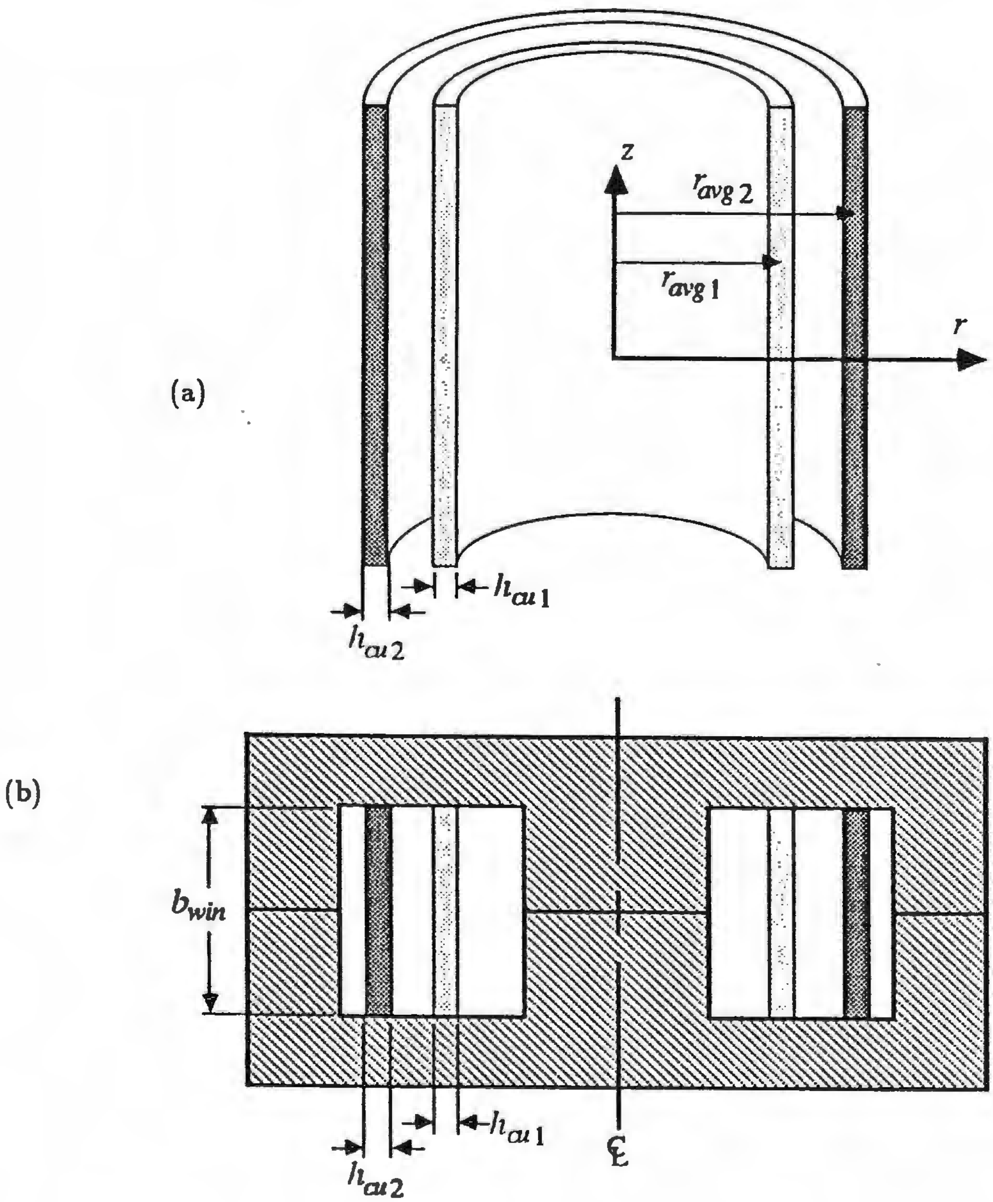

Figure 3.3: (a) Section of a two-layer infinite solenoid. (b) Pot-core transformer model containing the infinite-solenoid section in Part (a). The transformer model has winding layers of height h_{cu1} and h_{cu2} and breadth b_{win} as indicated.

integrating over a finite-length cylinder of current, and letting the length of the cylinder approach infinity, the net magnetic field at any point outside the cylinder can be shown to be zero.

3.1.2 Field Distribution with DC Current

It is stated in the introduction of this chapter that the magnetic field intensity everywhere in a transformer, except inside the conducting material, is independent of frequency and depends only on the net current flowing in each layer. This statement is proven below using Ampere's law. This fact, together with the earlier deduction that the fields in an infinite solenoid approximate those in an actual transformer, implies that an infinite solenoid with *dc* currents flowing in its layers may be used to calculate the instantaneous *ac* magnetic field present in the interlayer spaces of a transformer. Such a dc analysis does not, however, give accurate results for the ac field inside the conducting material. The analysis is carried out below for a single-layer air-core infinite solenoid, then extended to a two-layer solenoid, and finally to an infinite solenoid that has a magnetic core.

3.1.2.1 Ampere's Law Applied to a Single-Layer Infinite Solenoid

Having established that the magnetic field is always zero outside an infinite solenoid, Ampere's law for static fields

$$\oint_{l(S)} \mathbf{H} \bullet \mathbf{dl} = \iint_{S(l)} \mathbf{J} \bullet \mathbf{dS} \tag{3.1}$$

may be used to calculate the magnetic field distribution inside an infinite solenoid carrying dc current as shown in Fig. 3.4. The integration path $l(S)$ is the closed curve or loop l which bounds a surface S, while the surface of integration $S(l)$ is a surface S bounded by the closed curve l. The directions of the differential vectors **dl** and **dS** are chosen to be consistent with each other according to the right-hand rule. The direction of the differential-length element **dl** is chosen to be "clockwise," and the direction of the differential-surface-element vector **dS** is chosen to be "into the paper" as shown for loop l_1. The dots and the crosses in the current-conducting foil indicate that current is flowing into the right-hand side of the solenoid and out of the left-hand side.

By using the pictured series of closed curves as the integration paths for Ampere's law, it is shown below that the magnetic field is uniform inside the solenoid and directed vertically in what is defined as the positive z-direction. In addition, it is shown that the field changes linearly with the radius r across the height of the conducting layer.

First the following conditions are established to simplify the problem:

1. Only dc current flows in the solenoid, for which the current density in the conducting layer is uniform. Uniform current density is also a very good approximation whenever the excitation current is varying slowly.

2. There are no externally generated magnetic fields present.

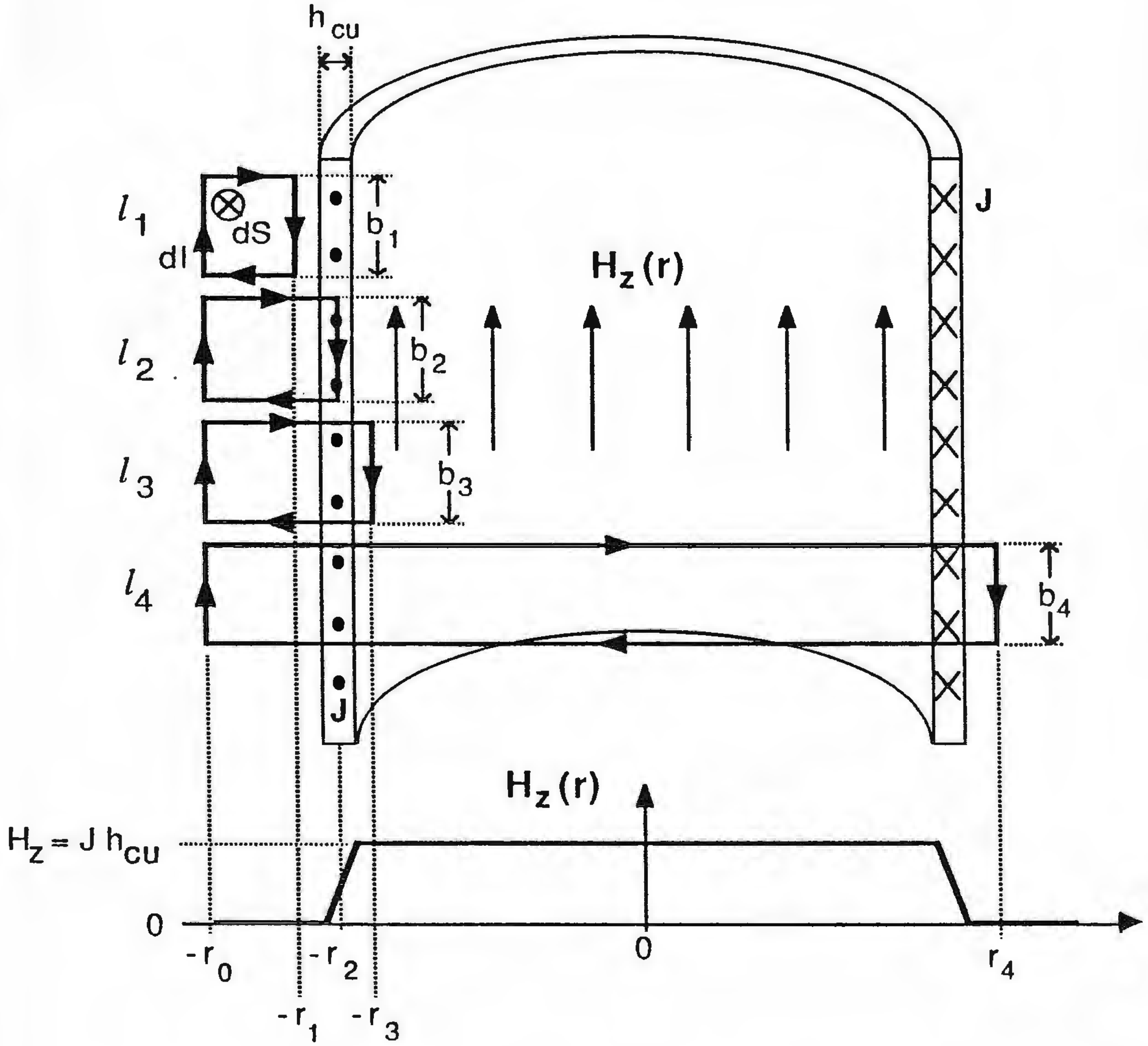

Figure 3.4: Integration paths used with Ampere's law to calculate the magnetic field intensity $H_z(r)$ in an infinitely long solenoid conducting at a uniform current density J.

3. The infinite length of the solenoid and its uniformity in the z-direction dictate that the magnetic field generated by the solenoid is everywhere parallel to the axis of the solenoid. The reference or positive direction for **H** is chosen to be "up," in the direction of the $H_z(r)$ vectors shown.

4. The integration paths are chosen to be rectangles so the magnetic field intensity **H** is either perpendicular or parallel to **dl** at every point along the path.

5. The surface of integration is chosen to lie in the plane of the figure, which causes **dS** to be parallel to the current-density vector **J**.

For any of the four loops l_1 to l_4 in Fig. 3.4, the left side of Ampere's law (3.1) may be rewritten as the sum of the line integrals along each of the four segments of the rectangular integration path l.

$$\oint_l \mathbf{H} \bullet \mathbf{dl} = \int_{\text{left}} \mathbf{H} \bullet \mathbf{dl} + \int_{\text{top}} \mathbf{H} \bullet \mathbf{dl} + \int_{\text{right}} \mathbf{H} \bullet \mathbf{dl} + \int_{\text{bottom}} \mathbf{H} \bullet \mathbf{dl} \tag{3.2}$$

By condition 3 above, **H** is always perpendicular to **dl** along the top and bottom segments of the chosen integration paths, causing the second and fourth terms on the right-hand side to be zero.

Loop l_1 of Fig. 3.4 may be used to show that the magnetic field outside the solenoid is uniform. After performing the remaining dot products in (3.2) for this loop,

$$\oint_{l_1} \mathbf{H} \bullet \mathbf{dl} = b_1 H_z(-r_0) + 0 - b_1 H_z(-r_1) + 0 \tag{3.3}$$

where $H_z(-r_0)$ and $H_z(-r_1)$ represent the magnetic field intensity at the locations $r = -r_0$ and $r = -r_1$, respectively. The loop breadth b_1 in the third term is negative because **dl** is directed in the negative-z direction along the right segment of the integration path.

The right side of Ampere's law (3.1) is zero for loop l_1 because the current density J is zero everywhere inside this loop. Setting (3.3) equal to zero yields

$$H_z(-r_0) = H_z(-r_1) \tag{3.4}$$

which confirms that the field outside the solenoid is uniform, shown in the previous section to be zero.

For loop l_2 in Fig. 3.4, where $r = r_2$ is the midpoint of the conducting layer of height h_{cu}, the left side of Ampere's law may be written from (3.2) as

$$\oint_{l_2} \mathbf{H} \bullet \mathbf{dl} = 0 + 0 - b_2 H_z(-r_2) + 0 \tag{3.5}$$

which makes use of the fact that $H_z(-r_0) = 0$. With r_2 exactly at the center of the conducting layer, the corresponding right side of Ampere's law (3.1) is

$$\iint_{S(l_2)} \mathbf{J} \bullet \mathbf{dS} = -J \frac{h_{cu}}{2} b_2 \tag{3.6}$$

where J is the dc value of the current-density vector $\mathbf{J}$. The negative sign occurs because $\mathbf{J}$ is directed opposite $\mathbf{dS}$. Equating (3.5) and (3.6)

$$H_z(-r_2) = J\frac{h_{cu}}{2} \tag{3.7}$$

Similar equations may be written for loop l_3.

$$\begin{aligned}
\oint_{l_3} \mathbf{H} \bullet \mathbf{dl} &= 0 + 0 - b_3 H_z(-r_3) + 0 && (3.8)\\
\iint_{S(l_3)} \mathbf{J} \bullet \mathbf{dS} &= -J h_{cu} b_3 && (3.9)\\
H_z(-r_3) &= J h_{cu} && (3.10)
\end{aligned}$$

Moving the right side of loop l_3 to any position inside of the conducting cylinder would not change the calculated value of H. Stated differently, the magnetic field intensity is uniform and given by (3.10) everywhere inside the solenoid. In addition, (3.7) and (3.10) show that the magnetic field intensity varies linearly across the height of the conducting layer.

Finally, the corresponding equations for loop l_4 of Fig. 3.4 confirm once again that the magnetic field is uniformly zero everywhere outside the infinite solenoid.

$$\begin{aligned}
\oint_{l_4} \mathbf{H} \bullet \mathbf{dl} &= 0 + 0 - b_4 H_z(r_4) + 0 && (3.11)\\
\iint_{S(l_4)} \mathbf{J} \bullet \mathbf{dS} &= -J h_{cu} b_4 + J h_{cu} b_4 = 0 && (3.12)\\
H_z(r_4) &= 0 && (3.13)
\end{aligned}$$

The two terms on the right side of (3.12) correspond to the left and right intersections of surface $S(l_4)$ with the conducting cylinder. By continuously varying the position of the right side of the rectangular integration path from $r = -r_1$ to $r = r_4$, one obtains the profile of magnetic field intensity shown at the bottom of Fig. 3.4.

3.1.2.2 Magnetic Field in a Two-Layer Infinite Solenoid

Figure 3.5 shows a solenoid which has two concentric and infinitely long layers with layer heights h_{cu1} and h_{cu2} and average radii r_{avg_1} and r_{avg_2} respectively. These radii are different from the "ring" radii in Fig. 3.1, which approach infinity for any infinite solenoid. The inner layer of the solenoid in Fig. 3.5 is called layer 1 and is wound with n_1 turns of rectangular conductor per meter of the solenoid in the z-direction. The outer layer is wound with n_2 turns of square conductor per meter of the solenoid in the z-direction. For convenience of discussion for the remainder of this illustration, n_2 is chosen to be twice n_1. The layers are shaded differently to emphasize that they are not necessarily two layers of a single winding. Rather, each layer is considered to be a separate element that can carry current in either direction independent of the current in

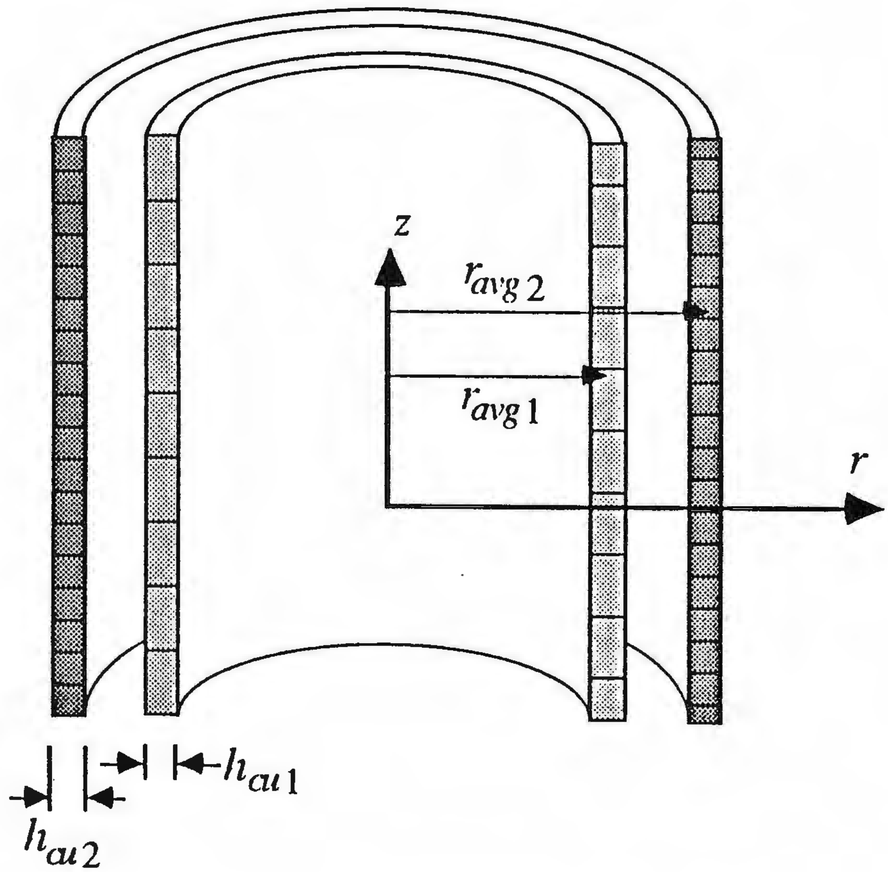

Figure 3.5: Infinitely long solenoid with two layers. The inner layer has n_1 turns per meter, average radius r_{avg_1}, and height h_{cu1}. The outer layer has n_2 turns per meter, average radius r_{avg_2}, and height h_{cu2}.

the other layer of the solenoid. The layers could carry the same current, but this is not required.

Assuming no external magnetic field is present, Fig. 3.6(a) shows the field distribution that exists around the solenoid when the outer winding layer is carrying a current $I_{2,DC}$ and the inner layer is carrying no current. Because the relative permeability of copper is close to one, and because there are no time-varying fields which would induce eddy currents in the inner conducting layer, the magnetic field distribution is exactly the same as in Fig. 3.4 where no inner layer is present. From (3.10), the magnetic field intensity everywhere inside the inner surface of layer 2 is given by

$$H_z = Jh_{cu} = \left(\frac{n_2 I_{2,DC}}{h_{cu2}}\right) h_{cu2} = n_2 I_{2,DC} \tag{3.14}$$

where n_2 has units of turns per meter.

Instead, if the inner layer is excited with a current $I_{1,DC}$ and the outer layer is left open-circuited, the plot of magnetic-field-intensity distribution appears as in Fig. 3.6(b). As in the case above for current flowing only in the outer layer, there is no z-directed magnetic field created outside an infinitely long cylindrical layer *by a current flowing in that layer.* The magnetic field in the region surrounded by layer 1 is $n_1 I_{1,DC}$, produced by the current in layer 1. In this illustration, the magnetic field intensity $n_1 I_{1,DC}$ is shown as half the value $n_2 I_{2,DC}$ in Part (a). Thus for this example, since $n_1 = n_2/2$,the magnitudes of the two currents $I_{1,DC}$ and $I_{2,DC}$ are equal.

The individual magnetic fields described above can be superposed to give the net magnetic field that exists in a solenoid of two layers. The currents $I_{1,DC}$ and $I_{2,DC}$ need not be equal and their directions need not be the same. In fact, there are no restrictions placed on these currents at all.

However, if $I_{1,DC} = I_{2,DC}$, which implies that the currents are equal and flow in the same direction, the magnetic field contributions of the two layers in the solenoid add, producing the field distribution shown in Fig. 3.6(c). The field strength between the two layers is the same as when only the outer layer carries current, but the field inside the inner layer is the sum of the fields produced by the individual layer currents. If the direction of the current in layer 1 is reversed, the net magnetic field distribution in the solenoid is the difference between the two contributions. This is illustrated in Fig. 3.6(d). Again, the field intensity between the two layers is that due to current in the outer layer only, while the field intensity inside the inner layer is the result of superposing the fields generated by the currents in both layers. These same plots of magnetic field intensity versus radius may be obtained by applying Ampere's law to a series of rectangular integration paths similar to those in Fig. 3.4.

The magnetic field intensity H that exists in the space surrounded by any winding layer establishes lines of magnetic flux ϕ which link the turns of that infinitely long layer *by closing on themselves via a flux path at infinity* [19, p. 356]. That flux path lies inside the torus of infinite ring radius shown in Fig. 3.1(c). Any flux in the innermost region of the solenoid links all the layers of the solenoid, but the flux in the conducting layers themselves and in the spaces between the conducting layers links only the layers further

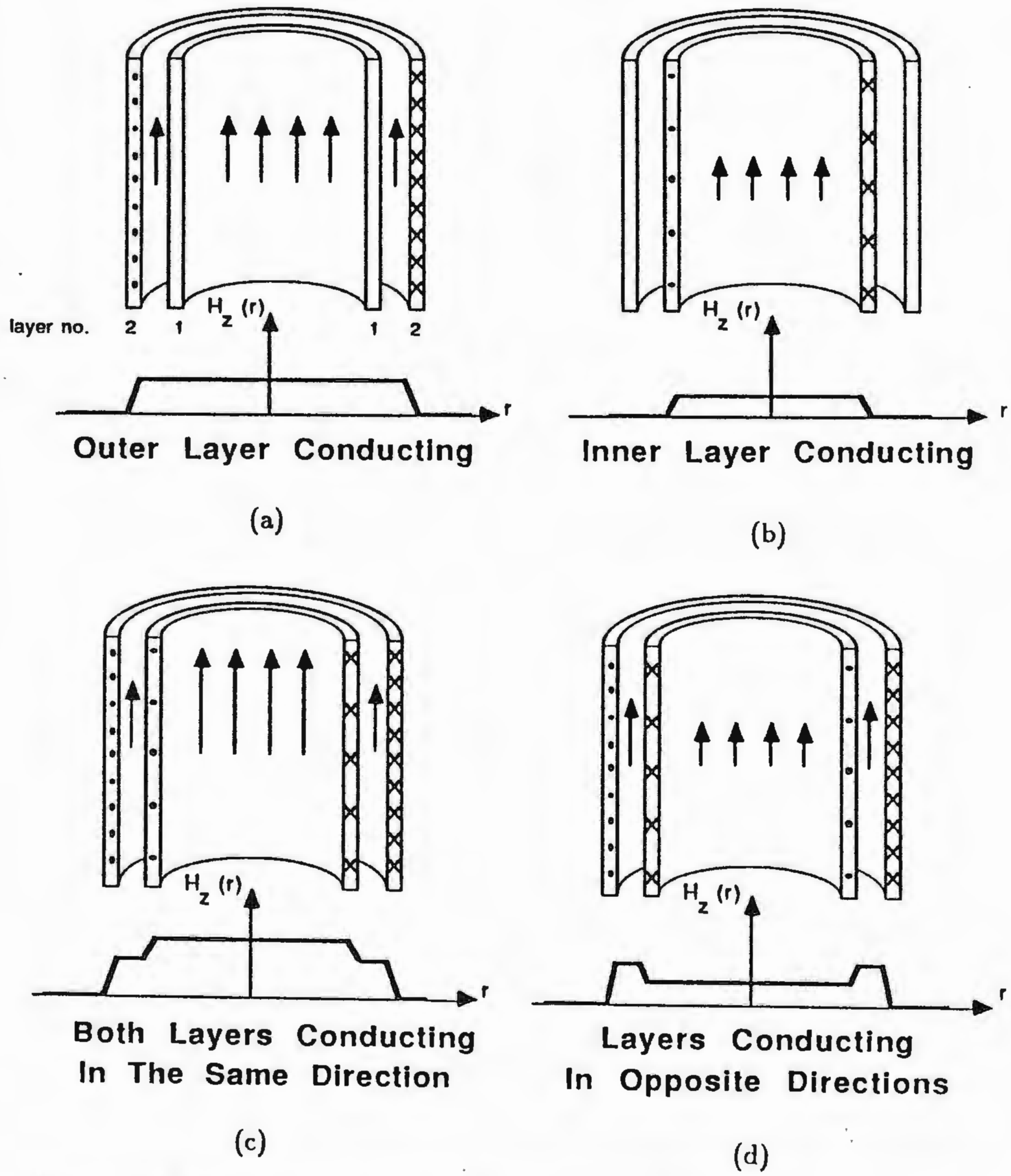

Figure 3.6: Field distribution inside an infinitely long two-layer solenoid with (a) only the outer layer conducting, (b) only the inner layer conducting but at half the current density, (c) both layers conducting the stated currents in the same direction, and (d) both layers conducting the stated currents but in opposite directions. The lengths of the arrows are proportional to the strength of the magnetic field in the different regions.

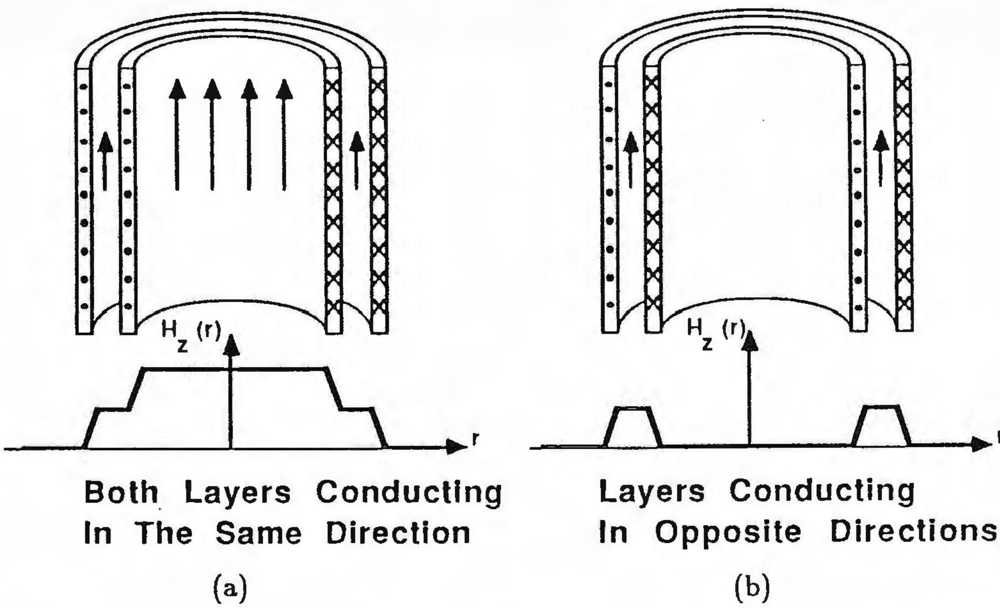

Figure 3.7: Field distribution inside an infinitely long two-layer solenoid with (a) the same current density in both layers, and (b) current densities of equal magnitude but opposite direction in the two layers. The lengths of the arrows are proportional to the strength of the magnetic field in the different regions.

from the center axis. Thus the winding space of the infinite solenoid, which includes the layers of conducting material and the spaces between them, contains the flux which is of particular interest to us because it is directly analogous to the leakage flux in a transformer.

To apply the infinite-solenoid model to the transformers that are of interest here, particular relationships are assumed between the magnetic fields generated by each of the two layers of the infinite solenoid. If $n_1 = n_2$ and $I_{1,DC} = I_{2,DC}$, then the two layers can be viewed as simply two series-connected layers of a single winding. This is the type of problem, namely one of single-winding multilayer series-connected solenoids, that M. P. Perry examines in [14]. In this instance, the equal magnetic-field contributions of the two layers $n_1 I_{1,DC}$ and $n_2 I_{2,DC}$ add, resulting in the field distribution shown in Fig. 3.7(a). If, however, the direction of the current in the inner layer is reversed such that $n_1 I_{1,DC} = -n_2 I_{2,DC}$, the magnetic field contributions of the two layers oppose each other, producing the net magnetic field distribution shown in Fig. 3.7(b). This case is similar to the condition of instantaneously equal and opposite ampere-turns in the windings of a transformer, where it is significant to note that the magnetic field inside the inner layer is completely canceled to give zero magnetic field intensity.

3.1.2.3 The Effect of a Magnetic Core on a Two-Layer Infinite Solenoid

The next step in developing a model for a real transformer is to place magnetic core material inside of the infinite solenoid as illustrated in Fig. 3.8. If that core has infinite permeability, it "forces" equal and opposite ampere-turns in the winding layers of the solenoid at all instants of time. This is shown on the characteristic curve of B versus H for the core material in Part (a) of the figure at an arbitrary time when the core flux density is at $B_{core}(t)$ and the net magnetic field intensity $H_{z,core}(t) = n_2 I_{2,DC} - n_1 I_{1,DC} = 0$.[2] Only such ideal, infinite-permeability transformer cores are considered in this report, but they are good approximations for real cores as long as the component of primary current which excites the core is small relative to the component of primary current which supplies the loads.

The effect of a low-permeability core on the magnetic field distribution across the infinite solenoid is shown in Fig. 3.8(b). "Low" permeability is defined as any permeabiltiy that produces an exciting current of the same order of magnitude as the component of primary current that supplies the loads. With a low-permeability core, the net field in the center of the solenoid is not zero. In fact, it is a function of the flux density B in the core, which depends upon the history of the voltage applied to the core. At the particular instant t_1 shown in the figure, the core flux density is at $B_{core}(t_1)$, and the B versus H characteristic of the core material requires that the net magnetic field intensity be $H_{z,core}(t_1)$. With the current directions shown, this net magnetic field intensity can only be achieved by having the field produced by the outer winding layer greater than that produced by the inner winding layer by just this amount, that is, $H_{z,core}(t_1) = |n_2 I_{2,DC}(t_1)| - |n_1 I_{1,DC}(t_1)|$. This situation is shown in the associated plot of $H_z(r, t_1)$ versus r, where the magnetic field intensity inside the inner winding is not zero but varies in direct proportion to the flux density in the core. For the outer winding to contribute a larger component of field intensity inside the core than the inner winding, as shown in the figure, the outer winding must be connected to a source while the inner winding may be connected to a load. The case of a low-permeability core is not considered further in this report.

In summary, for an infinite solenoid having any number of concentric layers, no magnetic field is produced outside the solenoid for any combination of currents flowing in the layers. In contrast, the magnetic field in the space enclosed by the innermost layer depends on the currents flowing in all the layers, and it is zero only if the net field intensity—or mmf—produced by all the currents is zero. Because the material characteristics of a high-permeability magnetic core require a transformer to operate with essentially zero net mmf, the requirement of zero net mmf is imposed on a multilayer infinite solenoid when modeling such a transformer.

---

[2]The magnetic path length is implicit in n_1 and n_2, which have units of turns per meter.

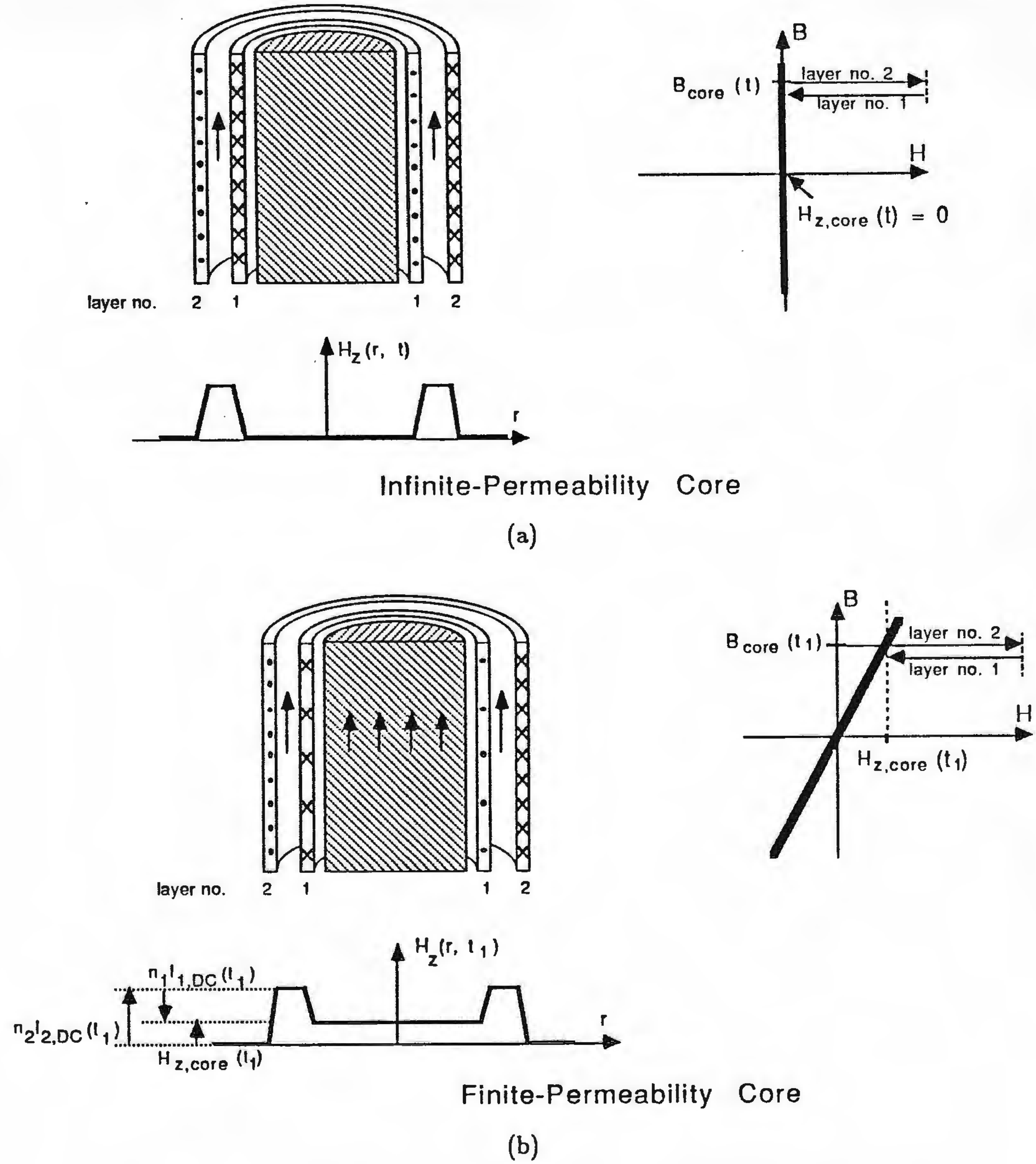

Figure 3.8: For an infinitely long two-layer solenoid containing a magnetic core, the field distribution in the winding space and the B versus H characteristic for (a) infinite-permeability core material and (b) finite-permeability core material. The horizontal vectors associated with the B versus H curves represent the magnetic field intensity in the center of the solenoid produced by each of the two winding layers. The difference between the horizontal vectors gives the magnetic field intensity inside the inner winding layer.

3.1.3 Field Distribution with AC Current

Since the discussion to this point concerns only direct currents in the layers of the solenoid, the magnetic field intensity changes linearly with radius over the height of the current-carrying layers of the solenoid. This is not the case when the currents in the solenoid are varying in time. When the excitation frequency becomes sufficiently high, or the conductor size becomes sufficiently large, skin and proximity effects force the current in the conductors to flow primarily near the surfaces of the conductors. This change in current density also changes the profile of the magnetic field intensity across the height of the conductive layers. These shifts in the distributions of the current density and the magnetic field intensity inside the conductors appear at the terminals of the solenoid—or at the terminals of the transformer that it models—as a change in the characteristic impedances between the various windings of the device.

Although the distribution of the magnetic field in the interior of the conductors varies with excitation frequency, the magnetic field intensity that any one layer contributes to the net magnetic field in the space between winding layers is independent of frequency. The field between layers is a function only of the *net* current in each of the surrounding layers. As long as the net current in each layer of conductors remains constant for changes in excitation frequency, the magnetic field in the spaces between the layers is independent of frequency. The skin and proximity effects, which cause the nonuniform distribution of current and the nonlinear profile of magnetic field intensity in the conductors, are discussed qualitatively in the next section.

3.2 EDDY-CURRENT EFFECTS IN INFINITE SOLENOIDS

The basic issues of magnetic-field analysis are addressed in Section 3.1, which describes the field-intensity distribution in an infinite solenoid excited by direct current. The nonuniform distribution of current that occurs as the excitation frequency increases is mentioned, but so far there has been no effort to explain its causes or to quantify the severity of its impact on circuit characteristics.

With this background in place, skin and proximity effects can be introduced into the analysis of the infinite solenoid. These effects have the same impact on the layers of this infinite solenoid as they do on the windings of transformers. Namely, an increase in excitation frequency causes an increase in the loss in the winding layers and a reduction in the total amount of energy stored in the magnetic field that exists in the winding layers.

3.2.1 Skin Effect

An isolated conductor carrying alternating current $i(t)$ generates a time-varying circular magnetic field $H(t)$ which exists both inside and outside the conductor. Such a conductor and its associated field are shown in Fig. 3.9.

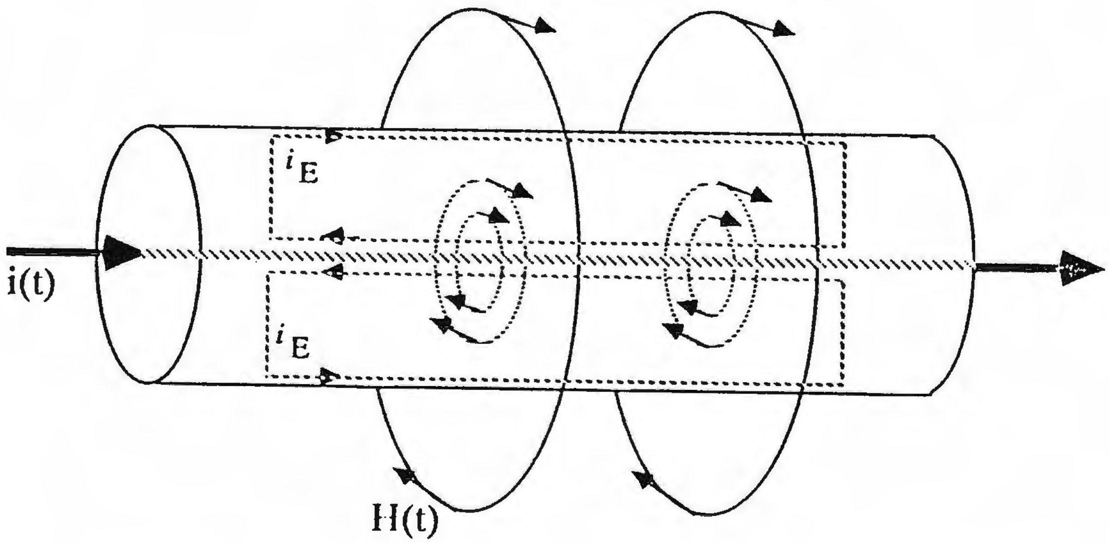

Figure 3.9: Skin effect in a conductor carrying an alternating current $i(t)$. The alternating current creates the circularly directed magnetic field shown as solid-line circles outside the conductor and as dotted-line circles inside the conductor. The time-varying magnetic field inside the conductor induces the eddy current i_E shown as circulating around the dashed rectangular paths. At the instant shown, the current $i(t)$ is increasing in the direction indicated. The net instantaneous current flowing in the conductor is unchanged by the eddy currents, but the distribution of the current over the cross section of the conductor changes.

The circular alternating field inside the conductor induces eddy currents i_E in the conductor which are directed to produce a field that partially cancels the "main" alternating field produced by the time-varying current. These induced eddy currents are directed such that they add to the main current on the surface of the conductor and subtract from it in the interior region. The superposition of the main alternating current and the induced eddy currents results in a decrease in the current density in the interior of the wire and an increase in the current density near its surface. Because the intensity of the induced eddy currents is directly proportional to the rate of change of the main current, the nonuniform distribution of the current in a conductor is more pronounced for higher excitation frequencies. This change in the current-density distribution caused by the time-varying current in the wire is the phenomenon usually referred to by the term *skin effect* in current-carrying conductors.

3.2.2 Proximity Effect

The nonuniform current distribution over the cross section of a conductor attributed to skin effect is due solely to the time-varying magnetic field generated by the current in the conductor itself. Another frequency-dependent eddy-current phenomenon occurs in any conductor that is placed in a region of space containing a time-varying magnetic field that has a component normal to the axis of the conductor. Since a conductor located close to a wire that carries alternating current experiences such an externally imposed magnetic field, this eddy-current phenomenon is often called the *proximity effect*. It would be more accurate perhaps to call this the *external-field effect* since it is actually the presence of the time-varying magnetic fields generated by nearby windings that causes the so-called proximity effect. In this document, however, the common term *proximity effect* is used.

Whenever a conductor is located in a region of space that contains an alternating magnetic field which is directed normal to the axis of the conductor, there are eddy currents induced in the conductor which act to oppose the penetration of this external field. Fig. 3.10 shows such a situation for a conductor with a circular cross section in a uniform time-varying magnetic field that is normal to the axis of the conductor. The conductor is isolated in space and carries no net current. The uniform external field H_{ext} in Fig. 3.10 is assumed to be increasing in magnitude in the indicated direction. The time-varying field lines which pass through the conductor induce eddy currents in the conductor, and these eddy currents are directed to oppose the increasing magnetic field. In Fig. 3.10(a), the eddy currents are shown as circular currents which surround each of the crosses that represent the downward directed external field H_{ext}.

The cross-sectional view of the conductor in Fig. 3.10(c) shows that the net effect of the induced eddy currents is the generation of a circulating current that flows into the right side of the cross section and out of the left side. The upwardly directed arrows in this cross-sectional view show the opposing magnetic field generated by the eddy currents. The superposition of this reaction field and the external field that induces it results in a reduction in the net amount of magnetic flux that penetrates the conductor. Since the energy stored in the magnetic field in any region of space is directly related

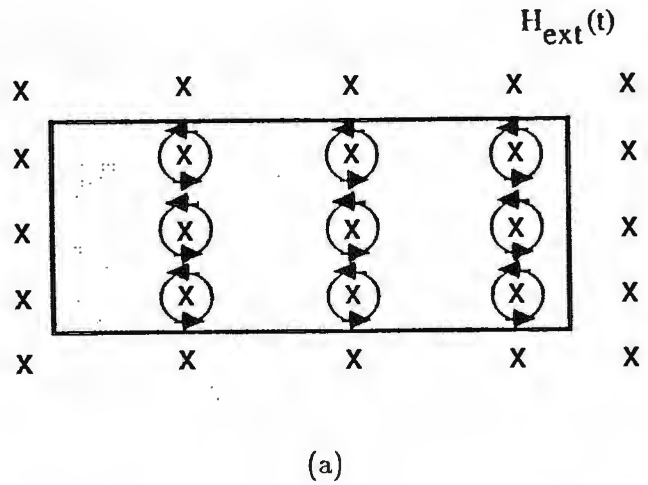

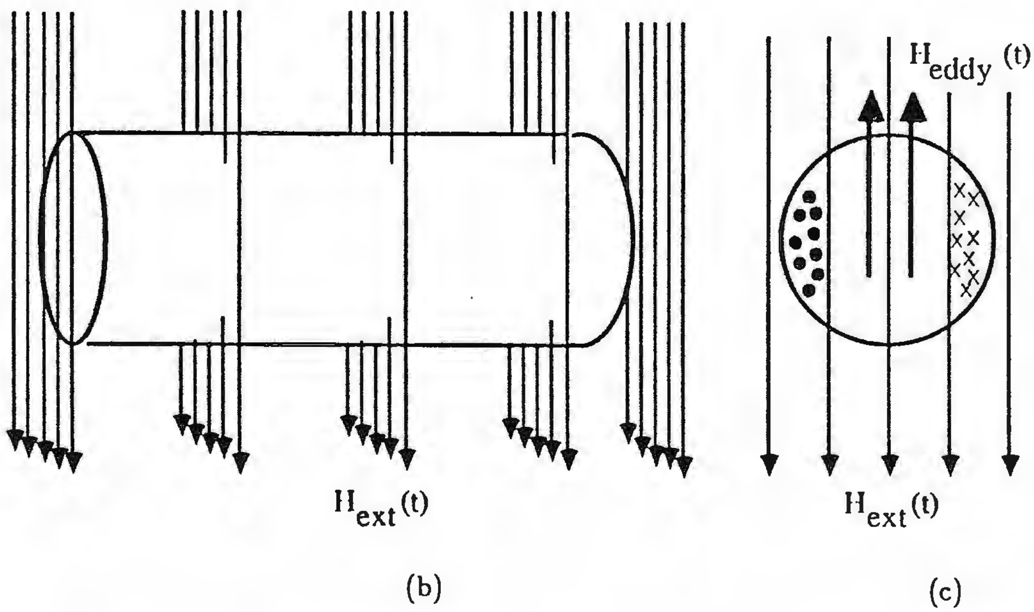

Figure 3.10: Proximity effect for a cylindrical conductor in a uniform time-varying magnetic field. (a) Top view, showing an eddy current induced around each field line that passes through the conductor (b) Side view. (c) Cross-sectional view, showing the net opposing field H_{eddy} generated by the eddy currents.

to the magnetic field intensity there as explained in Section 3.3.2, a reduction in the magnetic flux that penetrates a conductor corresponds to a reduction in the magnetic energy stored in the conductor.

3.2.3 Combined Frequency Effects

Skin and proximity effects are combined when a conductor that carries an alternating current is placed in an external alternating field. This is exactly the situation that exists for the conductors in the layers of an infinite solenoid when these layers carry time-varying currents, and the same situation exists for transformer windings. The essence of the combination of these effects is that the current in each layer of conductors produces a skin effect in itself and produces a proximity effect in other conductors that are close to it.

While the infinite solenoid is the object of this analysis, a structure which has an infinite number of conductors in each layer, all carrying the same current, skin and proximity effects are just as evident in two side-by-side conductors. Figure 3.11 illustrates the combination of these effects for two round conductors located next to each other when the conductors carry currents in opposite directions. Parts (a) and (b) of the figure show the effects of the individual left-hand and right-hand currents respectively; Fig. 3.11(c) shows the combined effects of the two currents. For this case of two side-by-side conductors that carry currents in opposite directions, the current in either of the conductors tends to flow mostly on the skin of the conductor and more on the side nearest to the other conductor as shown in the figure.

Figure 3.12 shows the individual and combined effects of currents in the same direction in two side-by-side conductors. This figure shows that for two conductors carrying current in the same direction, the currents tend to flow mostly on the skin of the conductors and more on the side furthest from the other conductor. From the density of the magnetic field lines in Fig. 3.11(c) and Fig. 3.12(c), it can be seen that, in both cases, the current in the conductors is concentrated in the region of highest flux density.

When layers of conductors which all carry the same current are located next to each other, the combined eddy-current effects cause the current-distribution patterns illustrated in Fig. 3.13. The situation for two layers of conductors which carry current in the same direction is shown in Fig. 3.13(a); Fig. 3.13(b) shows the situation for two side-by-side layers which carry oppositely directed currents. As with the single conductors in Figs. 3.11 and 3.12, the currents in the layers of Fig. 3.13 concentrate in the region of highest magnetic flux density. This fact is important to remember when considering the current distribution in the winding layers of an infinite solenoid or a transformer.

This entire discussion of eddy currents concerns alternating magnetic fields. An alternating magnetic field induces the eddy currents that cause the nonuniform distribution of the current over the cross section of the conductors. For direct current flowing in the conductors, the magnetic field patterns in Figs. 3.11 to 3.13 would be similar to those shown, but there would be no crowding of current in the conductors in the regions of highest field strength. Instead, the current density would be uniform across all the

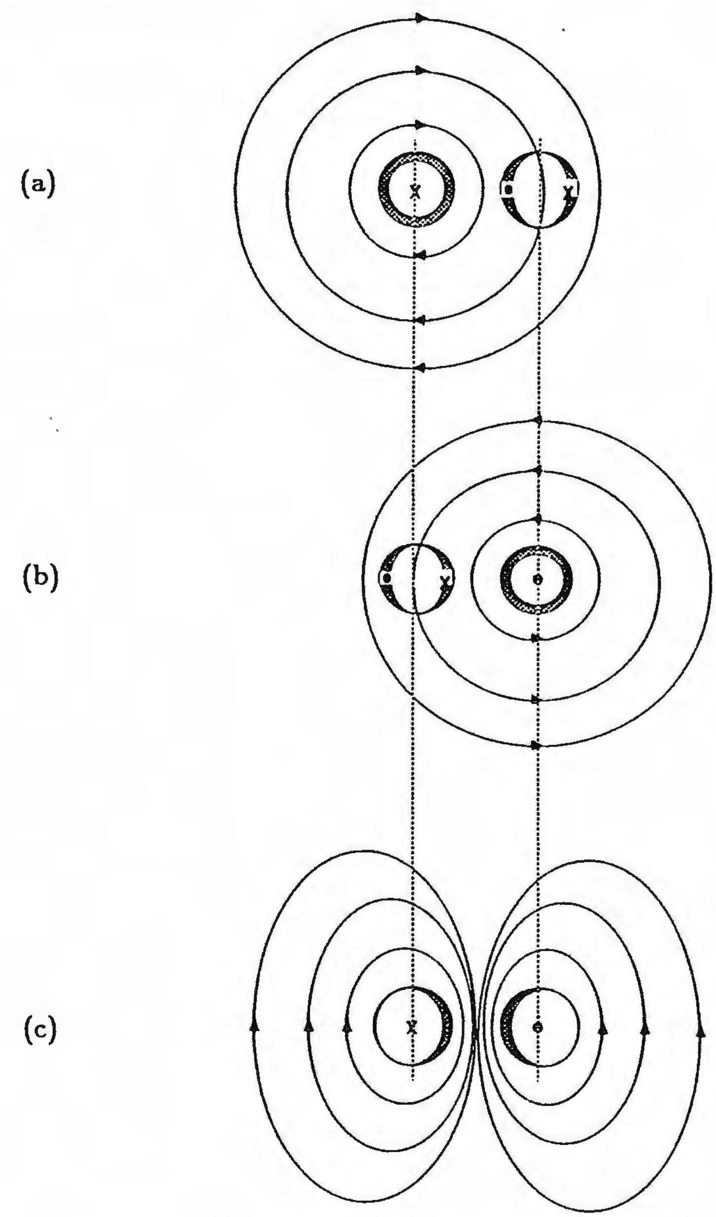

Figure 3.11: Combined skin and proximity effects in two side-by-side round conductors that carry time-varying currents in opposite directions. Dark regions show areas of high current density. (a) The effect of a current in the left-hand conductor. (b) The effect of an oppositely directed current in the right-hand conductor. (c) The combined effects of the two currents.

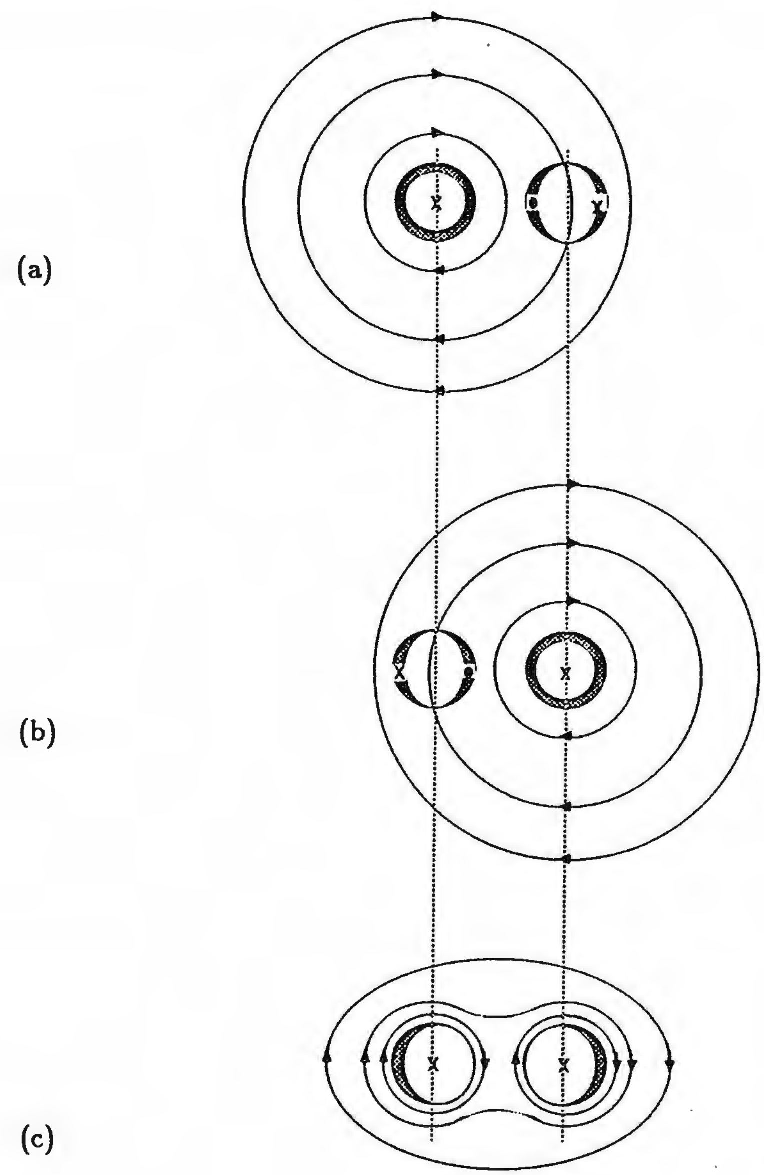

Figure 3.12: Combined skin and proximity effects in two side-by-side round conductors that carry time-varying currents in the same direction. Dark regions show areas of high current density. (a) The effect of a current in the left-hand conductor. (b) The effect of an equal current in the right-hand conductor. (c) The combined effects of the two currents.

(a)

(b)

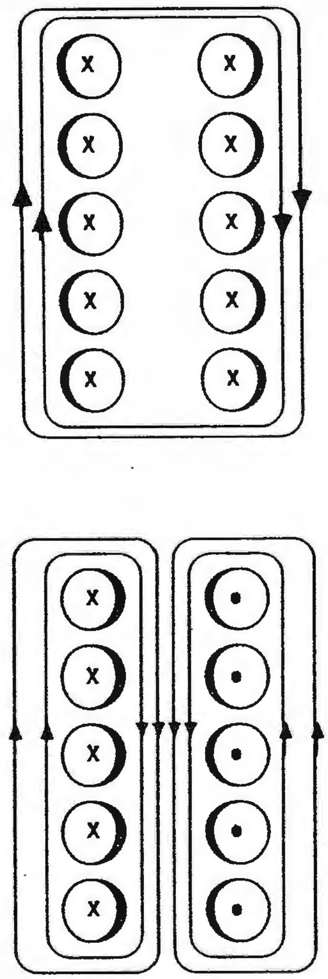

Figure 3.13: Simplified view of the combined skin and proximity effects in two side-by-side layers of conductors which carry time-varying currents. (a) Approximate effect of equal currents in the same direction in the two layers. In reality, the field lines are not straight and they do not entirely cancel in the region between layers. (b) The approximate effect of equal but oppositely directed currents in the two layers.

conductors.

It is also important to realize that the net magnetic field between the layers of conductors is assumed to be tangential to the layers. This is usually true near the "middle" of a winding layer with respect to the z-direction in Fig. 3.5, but it is less likely to be true at the ends of the layer. As stated in Section 1.1.2, this *parallel-field* assumption is critical to the analysis developed in Part I of the present document.

3.2.4 The Effect of the Field Distribution on Impedance Values

The crowding of current due to the effects of time-varying magnetic fields increases the effective resistance of a wire. The resistance R of any wire is given by

$$R = \frac{l}{\sigma A} \tag{3.15}$$

where l is the length of the wire, σ is the conductivity of the material, and A is the effective cross-sectional area of the conductor. Since current tends to flow only near the surface of the conductor as the frequency of the sinusoidal magnetic fields increases, the effective cross-sectional area of the wire decreases, which causes an increase in the resistance of the wire.

The relationship between the current distribution in the conductors and leakage inductance can be explained qualitatively as follows. The eddy currents induced near the surfaces of the conductors contribute to the magnetic field in a direction that tends to oppose the penetration of the external flux into the conductors. As a consequence, the magnetic field intensity inside the conductors is reduced. A lower magnetic field intensity produces less energy storage, which corresponds to a lower leakage inductance.

The distribution of magnetic field intensity for dc or low-frequency excitation in an infinite solenoid is developed in Section 3.1.2. Figure 3.4 in that section shows that the current distributes evenly across the solenoid layer at low frequencies and the magnetic field intensity for such a low-frequency case changes linearly across the height of each winding layer. When the frequency of the layer currents increases, however, skin and proximity effects combine to cause the current to crowd toward the surfaces of the conductors in the regions of highest flux density. This redistribution of current in the conductors of a winding layer acts to shield the interior of the layer from the time-varying magnetic fields, which means that at high frequencies, the total amount of energy stored in the magnetic field that exists in any winding layer is lower than it is with low-frequency excitation.

The decrease in the average magnetic energy stored in and around the layers of any two windings under short-circuit conditions correlates to a decrease in the leakage inductance between those two windings. One of the main objectives of the analysis in the next chapter is to develop analytical expressions for the variation of the magnetic field and the current density in a layer of conductors as a function of the excitation frequency. Such results are then used to formulate expressions for the frequency-variation of the characteristic impedance between each pair of windings in a multiwinding transformer.

3.3 CURRENT-SHEET APPROXIMATION OF A WINDING LAYER

The analysis described so far establishes the groundwork needed to solve for the spatial distribution of the magnetic field intensity and current density in the winding layers of an infinite solenoid, and for the magnetic field intensity between the winding layers, under conditions of high-frequency sinusoidal excitation. In Section 3.3.1 below, the problem of calculating these distributions is set up to be solved in the next chapter. There, it is seen that the current-density and field-intensity distributions are determined solely by the phasor values of the magnetic field intensity that exist at the surfaces of the winding layers. Section 3.3.2 then tells how the solutions for the magnetic-field-intensity and current-density distributions can be used to find the power dissipation and magnetic-energy storage in the layers.

3.3.1 Modeling an Infinite Cylindrical Layer as an Infinite Current Sheet

In an infinitely long cylindrical winding layer, the magnetic field intensity depends only on the distance r from the center axis and is directed purely in the z-direction. The general expression in cylindrical coordinates for a three-dimensional time-varying magnetic field intensity function $\mathbf{H}(r, \phi, z, t)$ can be written as simply $\mathbf{H}_z(r, t)$. When the excitation currents are sinusoidal, the magnetic field intensity can be written as a vector phasor field, representing a vector field in which all magnitudes vary sinusoidally with time. In symbols, $\underline{\mathbf{H}}(r) = \underline{H}_z(r)\hat{\mathbf{a}}_\mathbf{z}$ where $\underline{H}_z(r)$ is a scalar complex phasor which is a function of the radius coordinate r, and $\hat{\mathbf{a}}_\mathbf{z}$ is the unit vector in the z-direction.[3]

The above assumptions permit us to solve for the current distribution in the winding layers using Maxwell's equations written in their one dimensional form for cylindrical coordinates. M. P. Perry presents such an analysis in [14] where he shows that for the cylindrical current sheet problem, the current density in a winding layer can be written in terms of Bessel functions. Perry also argues, however, that it is often possible to neglect the curvature in the cylindrical winding layers and simply treat the layers as current sheets that extend infinitely in the direction of depth. He asserts that the curvature of the winding layers can be neglected if "the conductor thickness (designated here the layer *height* h_{cu}) is small compared to the total coil diameter [14, p. 118]." Figure 3.14 shows a cylindrical current sheet which is modeled by an infinite rectangular current sheet. Looking down at the top of any particular part of the cylindrical sheet as shown in Fig. 3.14(b), it seems reasonable that as long as the curvature of the surface of the cylinder is relatively small, each local section of the cylindrical conductor can be approximated by a flat surface without introducing substantial error. If such an approximation is valid, the winding layers can be analyzed as current sheets in rectangular coordinates, which is substantially easier than the analysis in cylindrical coordinates. It is seen later

[3] See Section 1.3 for a discussion of the use of phasor notation.

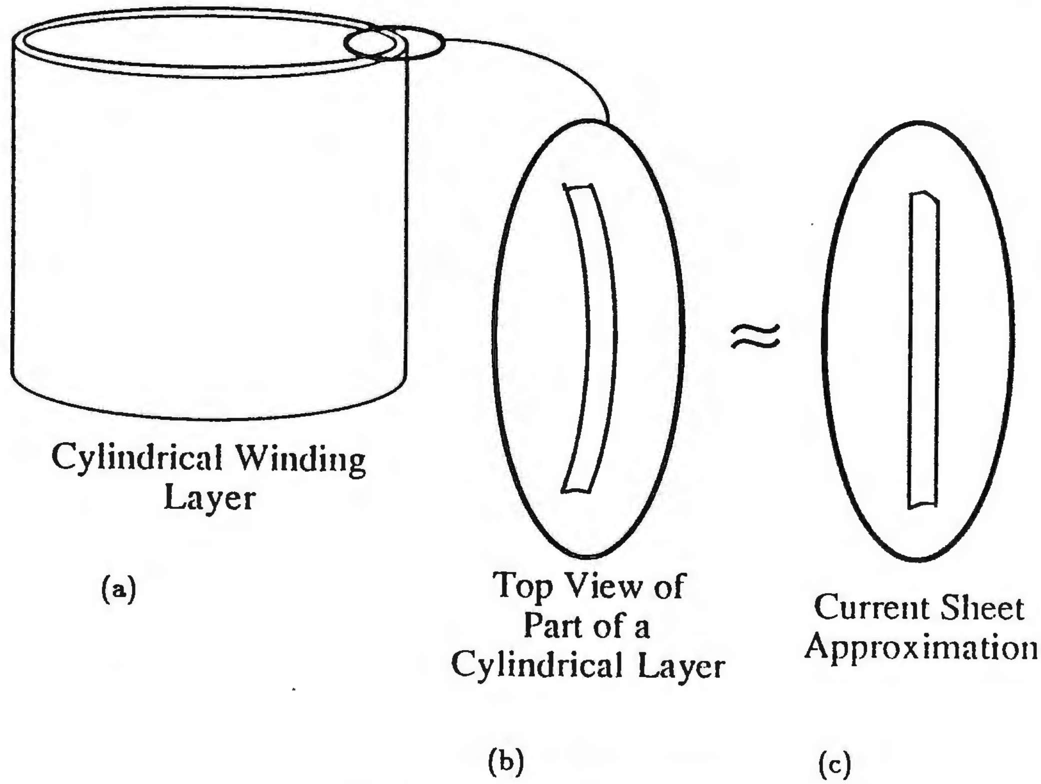

Figure 3.14: (a) Cylindrical layer of an infinite solenoid. (b) Detailed top view of the cylinder. (c) Infinite current sheet used to approximate the layer if the radius of the cylinder is large relative to the height of the layer.

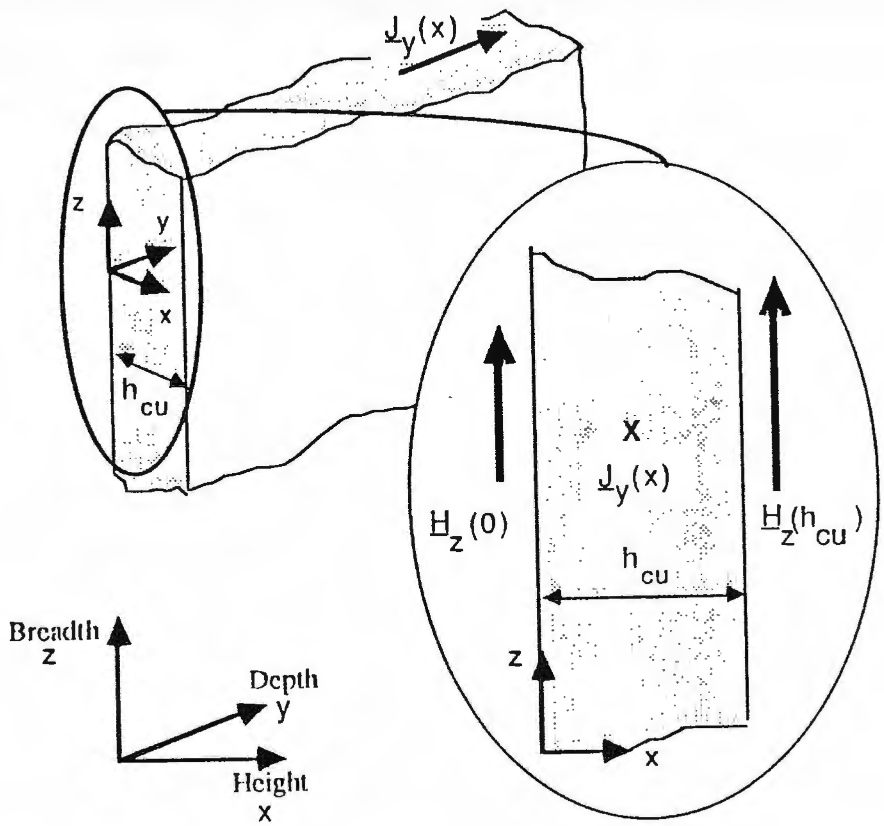

Figure 3.15: Model of an infinite current sheet. The sheet extends to infinity in the y (*depth*) and z (*breadth*) directions. The *height* of the sheet is shown as h_{cu} in the x-direction.

in this report that the results of a rectangular-coordinate analysis can be written in terms of hyperbolic sines and cosines instead of Bessel functions. In this document, it is always assumed that the radius of curvature of any winding is much larger than the height of the conductors; therefore, only rectangular coordinates are used.

For the current-sheet approximation, a general three-dimensional time-varying magnetic field intensity function is written as $\mathbf{H}(x, y, z, t)$ where the x, y, z directions are as defined as the height, depth, and breadth, respectively, as shown in Fig. 3.15.

For sinusoidal excitation, phasor notation is used to represent the time-varying magnetic field intensity $\mathbf{H}(x, y, z, t)$. The result is the vector phasor function $\underline{\mathbf{H}}(x, y, z)$ of the x, y and z coordinates. As the magnetic field intensity in an infinitely long conducting cylinder is a function of the radius r only, in the infinite current sheet it is a function of the x-direction only as defined in Fig. 3.15. Therefore, in the one-dimensional case, $\underline{\mathbf{H}}(x, y, z)$ is written as simply $\underline{H}_z(x)\hat{\mathbf{a}}_\mathbf{z}$.

3.3.2 Power and Magnetic-Energy Density in a Region of Space

The motivation for modeling a round-wire or other physically realizable winding as an infinite conductor is that Maxwell's field equations can be solved analytically for such a simple geometry. Further, the motivation for solving these equations explicitly lies in the following basic equations that relate the current density and magnetic field intensity in space to the amount of dissipated power and stored energy, respectively, in that space. From electromagnetic theory, in any conductor with conductivity σ and permeability μ, the power $p_d(t)$ dissipated per unit volume and the energy $w_m(t)$ stored in the magnetic field per unit volume are given by

$$p_d(t) = \frac{|\mathbf{J}(t)|^2}{\sigma} \tag{3.16}$$

$$w_m(t) = \frac{\mu |\mathbf{H}(\mathbf{t})|^2}{2} \tag{3.17}$$

The task of finding the power dissipation and magnetic-energy storage in any winding space reduces, therefore, to solving for the current density **J** and the magnetic-field intensity **H** in that winding space, and evaluating the volume integrals of (3.16) and (3.17) over the space. In this chapter, it is shown how the frequency-independent values of **H** are calculated for the interlayer spaces of a transformer winding structure. Because **H** is uniform in each interlayer space, the corresponding volume integral of (3.17) is trivial. Of course, no current flows in the interlayer spaces, making p_d zero there.

Inside the conductors, the current density and magnetic field intensity are complicated functions of frequency. By modeling each cylindrical winding layer as an infinite current sheet, it is possible to derive expressions which give the field distribution in each layer of conductors based solely on the thickness of the layer and the magnetic field intensity **H** at the two surfaces of the layer, determined by the methods of this chapter. The derivation for the magnetic field intensity **H** and the current density **J** in an infinite current sheet is carried out in the next chapter. Afterwards, the volume integrals of (3.16) and (3.17) can be calculated for the winding layers as well as the interwinding spaces, and the total power dissipation and energy storage are thus obtained. Then the goal of this analysis can be addressed: deriving expressions for the high-frequency impedances between the windings of actual transformers.

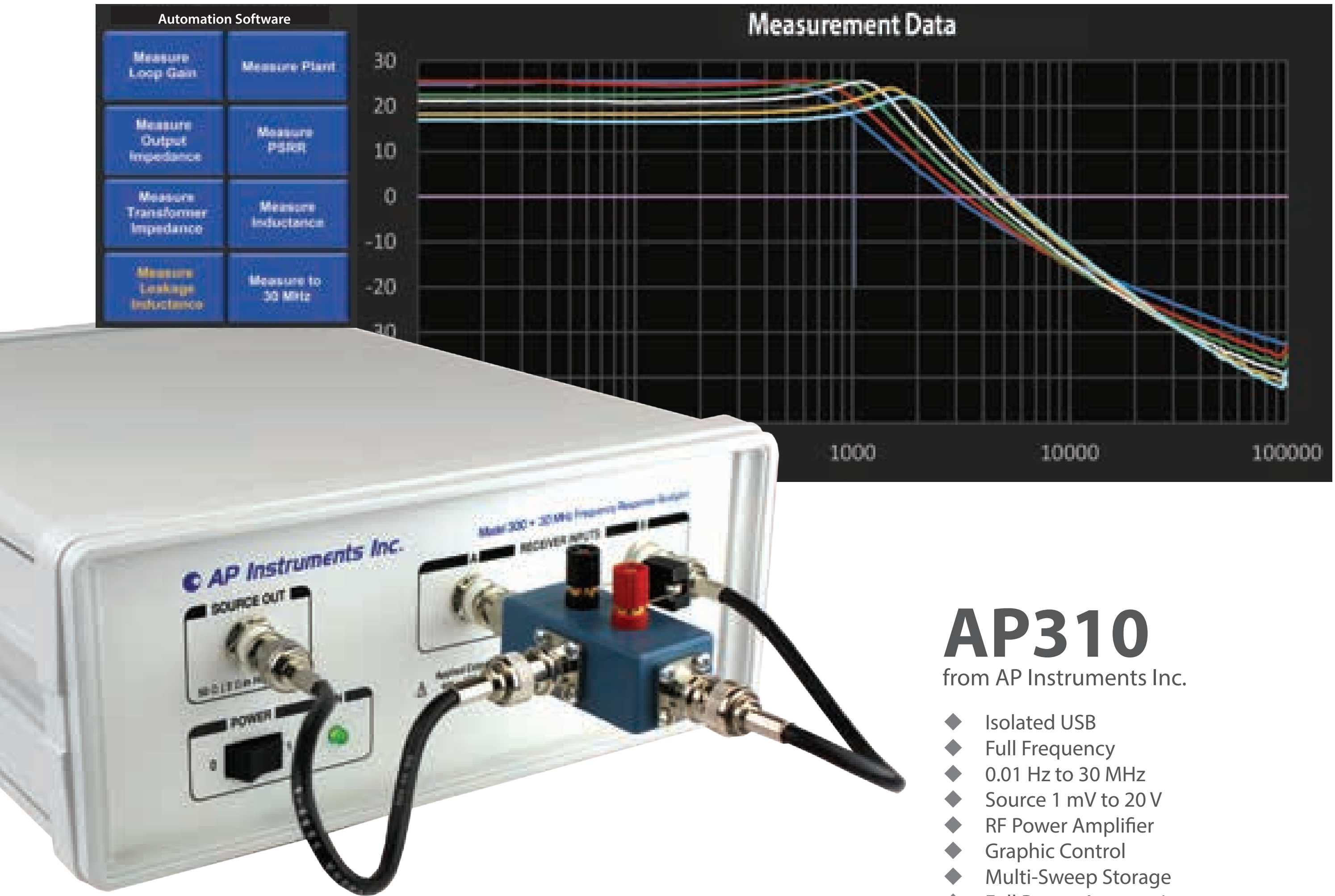

AP310

from AP Instruments Inc.

- Isolated USB
- Full Frequency
- 0.01 Hz to 30 MHz
- Source 1 mV to 20 V
- RF Power Amplifier
- Graphic Control
- Multi-Sweep Storage
- Full Range Accessories
- Maximum Productivity
- Fully-Automated Loop Design
- Support from Industry Experts
- Easy to Use
- One-Button Setup

AP310 is the industry's only full-featured frequency response analyzer designed specifically for power supplies. Enhance the experience with RidleyWorks® software for seamless integration between power supply design and measurement. *Made in California since 1995.*

RIDLEYENGINEERING.COM

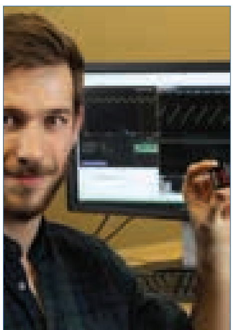

Workshops

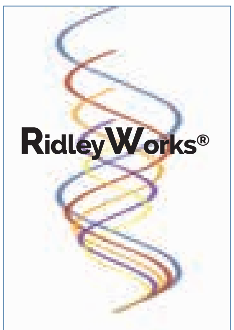

Design Software

Analyzer

Design Ideas

RIDLEY ENGINEERING

601 E Daily Drive, Suite 112 | Camarillo CA 93010 | info@ridleyengineering.com | +1 805 504 2212 | POWER SUPPLY DESIGN CENTER GROUP on FaceBook

Full Range Measurements

0.01Hz Minimum frequency
for PFC measurement
30 MHz Maximum frequency
for full magnetics characterisation
117 dB Dynamic range
Exceptional performance
for high-noise environments,
challenging impedance and PSRR

Power Amplifier Output

1 mV Minimum source value
for sensitive systems
20 V p-p Source for high-power
and high-drive systems
2 Ohm Output impedance
500 mA Current capability
Self protected from damage

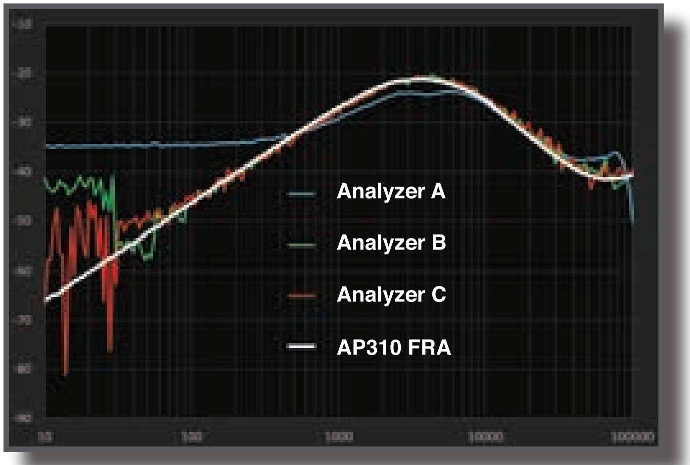

Full Calibration and Certification

Z540-1 Military calibration and certification with full data
NIST Calibration and certification with full data
2-year warranty

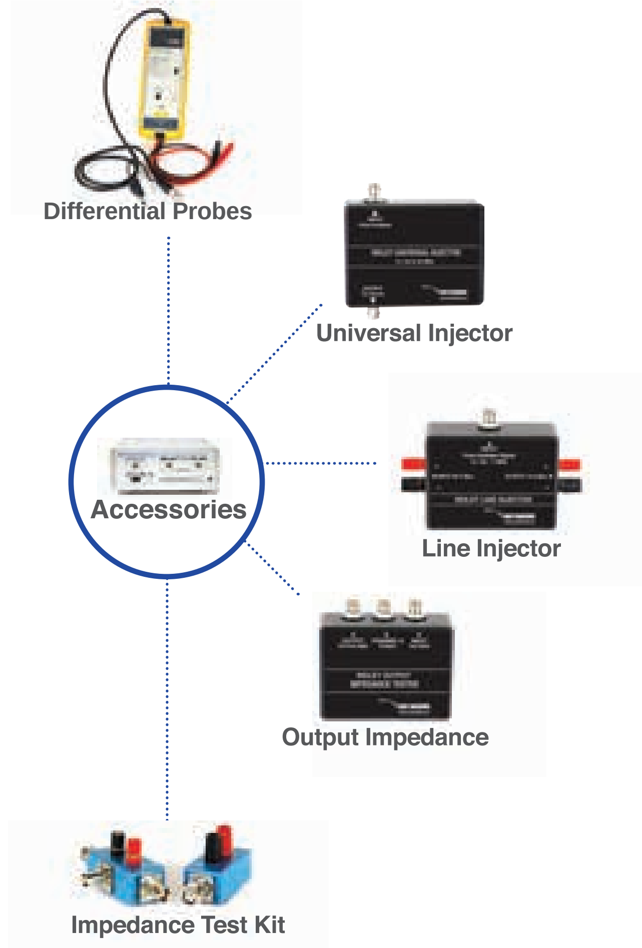

Chapter 4

Field Solution for an Infinite Current Sheet

To arrive at expressions for the energy storage and power dissipation within the winding space of a transformer structure, we must first obtain expressions for the magnetic-field-intensity and current-density distributions within each winding layer. However, when the windings of a transformer are excited with ac currents, the magnetic field intensity and current density within the conductors become distributed in a complicated and nonuniform fashion. As a result, we must resort to analyzing the distribution of the magnetic field intensity and current density by applying Maxwell's field equations. As argued in Chapter 3, we can model a given layer of a transformer winding structure as an infinite current sheet. Therefore, in this chapter we apply Maxwell's equations to an infinite current sheet and arrive at analytical expressions that approximately describe the magnetic-field-intensity and current-density distributions within transformer windings. We then make a detailed investigation into the peculiar nature of these distributions through an extensive array of examples and graphical illustrations. Finally, using the expressions for the magnetic-field-intensity and current-density distributions, we derive expressions for the average power dissipation and average energy storage per square meter for an infinite current sheet.

4.1 APPLICATION OF MAXWELL'S EQUATIONS TO THE INFINITE CURRENT SHEET

4.1.1 Description of Problem

Figure 3.15 shows the infinite current sheet we use to model the cylindrical winding layer. In this figure, a set of axes designates the coordinate system that applies to the following analysis. The origin of the system is located at the left-hand side of the current sheet. The x-coordinate axis is in the direction of layer height; the y-direction is normal to the indicated cross section of the current sheet and lies along the direction of depth; and the

z-axis is in the direction of breadth. The infinite sheet has a height designated as h_{cu}. To analyze the fields in such a current sheet, we need only the following assumptions:

- The current density and the magnetic field intensity vary sinusoidally with time.
- The media are linear.
- The magnetic field at the surfaces of the sheet are directed purely in the breadth or z-direction. That is, $\underline{\mathbf{H}}(x, y, z) = \underline{H}_z(x)\hat{\mathbf{a}}_z$ where $\hat{\mathbf{a}}_z$ is the unit vector in the z-direction. The boundary values of this field are given as $\underline{H}_z(0)$ and $\underline{H}_z(h_{cu})$.
- The current sheet is long enough in the breadth and depth directions that the spatial variation of the magnetic field depends only on changes in the x-direction, which is to say that the magnetic field is determined by the height, or x-coordinate, and does not vary with changes in depth or breadth. This is an alternate statement of the infinite-current-sheet assumption.
- The current sheet is stationary with respect to the observer.

What we seek in this analysis is a method for describing the fields inside the conductive sheet of a material with conductivity σ and permeability μ that is based only on the values of the sinusoidally varying magnetic fields on the surfaces of the sheet. This type of boundary-value problem where the spatial magnetic field intensity decreases as the field penetrates the material is the same mathematically as the problem of the diffusion of heat or gases into a medium where the surface temperature or gas concentration is made to vary sinusoidally with time. The mathematical statement of the differential equation that defines this problem is sometimes referred to as *the diffusion equation*, and we shall use this term in the analysis which follows.

4.1.2 Derivation of the Diffusion Equations

The diffusion equation for the case of sinusoidal steady-state variations of the electric field $\mathbf{E}$ is derived in Appendix A in terms of the the complex wave number $\underline{k}$ and the complex vector phasor $\underline{\mathbf{E}}$ as

$$\nabla^2 \underline{\mathbf{E}} = \underline{k}^2 \underline{\mathbf{E}} \tag{4.1}$$

where the complex wave number is a material characteristic given by

$$\underline{k} = \sqrt{j\omega\mu\sigma - \omega^2\mu\epsilon}. \tag{4.2}$$

In the *good conductor* case—which is the only case of importance here—the permittivity ϵ and the permeability μ are given by their free-space values $\epsilon_o = 8.854 \times 10^{-12}$ F/m and $\mu_o = 4\pi \times 10^{-7}$ H/m , respectively. Since the conductivity σ is far greater than the product of the permittivity of free space ϵ_o and the angular frequency ω, we can assume, for any frequency of interest in our analysis[1], that $\omega\mu_o\sigma \gg \omega^2\mu_o\epsilon_o$. Therefore, for a good conductor, we can write the complex wave number as

$$\boxed{\underline{k} \approx \sqrt{j\omega\mu_o\sigma}} \tag{4.3}$$

Using the relation for the square root of j

$$\begin{aligned} \sqrt{j} &= (e^{j\frac{\pi}{2}})^{\frac{1}{2}} \\ &= e^{j\frac{\pi}{4}} \\ &= \cos\frac{\pi}{4} + j\sin\frac{\pi}{4} \\ &= \frac{1}{\sqrt{2}} + j\frac{1}{\sqrt{2}} = \frac{1}{\sqrt{2}}(1+j) \end{aligned} \tag{4.4}$$

we can write (4.3) as

$$\underline{k} = \sqrt{\frac{\omega\mu_o\sigma}{2}}(1+j) \tag{4.5}$$

$$\boxed{\underline{k} = \frac{1}{\delta}(1+j)} \tag{4.6}$$

where

$$\boxed{\delta = \sqrt{\frac{2}{\omega\mu_o\sigma}}} \tag{4.7}$$

The expression for δ above is referred to as the *skin depth* for the conductive material at the excitation frequency ω. For any general conducting sheet with a sinusoidally varying electric field at the surface of the conductor, the magnitude of the field strength at a distance equal to one skin depth into the material is equal to e^{-1} times the value of the field at the material surface. That is, at one skin depth, the strength of the electric field is 36.8% of its value at the conductor surface; and at a depth of 3δ, the electric field strength is reduced to 5.0% of the value at the surface. The solution to (4.1) is a phasor from which the instantaneous spatial distribution of the electric field can be determined. The solution is general and applicable for any good conductor under sinusoidal steady-state field conditions.

The diffusion equation given above in (4.1) is written in terms of the electric field; an analogous relationship can be written in terms of current density $\mathbf{J}$ by using the constitutive relationship $\mathbf{J} = \sigma\mathbf{E}$. Also, Maxwell's equations can be manipulated to

[1]For copper with $\sigma = 5.315 \times 10^7$ S/m at 60°C, this assumption is good for frequencies below approximately 1×10^{12} hertz. Above this frequency, the conductivity of copper becomes frequency dependent and the simple classical analysis of this report is not valid [7].

yield a diffusion equation in terms of the magnetic field **H**; this derivation is detailed in Appendix B. The three diffusion equations are collected below.

$$\nabla^2 \underline{\mathbf{E}} = \underline{k}^2 \underline{\mathbf{E}} \tag{4.8}$$
$$\nabla^2 \underline{\mathbf{H}} = \underline{k}^2 \underline{\mathbf{H}} \tag{4.9}$$
$$\nabla^2 \underline{\mathbf{J}} = \underline{k}^2 \underline{\mathbf{J}} \tag{4.10}$$

What is important to see in the above equations is that, when there are no free charges in the conducting material, i.e., the volume charge density ρ in the material is zero, the diffusion equation is of exactly the same form for all three field quantities $\underline{\mathbf{E}}$, $\underline{\mathbf{H}}$ and $\underline{\mathbf{J}}$. This does not, however, mean that the solutions are the same because different boundary conditions apply.

For the infinite-current-sheet problem we are considering, we can make several simplifying assumptions. First, the spatial magnetic-field phasor $\underline{\mathbf{H}}(x, y, z)$ is assumed to be a function of x only and to be directed in the z-direction. Likewise, the spatial current-density phasor $\underline{\mathbf{J}}(x, y, z)$ is assumed to be a function of x only and to be directed in the y-direction. We can write these mathematically as

$$\underline{\mathbf{H}}(x, y, z) = \underline{H}_z(x)\hat{\mathbf{a}}_\mathbf{z} \tag{4.11}$$
$$\underline{\mathbf{J}}(x, y, z) = \underline{J}_y(x)\hat{\mathbf{a}}_\mathbf{y} \tag{4.12}$$

where $\hat{\mathbf{a}}_\mathbf{y}$ and $\hat{\mathbf{a}}_\mathbf{z}$ are the unit vectors in the y and z directions respectively. Then the three dimensional diffusion equations given in (4.9), and (4.10) above become the one-dimensional partial differential equations,

$$\boxed{\begin{aligned} \frac{\partial^2 \underline{H}_z(x)}{\partial x^2} &= \underline{k}^2 \underline{H}_z(x) \qquad (4.13) \\ \frac{\partial^2 \underline{J}_y(x)}{\partial x^2} &= \underline{k}^2 \underline{J}_y(x) \qquad (4.14) \end{aligned}}$$

These are the equations that we now undertake to solve.

4.1.3 Form of Solution of the Boundary Value Problem

Before we continue with the mathematical development, it is useful to pause for a moment and consider the type of solution we expect to find in the analysis that follows. Figure 4.1(a) shows as a vertically shaded plot a hypothetical distribution over the layer height of the phasor magnitude(rms value) of the magnetic field intensity in a current sheet similar to that in Fig. 3.15 that is subject to an arbitrary pair of cosinusoidal magnetic-field-intensity boundary conditions. What we seek to find in our analysis is an analytical expression for the distribution of the magnetic field—and for the related

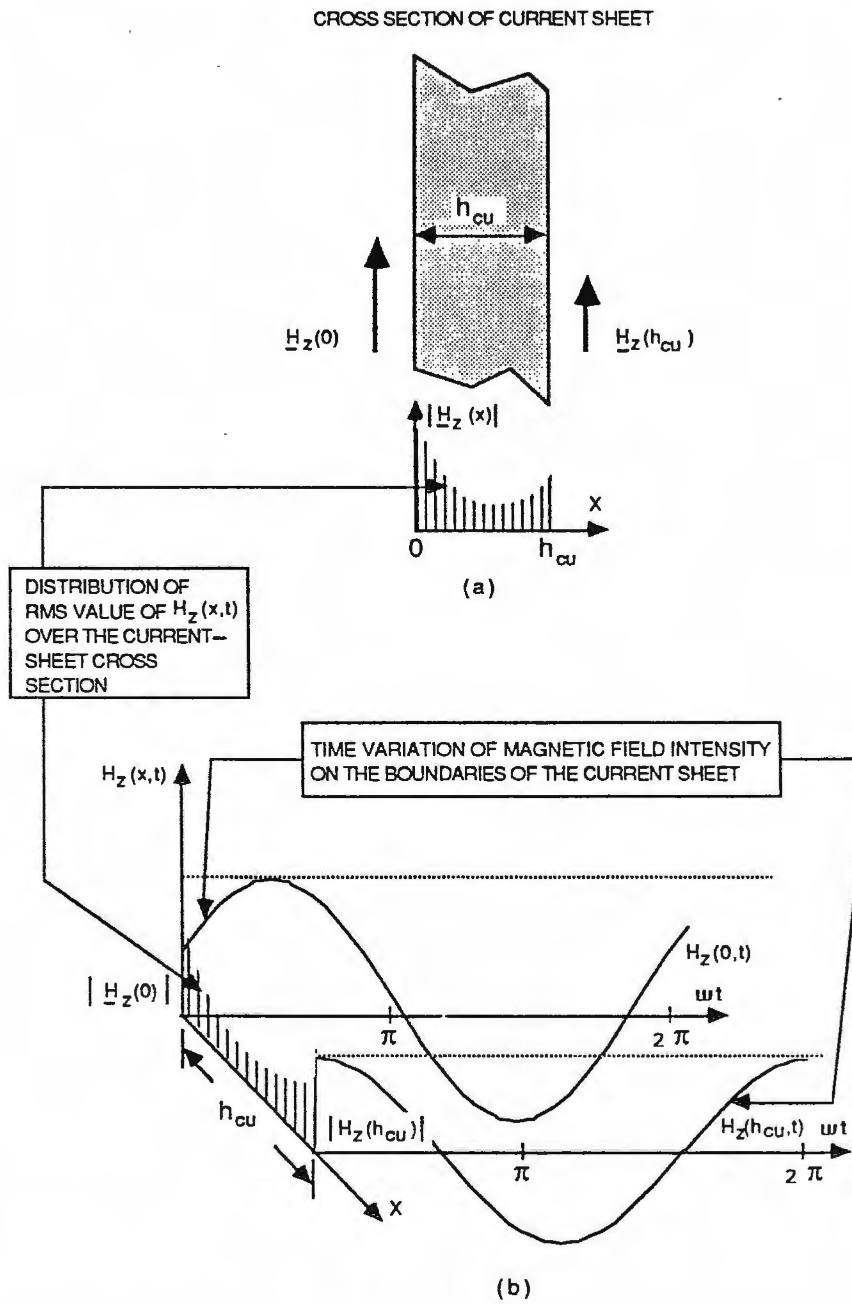

Figure 4.1: (a) Hypothetical distribution of the magnitude of the magnetic-field-intensity phasor $\underline{H}_z(x)$ across a layer of height h_{cu}. (b) The boundary conditions of the cosinusoidal waveforms $H_z(0,t) = \sqrt{2}\,|\underline{H}_z(0)|\cos(\omega t + \theta_0)$ and $H_z(h_{cu},t) = \sqrt{2}\,|\underline{H}_z(h_{cu})|\cos(\omega t + \theta_{h_{cu}})$ are shown.

current-density distribution—in a winding layer based on the excitation frequency and on the values of the magnetic field intensity at the surfaces of the conductor.

The boundary values of the magnetic field intensity play an important part in the derivations that follow, and we need to be somewhat explicit about the notation we use in describing these quantities. In part (a) of Fig. 4.1, we see a cross-sectional view of the current sheet. The arrows labeled $\underline{H}_z(0)$ and $\underline{H}_z(h_{cu})$ indicate the location of the magnetic-field-intensity phasor $\underline{H}_z(x)$ at the boundaries $x = 0$ and $x = h_{cu}$ on the two sides of the current sheet. The succession of vertical lines in the plot of $|\underline{H}_z(x)|$ versus x below the conductor cross section show how the rms value of a hypothetical phasor magnetic field might vary across the height of the layer. Part (b) of Fig. 4.1 shows in a perspective drawing two time axes on which the magnetic-field-intensity functions $H_z(0,t)$ and $H_z(h_{cu},t)$ at the boundaries of the layer are shown as cosinusoidally varying functions of time with arbitrary phase angles of θ_0 and $\theta_{h_{cu}}$. A repeat of the sketch of the rms value of the magnetic-field-intensity function across the winding-layer height is shown at the origin of the waveform plots. Note that the peak values of the cosinusoidally varying time wave is $\sqrt{2}$ times the rms values of the waveforms.

As explained in Section 1.2, we write the phasor boundary conditions in magnitude and phase notation as

$$\underline{H}_z(0) = H_z(0)\angle\theta_0 \tag{4.15}$$

$$\underline{H}_z(h_{cu}) = H_z(h_{cu})\angle\theta_{h_{cu}} \tag{4.16}$$

The angles θ_0 and $\theta_{h_{cu}}$ must be expressed in relation to some reference angle. We find that it is convenient for most purposes in this report to choose $\theta_{h_{cu}} = 0$ as the reference phase angle. The boundary conditions can be expressed as time functions by choosing a cosinusoidal reference and writing,

$$H_z(0,t) = \sqrt{2}\,H_z(0)\cos(\omega t + \theta_0) \tag{4.17}$$

$$H_z(h_{cu},t) = \sqrt{2}\,H_z(h_{cu})\cos(\omega t + \theta_{h_{cu}}) \tag{4.18}$$

Since these boundary conditions are varying in time, the instantaneous magnetic-field-intensity profile across the current sheet is continually changing. It is important to point out, however, that it is the rms value or magnitude of the current-density phasor whose effect over the height of the current sheet determines the power loss in the windings. This presumably is the reason why the field and current-density distributions in a layer are commonly represented by plots of the phasor *magnitude* (rms value) of the magnetic field intensity $|\underline{H}_z(x)|$ and the current density $|\underline{J}_z(x)|$ at each point in the current sheet [10]. In one reference [10], the magnitude plots are accompanied by plots of the real and imaginary parts as well.

4.1.4 Differential Relationships between $\underline{H}_z(x)$ and $\underline{J}_y(x)$ in the Current Sheet

With the above conceptual picture of the magnetic-field distribution across a winding layer in mind, we return our attention to deriving an analytical expression for the magnetic-field-intensity and current-density distributions. We start this development by writing two of the field equations given in Appendix A in a form that is appropriate for the infinite-current-sheet problem considered here. In doing so, we obtain two equations that interrelate the magnetic field intensity and current density so that we can easily determine the expression for one given an expression for the other. In the next section, we first calculate an expression for the magnetic-field-intensity distribution, and then apply one of the relationships derived in this section to determine the corresponding expression for the current-density distribution.

If we write the Maxwell field expression for Faraday's law from (A.1) as $\nabla\times\mathbf{E} = -\frac{\partial \mathbf{B}}{\partial t}$ in terms of $\mathbf{J}$ and $\mathbf{H}$ by using the relations $\mathbf{B} = \mu_o\mathbf{H}$ and $\mathbf{J} = \sigma\mathbf{E}$, we get

$$\nabla \times \mathbf{J}(x,y,z,t) \quad = \quad -\mu_o\sigma\frac{\partial}{\partial t}\mathbf{H}(x,y,z,t) \tag{4.19}$$

Since we are interested only in the special case of sinusoidal steady-state excitation at an angular frequency ω, we can remove the explicit time dependence from (4.19) by replacing $\mathbf{J}$ and $\mathbf{H}$ with their corresponding phasors. As shown in Appendix A, taking the time derivative of a real quantity is equivalent to multiplying its corresponding phasor by $j\omega$. Therefore, we can rewrite (4.19) in phasor form as

$$\nabla \times \underline{\mathbf{J}}(x,y,z) \quad = \quad -j\omega\mu_o\sigma\underline{\mathbf{H}}(x,y,z) \tag{4.20}$$

which relates the current-density phasor at any point in space to the magnetic-field-intensity phasor at that same point. Finally, using the definition of complex wave number $\underline{k}$ for a good conductor from (4.3) we have

$$\nabla \times \underline{\mathbf{J}}(x,y,z) \quad = \quad -\underline{k}^2\underline{\mathbf{H}}(x,y,z) \tag{4.21}$$

Similarly, we can write the Maxwell-field expression for Ampere's law given by (A.2) as $\nabla \times \mathbf{H} = \mathbf{J} + \frac{\partial \mathbf{D}}{\partial t}$ in the form

$$\nabla \times \mathbf{H} = \sigma\mathbf{E} + \epsilon_o\frac{\partial \mathbf{E}}{\partial t} \tag{4.22}$$

where the constitutive relations $\mathbf{J} = \sigma\mathbf{E}$ and $\mathbf{D} = \epsilon\mathbf{E}$ have been used. In the sinusoidal steady-state case, we have

$$\nabla \times \underline{\mathbf{H}}(x,y,z) = \sigma\underline{\mathbf{E}}(x,y,z) + j\omega\epsilon_o\underline{\mathbf{E}}(x,y,z) \tag{4.23}$$

Now, if

$$\omega\mu_o\sigma \gg \omega^2\mu_o\epsilon_o \tag{4.24}$$

as is assumed in deriving the complex wave number $\underline{k}$ for the good conductor in (4.3), then

$$\sigma \gg \omega\epsilon_o \tag{4.25}$$

and we can approximate (4.23) by

$$\begin{aligned} \nabla \times \underline{\mathbf{H}}(x,y,z) &\approx \sigma\underline{\mathbf{E}}(x,y,z) \\ &\approx \underline{\mathbf{J}}(x,y,z) \end{aligned} \tag{4.26}$$

We show in Appendix C that for the one dimensional sinusoidal analysis where the spatial components of $\underline{\mathbf{J}}$ and $\underline{\mathbf{H}}$ are functions only of x, (4.21) and (4.26) reduce to the one-dimensional equations,

$$\boxed{\begin{aligned} \frac{\partial \underline{J}_y(x)}{\partial x}\hat{\mathbf{a}}_{\mathbf{z}} &= -\underline{k}^2 \underline{H}_z(x)\hat{\mathbf{a}}_{\mathbf{z}} && (4.27) \\ \frac{\partial \underline{H}_z(x)}{\partial x}\hat{\mathbf{a}}_{\mathbf{y}} &= -\underline{J}_y(x)\hat{\mathbf{a}}_{\mathbf{y}} && (4.28) \end{aligned}}$$

These two results are the one-dimensional field relations that we find useful in solving the diffusion-equation boundary-value problem for the infinite current sheet. Also, (4.27) and (4.28) point out that the current density and the magnetic field intensity are directly related and that we can always express one function in terms of the other. We make use of this fact in the following section where, after solving equation (4.13) for $\underline{H}_z(x)$, we obtain the equation for $\underline{J}_y(x)$ directly by applying the differential relationship (4.28).

4.2 SOLUTION TO FIELD EQUATIONS FOR $\underline{H}_z(x)$ AND $\underline{J}_y(x)$ FOR AN INFINITE CURRENT SHEET

Equation (4.13) is the one-dimensional diffusion equation written in terms of magnetic field intensity. The general solution of an equation of this form is

$$\underline{H}_z(x) = \underline{H}_1\, e^{\underline{k}x} + \underline{H}_2\, e^{-\underline{k}x} \tag{4.29}$$

where $\underline{H}_1$ and $\underline{H}_2$ are arbitrary quantities yet to be determined; $\underline{H}_1$ and $\underline{H}_2$ are written as underlined symbols to indicate that these quantities are in fact complex numbers representing phasor quantities. We use the boundary values of the magnetic field intensity, $\underline{H}_z(0)$ and $\underline{H}_z(h_{cu})$, to solve this differential equation as follows:

1. Use the boundary values to write two independent expressions involving $\underline{H}_1$ and $\underline{H}_2$. Evaluating (4.29) at $x = 0$ gives

$$\underline{H}_z(0) = \underline{H}_1 + \underline{H}_2 \tag{4.30}$$

and at $x = h_{cu}$ gives

$$\underline{H}_z(h_{cu}) = \underline{H}_1\, e^{\underline{k}h_{cu}} + \underline{H}_2\, e^{-\underline{k}h_{cu}} \tag{4.31}$$

2. Solve simultaneously for $\underline{H}_1$ and $\underline{H}_2$. Using (4.30) to substitute for $\underline{H}_2$ in (4.31) gives

$$\underline{H}_z(h_{cu}) = \underline{H}_1 e^{\underline{k}h_{cu}} + \left[\underline{H}_z(0) - \underline{H}_1\right] e^{-\underline{k}h_{cu}}$$

or,

$$\underline{H}_1 = \frac{\underline{H}_z(h_{cu}) - \underline{H}_z(0)e^{-\underline{k}h_{cu}}}{e^{\underline{k}h_{cu}} - e^{-\underline{k}h_{cu}}} \tag{4.32}$$

and a second use of (4.30) gives

$$\underline{H}_2 = \frac{\underline{H}_z(0)e^{\underline{k}h_{cu}} - \underline{H}_z(h_{cu})}{e^{\underline{k}h_{cu}} - e^{-\underline{k}h_{cu}}} \tag{4.33}$$

3. Substitute (4.32) and (4.33) back into the general solution (4.29) to give

$$\begin{aligned}\underline{H}_z(x) &= \frac{1}{e^{\underline{k}h_{cu}} - e^{-\underline{k}h_{cu}}}\Big[\underline{H}_z(h_{cu})e^{\underline{k}x} - \underline{H}_z(0)e^{\underline{k}(x-h_{cu})} \\ &\qquad + \underline{H}_z(0)e^{-\underline{k}(x-h_{cu})} - \underline{H}_z(h_{cu})e^{-\underline{k}x}\Big] \\ &= \frac{1}{e^{\underline{k}h_{cu}} - e^{-\underline{k}h_{cu}}}\Big[\underline{H}_z(h_{cu})\left(e^{\underline{k}x} - e^{-\underline{k}x}\right) \\ &\qquad - \underline{H}_z(0)\left(e^{\underline{k}(x-h_{cu})} - e^{-\underline{k}(x-h_{cu})}\right)\Big]\end{aligned} \tag{4.34}$$

4. Use the identity

$$\sinh\theta = \frac{e^{\theta} - e^{-\theta}}{2} \tag{4.35}$$

to rewrite equation (4.34) as

$$\boxed{\underline{H}_z(x) = \frac{1}{\sinh \underline{k}h_{cu}}\left[\underline{H}_z(h_{cu})\sinh \underline{k}x + \underline{H}_z(0)\sinh \underline{k}(h_{cu} - x)\right]} \tag{4.36}$$

5. Calculate $\underline{J}_y(x)$ by applying the differential relationship (4.28) to our solution for $\underline{H}_z(x)$ in (4.36). We can rewrite equation(4.28) as

$$\underline{J}_y(x) = -\frac{\partial \underline{H}_z(x)}{\partial x} \tag{4.37}$$

and then apply this result by differentiating (4.36) with respect to x to yield

$$\frac{\partial \underline{H}_z(x)}{\partial x} = \frac{\underline{k}}{\sinh \underline{k}h_{cu}}\left[\underline{H}_z(h_{cu})\cosh \underline{k}x - \underline{H}_z(0)\cosh \underline{k}(h_{cu} - x)\right] \tag{4.38}$$

so that

$$\boxed{\underline{J}_y(x) = \frac{-\underline{k}}{\sinh \underline{k}h_{cu}}\left[\underline{H}_z(h_{cu})\cosh \underline{k}x - \underline{H}_z(0)\cosh \underline{k}(h_{cu} - x)\right]} \tag{4.39}$$

The above equation (4.39) for current density $\underline{J}_y(x)$ and equation (4.36) for magnetic field intensity $\underline{H}_z(x)$ are the solutions we are seeking. Based only on the values of $\underline{H}_z(0)$ and $\underline{H}_z(h_{cu})$, the thickness of the winding layer h_{cu}, and the angular frequency ω of the sinusoidal excitation, we can now calculate the value of the current density and the magnetic field intensity at any point within a winding layer. In addition, equations (4.36) and (4.39) highlight the fact that the distributions of the magnetic field intensity and the current density across the current sheet actually result from the superposition of two independent effects. That is, the two boundary magnetic fields $\underline{H}_z(0)$ and $\underline{H}_z(h_{cu})$ have mathematically equivalent effects on the distributions of $\underline{H}_z(x)$ and $\underline{J}_y(x)$, except, of course, that the magnetic field $\underline{H}_z(0)$ dominates the total magnetic field in the region near the surface at $x = 0$ while the magnetic field $\underline{H}_z(h_{cu})$ dominates the total magnetic field in the region near the surface at $x = h_{cu}$. This characteristic of the solutions is discussed in greater detail in Section 4.3.2 as we explore more thoroughly the meaning of equations (4.36) and (4.39).

Before beginning such a detailed investigation, however, we first introduce some new notation that proves useful later in our analysis of energy storage and power loss. For convenience, we define a new variable χ such that

$$\chi = \begin{cases} x & \text{if } |\underline{H}_z(x = h_{cu})| \geq |\underline{H}_z(x = 0)| \\ h_{cu} - x & \text{if } |\underline{H}_z(x = h_{cu})| < |\underline{H}_z(x = 0)| \end{cases} \tag{4.40}$$

which means that we always have $\chi = h_{cu}$ at the surface which has the *larger* of the two boundary magnetic fields, and $\chi = 0$ at the surface which has the *smaller* of the two boundary magnetic fields. In other words, regardless of the relative magnitudes of the boundary magnetic fields, we have now defined χ such that

$$|\underline{H}_z(\chi = h_{cu})| \geq |\underline{H}_z(\chi = 0)| \tag{4.41}$$

If we rewrite our solution for magnetic field intensity (4.36) in terms of χ, we obtain

$$\underline{H}_z(\chi) = \frac{1}{\sinh \underline{k}h_{cu}}\left[\underline{H}_z(\chi = h_{cu})\sinh \underline{k}\chi + \underline{H}_z(\chi = 0)\sinh \underline{k}(h_{cu} - \chi)\right] \tag{4.42}$$

and factoring out the term $\underline{H}_z(\chi = h_{cu})$ gives

$$\underline{H}_z(\chi) = \frac{\underline{H}_z(\chi = h_{cu})}{\sinh \underline{k}h_{cu}}\left[\sinh \underline{k}\chi + \frac{\underline{H}_z(\chi = 0)}{\underline{H}_z(\chi = h_{cu})}\sinh \underline{k}(h_{cu} - \chi)\right] \tag{4.43}$$

The form of equation (4.43) can be simplified somewhat by introducing the boundary-condition ratio $\underline{\Gamma} = \alpha + j\beta$ as

$$\underline{\Gamma} \;=\; \frac{\underline{H}_z(\chi = 0)}{\underline{H}_z(\chi = h_{cu})} \tag{4.44}$$

where

$$\alpha \;=\; \mathrm{Re}(\underline{\Gamma}) \tag{4.45}$$

$$\beta \;=\; \mathrm{Im}(\underline{\Gamma}) \tag{4.46}$$

and because of the way in which we define χ, we know that

$$0 \;\leq\; |\underline{\Gamma}| \;\leq\; 1 \tag{4.47}$$

for all possible choices of boundary magnetic fields, except of course for the trivial case where $|\underline{H}_z(0)|$ and $|\underline{H}_z(h_{cu})|$ are both equal to zero. In Section 4.1.3 above, we write $\underline{H}_z(0)$ and $\underline{H}_z(h_{cu})$ in magnitude and phase notation. We can use these expressions here to write

$$\begin{aligned}
\alpha &= \mathrm{Re}(\underline{\Gamma}) = \mathrm{Re}\left[\frac{\underline{H}_z(\chi = 0)}{\underline{H}_z(\chi = h_{cu})}\right] \\
&= \mathrm{Re}\left[\frac{H_z(\chi = 0)\angle\theta_{\chi = 0}}{H_z(\chi = h_{cu})\angle\theta_{\chi = h_{cu}}}\right] \\
&= \frac{H_z(\chi = 0)}{H_z(\chi = h_{cu})}\cos(\theta_{\chi = 0} - \theta_{\chi = h_{cu}})
\end{aligned} \tag{4.48}$$

$$\begin{aligned}
\beta &= \mathrm{Im}(\underline{\Gamma}) = \mathrm{Im}\left[\frac{\underline{H}_z(\chi = 0)}{\underline{H}_z(\chi = h_{cu})}\right] \\
&= \mathrm{Im}\left[\frac{H_z(\chi = 0)\angle\theta_{\chi = 0}}{H_z(\chi = h_{cu})\angle\theta_{\chi = h_{cu}}}\right] \\
&= \frac{H_z(\chi = 0)}{H_z(\chi = h_{cu})}\sin(\theta_{\chi = 0} - \theta_{\chi = h_{cu}})
\end{aligned} \tag{4.49}$$

where $\theta_{\chi = 0}$ and $\theta_{\chi = h_{cu}}$ are understood to be the arguments of the magnetic field intensity phasor at $\chi = 0$ and $\chi = h_{cu}$, respectively. Finally, we may rewrite (4.43) to obtain an expression for the magnetic field intensity phasor in terms of the real component α and the imaginary component β of $\underline{\Gamma}$.

$$\boxed{\underline{H}_z(\chi) = \frac{\underline{H}_z(\chi = h_{cu})}{\sinh \underline{k} h_{cu}}\left[\sinh \underline{k}\chi + (\alpha + j\beta)\sinh \underline{k}(h_{cu} - \chi)\right]} \tag{4.50}$$

The corresponding equation for current density is

$$\boxed{\underline{J}_y(\mathcal{X}) = \frac{(-1)^{\varepsilon}\,\underline{k}\,\underline{H}_z(\mathcal{X} = h_{cu})}{\sinh \underline{k}h_{cu}}\Big[\cosh \underline{k}\mathcal{X} - (\alpha + j\beta)\cosh \underline{k}(h_{cu} - \mathcal{X})\Big]} \tag{4.51}$$

where

$$\varepsilon = \begin{cases} 1 & \text{if } |\underline{H}_z(x = h_{cu})| \geq |\underline{H}_z(x = 0)| \\ 0 & \text{if } |\underline{H}_z(x = h_{cu})| < |\underline{H}_z(x = 0)| \end{cases} \tag{4.52}$$

so that the sign of equation (4.51) changes depending upon which case in equation (4.52) applies.

Equation (4.51) is the phasor expression for the current density function in the infinite current sheet subject to the given boundary conditions, and is equivalent to the result given by Perry [13] in his equation (8b). In Chapter 7, Part II of this report, the equivalence of these two equations is shown. Furthermore, except for minor differences in symbols, equation (4.51) is identical to equation (A-15) in the appendix of the paper by Vandelac and Ziogas [19].

Equations (4.50) and (4.51) are key equations. They are important in their own right because they give the phasor expressions for the sinusoidal steady-state magnetic field intensity and the current-density distributions at an arbitrary height $\mathcal{X}$ in a current sheet of height h_{cu} when a sinusoidal magnetic field of $\underline{H}_z(\mathcal{X} = 0)$ is present on one side and a field of $\underline{H}_z(\mathcal{X} = h_{cu})$ is on the other. They are also important because they lead, as shown in Section 4.5, to the calculation of energy storage and power loss within the winding structure of multi-winding transformers, which in turn can lead to the determination of the parameter values for an equivalent circuit, which is our ultimate goal.

4.3 GRAPHICAL ILLUSTRATIONS OF $\underline{H}_z(x)$ AND $\underline{J}_y(x)$ IN AN INFINITE CURRENT SHEET

Before continuing with the application of equations (4.50) and (4.51) to the winding space of a transformer, we first explore more thoroughly the meaning of the solutions for $\underline{H}_z(x)$ and $\underline{J}_y(x)$ through an extensive array of illustrations. In this section, we define specific numerical examples involving both single-layer and four-layer structures and, using the equations developed in the above sections, we provide a large number of plots and data tables that illuminate many of the important aspects of the magnetic-field-intensity and current-density distributions. Although the forms of equations (4.50) and (4.51) are well-defined and appropriate for their application in Section 4.5, we find that equations (4.36) and (4.39) are, in their simplicity, better-suited for the purposes of this Section. As shown in the development of Section 4.2, equations (4.50) and (4.51) really contain the same information as (4.36) and (4.39), although (4.50) and (4.51) have a slightly more generalized form.

4.3.1 Plots of Phasor Magnitudes for a Single-Layer Example

Plots of the magnitudes of the phasors of equations (4.36) and (4.39) reveal the impact that excitation frequency has on the current-density and magnetic-field-intensity distributions in a current sheet. Figure 4.2 shows the dramatic changes in magnitude of the phasor magnetic-field-intensity distribution over the height of a winding layer that take place as the excitation frequency increases. This plot represents the distribution of the magnitude $|\underline{H}_z(x)|$ of the magnetic-field-intensity phasor across a single layer given a particular set of boundary conditions. Figure 4.3 shows the corresponding variation of the magnitude of the current-density phasor in the same layer.

For this example, the magnetic-field-intensity boundary conditions are chosen as $\underline{H}_z(0) = 1\angle 0°$ and $\underline{H}_z(h_{cu}) = 2\angle 0°$. The plots in Figs. 4.2 and 4.3 represent the variation of $|\underline{H}_z(x)|$ and $|\underline{J}_y(x)|$ in an arbitrarily chosen winding layer of height $h_{cu} = 7.0 \times 10^{-4}$ meters over a frequency range of one kilohertz to one megahertz. At 1 kHz, the magnitude of the magnetic field intensity varies approximately linearly from one layer surface to the other, and the magnitude of the current density is approximately constant at a value of 1.43 kA/m^2 over the 0.7 mm height of the winding. At higher frequencies, the magnitude of the magnetic field intensity decreases substantially away from the layer boundaries, but remains constant over frequency at the two surfaces of the layer—as it must since the boundary conditions of the problem are the same for all these four frequencies. Also, the magnitude of the current density increases near the surfaces of the winding layer and drops to approximately zero in the interior regions. At 1 MHz, the magnitude of the current density at the surface where the magnetic-field-intensity magnitude is 1 A-t/m rises to 20.5 kA/m^2, and it reaches 41.0 kA/m^2 at the surface where the magnetic-field-intensity is 2 A-t/m in magnitude.

4.3.2 Plots of Phasors for a Single-Layer Example

In Section 4.3.1, we show the result of an example involving a single layer for which we plot the magnitudes of the magnetic-field-intensity and current-density phasors found in equations (4.36) and (4.39). These plots are shown in Figs. 4.2 and 4.3 for a range of excitation frequencies. In interpreting these two figures, however, we must be careful to remember that they are only *magnitude* plots, and therefore do not contain any information on the phase angles that are associated with $\underline{H}_z(x)$ and $\underline{J}_y(x)$. One way to incorporate this information is to accompany each of the magnitude plots with a corresponding phase plot, or similarly, with plots of the corresponding real and imaginary parts of the phasors. Magnitude plots such as those in Figs. 4.2 and 4.3, together with plots of the corresponding real and imaginary parts of the phasors are found in [9]. Although this approach does illustrate all of the information contained in the phasors of equations (4.36) and (4.39), it is generally quite difficult to gain physical insight into these solutions when the magnitude and phase information appears in two or more separate plots. To remedy this, we might wish to show the phasors of equations (4.36) and (4.39) at equally spaced intervals across the layer. Such a representation, however,

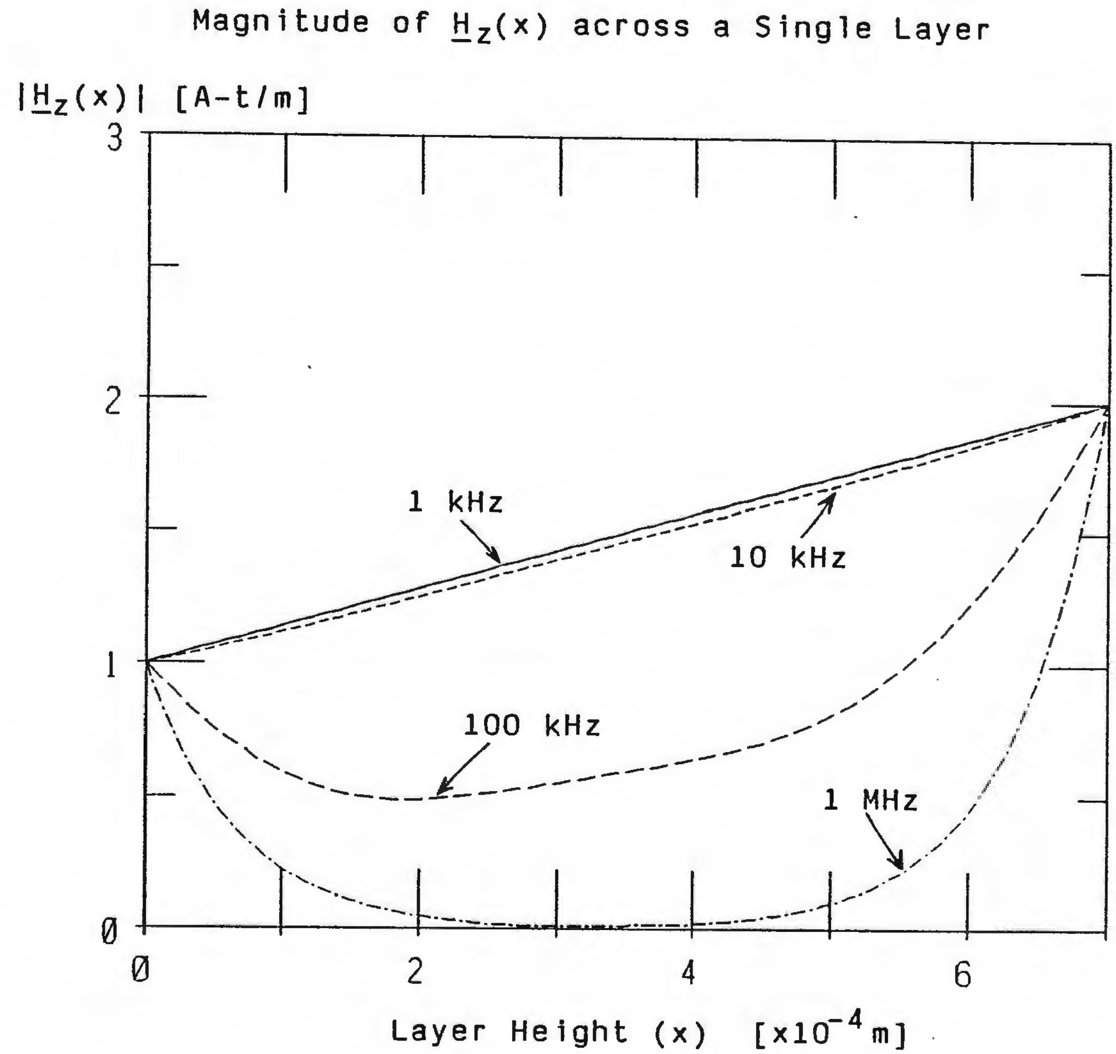

Figure 4.2: Plot of the magnitude of the magnetic-field-intensity phasor $\underline{H}_z(x)$ in an infinite current sheet at 1 kHz, 10 kHz, 100 kHz, and 1 MHz.

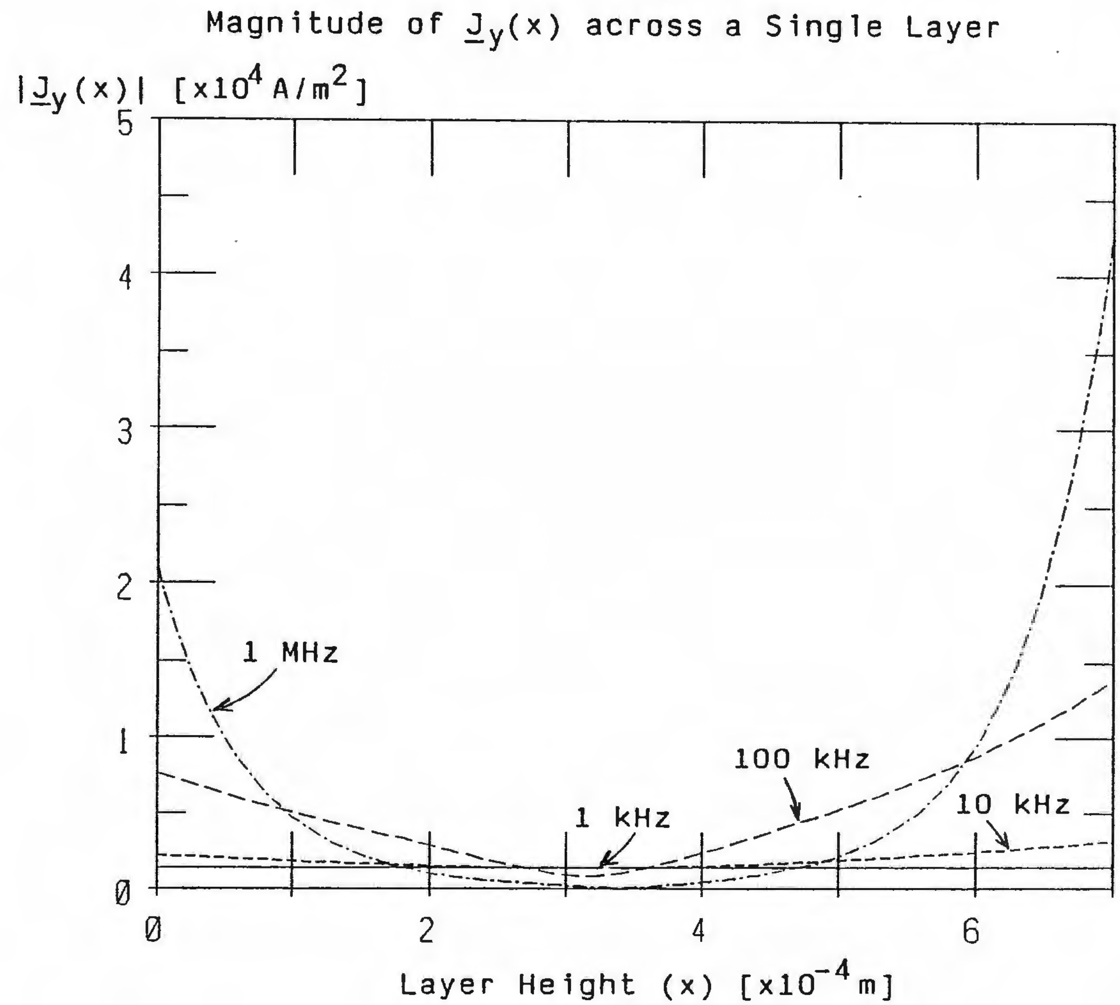

Figure 4.3: Plot of the magnitude of the current-density phasor $\underline{J}_y(x)$ in an infinite current sheet at excitation frequencies of 1 kHz, 10 kHz, 100 kHz, and 1 MHz.

needs to be three-dimensional, since each phasor has two components (real and imaginary) and the location of each phasor across the layer height requires a third dimension. Although a geometrical model is the most appropriate solution, we can also represent this information in an isometric plot.

As an introduction to the concept of plotting phasors in three dimensions, we first look at a simple example. The upper left corner of Fig. 4.4 shows for reference a right-hand three-dimensional coordinate system. The axes of this coordinate system are labeled x, Re, and Im, where x stands for distance, Re for Real, and Im for Imaginary. Note that this coordinate system is different from the one introduced in Fig. 3.15 of Section 3.3.1 in that the Re-axis and Im-axis of Figure 4.4 define, respectively, the real and imaginary parts of some phasor quantity, whereas the y-axis and z-axis of Fig. 3.15 define, respectively, the geometrical dimensions of layer depth and layer breadth. However, the x-axis of Fig. 4.4 *does* correspond to the x-axis of Figure 3.15 in that they both define the geometrical dimension of layer height. On the larger set of axes in Fig. 4.4, a hypothetical phasor distribution of current density $\underline{J}_y(x)$ is plotted at four equally spaced points across a winding layer. The real part of $\underline{J}_y(x)$ is plotted on the horizontal Re-axis, the imaginary part is plotted on the vertical Im-axis, and the distance through the layer is plotted on the horizontal x-axis that is coming out of the page to the left. Note that the positive half of each axis is drawn with a solid line, while the negative half is drawn with a dashed line. The current density phasors are drawn parallel to the plane of Re versus Im at evenly spaced points across the layer (x-axis). Each phasor has its tail on the x-axis, and its head at a point corresponding to the real and imaginary parts. The arrow head usually drawn at the head of a phasor is omitted in this report to avoid unnecessary cluttering of subsequent drawings. A phasor with zero phase angle (no imaginary part) would be shown parallel to the Re-axis, and a phasor with a 90° phase angle would be shown parallel to the Im-axis. The dotted lines that form parallelograms around each phasor in Fig. 4.4 are drawn so that the relative contributions of the real and imaginary parts can be seen more easily. Note that the table beneath the plot in Fig. 4.4 shows the value of the current-density phasor, magnitude and phase angle, together with the real and imaginary components, at each of the four points across the layer height.

We can obtain additional insight into how the current density varies with time over the height of the current sheet if we imagine all of the phasors to be rotating at an angular frequency $2\pi f$ in a counterclockwise direction around the x-axis, so that the actual time-varying distribution of the current density is proportional[2] to the projections of the phasors onto the plane of x versus Re. Illustrations of the results of such a process are shown later in this section.

In Section 4.3.1 we plot the magnitudes of the phasors $\underline{H}_z(x)$ and $\underline{J}_y(x)$ for a particular numerical example in Figs 4.2 and 4.3. We now return to this same numerical example, but instead of plotting the magnitudes of the phasors, we now plot the phasors

[2] We have defined the magnitude of the phasor as the rms value of the actual sinusoid. Therefore, the actual sinusoidal waveform can be recovered from the rotating phasor by multiplying the real projection of the phasor by $\sqrt{2}$.

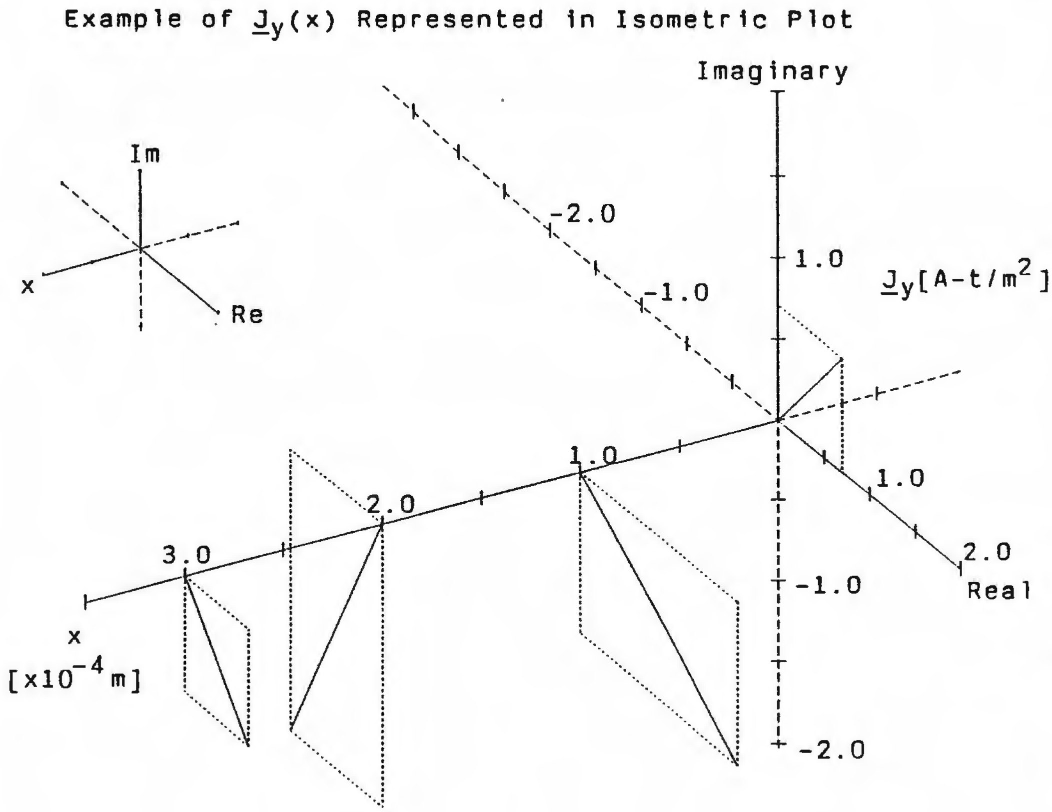

x $\times 10^{-4}$m	$\lvert\underline{J}_y(x)\rvert$ A/m^2	$/\underline{J}_y(x)$ Degrees	Re[$\underline{J}_y(x)$] A/m^2	Im[$\underline{J}_y(x)$] A/m^2
0	1.0	45°	0.707	0.707
1	2.0	−30°	1.732	−1.000
2	2.0	−120°	−1.000	−1.732
3	1.0	−45°	0.707	−0.707

Figure 4.4: Plot of hypothetical current-density phasor $\underline{J}_y(x)$ at four points across the winding layer.

themselves. Figure 4.5 consists of plots of these $\underline{H}_z(x)$ and $\underline{J}_y(x)$ phasors as a function of layer height x at 1 kHz. The magnetic-field-intensity phasors at the boundaries are again given as $\underline{H}_z(0) = 1\angle 0°$ and $\underline{H}_z(h_{cu}) = 2\angle 0°$, and the height of the copper current sheet is given as $h_{cu} = 7.0 \times 10^{-4}$ m. Our arbitrary choice of zero phase angle for the phasors $\underline{H}_z(0)$ and of $\underline{H}_z(h_{cu})$ simply means that the magnetic field at $x = 0$ is oscillating in phase with the field at $x = h_{cu}$. In addition to the plots of the magnetic-field-intensity and current-density phasors, Fig. 4.5 also contains a data table that provides the values for the $\underline{H}_z(x)$ and $\underline{J}_y(x)$ phasors at eight equally spaced points across the layer height.

The upper set of three-dimensional axes in Fig. 4.5 shows the variation of the magnetic-field-intensity phasors across the height of the layer calculated using equation (4.36). Note that the heads of the phasors are all connected with a single, solid line to enhance the appearance of a surface. The plot and associated tabular values of $\underline{H}_z(x)$ in Fig. 4.5 reveals that the magnitude of the magnetic field at 1 kHz varies linearly within two significant figures across the layer. Also, since none of the phasors differ by more than 2° from being parallel to the real axis, we know that the magnetic field at every point across the layer must be oscillating very nearly in phase with the magnetic field at the surfaces. This simple linear distribution of magnetic field intensity is similar to the result obtained in Section 3.1.2.1 for the case of a uniform dc current except, of course, that the distribution obtained from the phasors in Fig. 4.5 is varying sinusoidally with time.

The current-density phasors associated with these magnetic-field-intensity phasors have been calculated using equation (4.39) and the results are plotted on the lower set of axes in Fig. 4.5. Note that on this plot the scaling on the real and imaginary axes has been changed from the upper plot to accommodate the current-density phasors, while the scaling on the x-axis is the same as that on the upper set of axes. The plot of the current-density phasors and the table of values in Fig. 4.5 reveal that the magnitude of $\underline{J}_y(x)$ remains essentially constant across the layer while the phase angle varies by less than $\pm 10°$. Therefore, we conclude that the actual current density is almost uniform across the layer and varies sinusoidally with time. Once again, this result agrees rather closely with the dc field calculation of Section 3.1.2.1 which shows that a uniform current is associated with a linearly distributed magnetic field intensity.

We mention above that the actual distributions of the magnetic field intensity and current density are proportional to the real projections of the phasor distributions in Fig. 4.5. We can, therefore, see how these distributions vary with time by imagining that all of the phasors are rotating in a counterclockwise direction about the x-axis with an angular frequency ω. This principle can be illustrated by looking at a time sequence of such real projections. Figure 4.6, which is a companion piece to Fig. 4.5, shows the actual distribution of current density across the winding layer for an excitation frequency of 1 kHz at various points in time throughout one cycle. Each small plot is labeled with an angle measure, corresponding to the angular measure of time ωt. The plots divide a single period of oscillation into twelve equal intervals, and they are ordered in time from top to bottom down the left column, and then down the right. From Figure 4.6,

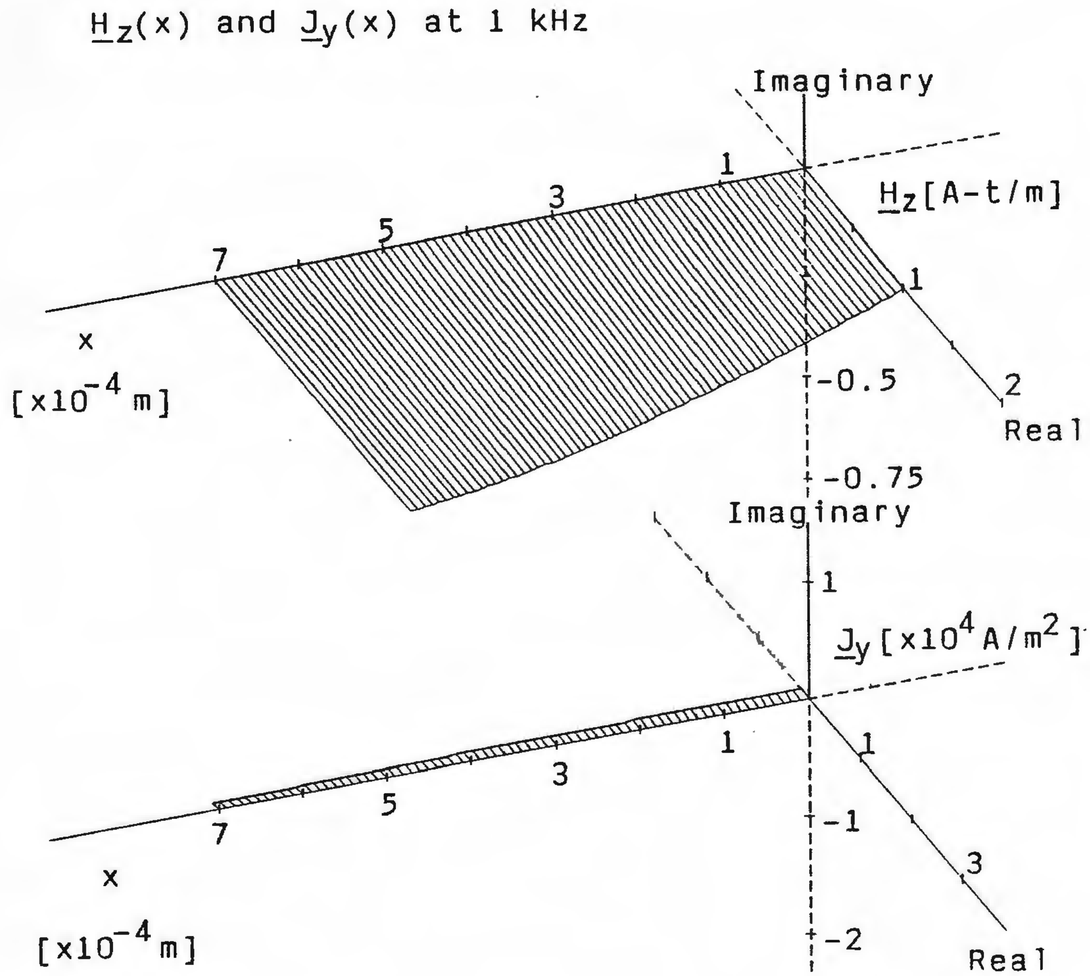

x $\times 10^{-4}$m	$\underline{H}_z(x)$ A-t/m	$\underline{J}_y(x)$ $\times 10^4$A/m^2	x $\times 10^{-4}$m	$\underline{H}_z(x)$ A-t/m	$\underline{J}_y(x)$ $\times 10^4$A/m^2
0	$1.00\angle 0.00°$	$0.144\angle 172.18°$	4	$1.57\angle -1.40°$	$0.143\angle 180.80°$
1	$1.14\angle -0.87°$	$0.143\angle 173.96°$	5	$1.71\angle -1.10°$	$0.143\angle 183.55°$
2	$1.29\angle -1.34°$	$0.143\angle 175.99°$	6	$1.86\angle -0.63°$	$0.144\angle 186.53°$
3	$1.43\angle -1.49°$	$0.143\angle 178.28°$	7	$2.00\angle 0.00°$	$0.145\angle 189.70°$

Figure 4.5: Plots of the magnetic-field-intensity phasor $\underline{H}_z(x)$ and the current-density phasor $\underline{J}_y(x)$ at an excitation frequency of 1 kHz.

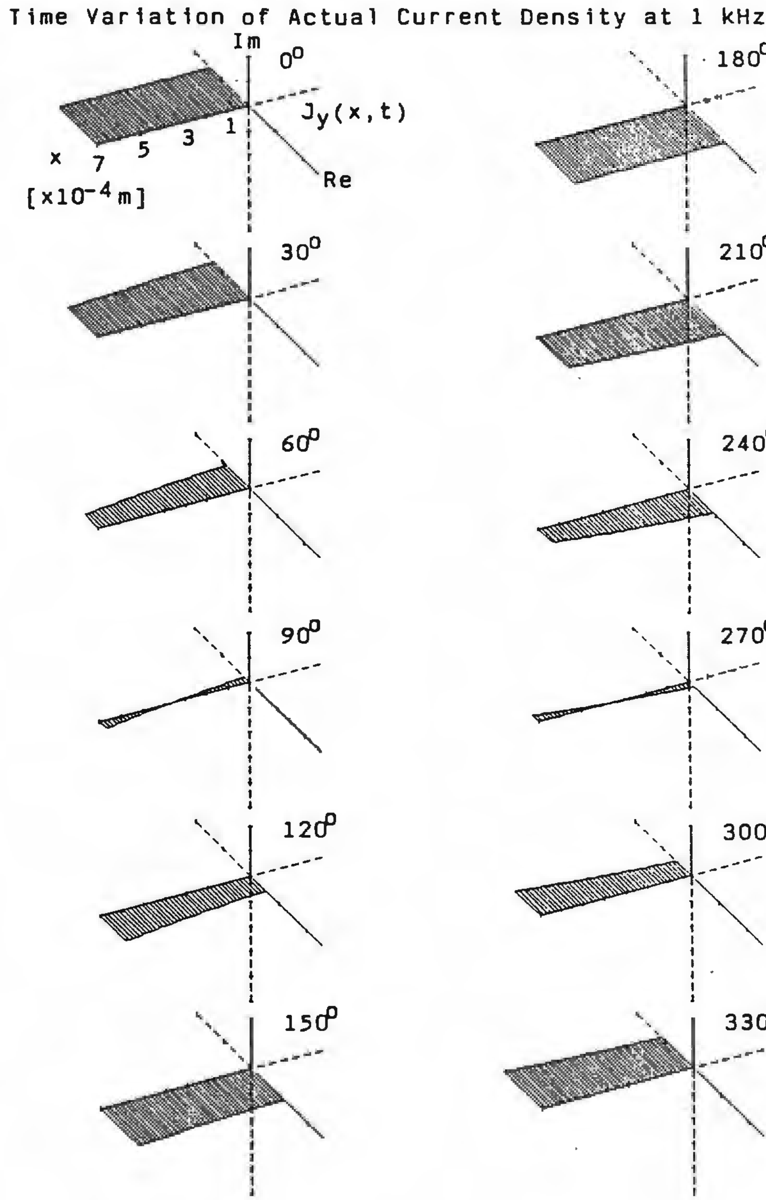

Figure 4.6: Plots of the actual current-density distribution at twelve different instants of ωt spaced evenly throughout a single cycle of oscillation at 1 kHz. The progression advances from top to bottom down the left column and then down the right.

we can see that the current density is nearly uniform across the layer at every point in time throughout a single cycle. Since we take the real, or cosinusoidal part of the phasor $\underline{J}_y(x)$ to be proportional to the actual, time-varying current density, we would expect that for a perfectly uniformly distributed current density there would be zero current at all points across the winding layer at times corresponding to $\omega t = 90°$ and $\omega t = 270°$. Accordingly, Fig. 4.6 reveals that there is very little current density in the winding layer at these times. Note that the small amount of current density that is evident at the time corresponding to $\omega t = 90°$ is a result of the difference in phase between the current density at $x = 0$ and at $x = h_{cu}$. From the table of Fig. 4.5, we can see that the actual current density at $x = 0$ is lagging in phase 17.52° behind the current density at $x = h_{cu}$. Nevertheless, the current density that does appear at the time corresponding to $\omega t = 90°$ in Fig. 4.6 is, at all points across the height of the layer, less than one-sixth of the current density that appears at the time corresponding to $\omega t = 0°$. In general, the distribution of current density at this frequency differs from a perfectly uniform distribution by no more than 6% at all points across the height of the layer. Consequently, we can conclude from Figs. 4.5 and 4.6 that skin effect does not have a significant influence on the distributions of magnetic field intensity and current density when the excitation frequency is low or, more specifically, when the skin depth is large with respect to the layer height.

Figure 4.7 contains plots of $\underline{H}_z(x)$ and $\underline{J}_y(x)$ for an excitation frequency of 10 kHz and Fig. 4.8 shows the corresponding time variation of the actual current density. The boundary conditions and layer height are the same as those used in Fig. 4.5. Throughout this section, we continue to use the example that is introduced in Section 4.3.1 and only the frequency is varied. The plot of the magnetic-field-intensity phasors and the table of values in Fig. 4.7 show that the magnitudes of the phasors no longer vary linearly across the layer, and that the phasors near the center of the layer are lagging by almost 15° behind those which have been established at the surfaces. Likewise, the current-density phasors plotted on the lower set of axes in Fig. 4.7 are also beginning to show the influence of skin effect. There is now a noticeable increase in the magnitude of the current-density phasors near the surfaces of the layer, by about 50% over that at 1 kHz at $x = 0$ and by about 100% at $x = h_{cu}$, while the magnitude near the center has decreased slightly below that at 1 kHz. More importantly, this plot reveals that there is now a substantial phase difference of 113° between the current-density phasors at $x = 0$ and at $x = h_{cu}$. It appears as though the small ribbon of current density that is seen in the lower set of axes in Fig. 4.5 has been twisted and widened at the ends to give us the distribution of Fig. 4.7. As a result of this phase difference, there is now an appreciable portion of a cycle during which the actual current flows in an opposite direction on one side of the current sheet than it does on the other. This can be seen more clearly in Fig. 4.8, which shows the actual current-density distribution at twelve instants of time during a single cycle of oscillation, at an excitation frequency of 10 kHz. This figure reveals, for example, that during the interval $60° \leq \omega t \leq 150°$ the current near the surface at $x = 0$ is flowing in the $-y$-direction, while the current near the surface at $x = h_{cu}$ is flowing in the $+y$-direction.

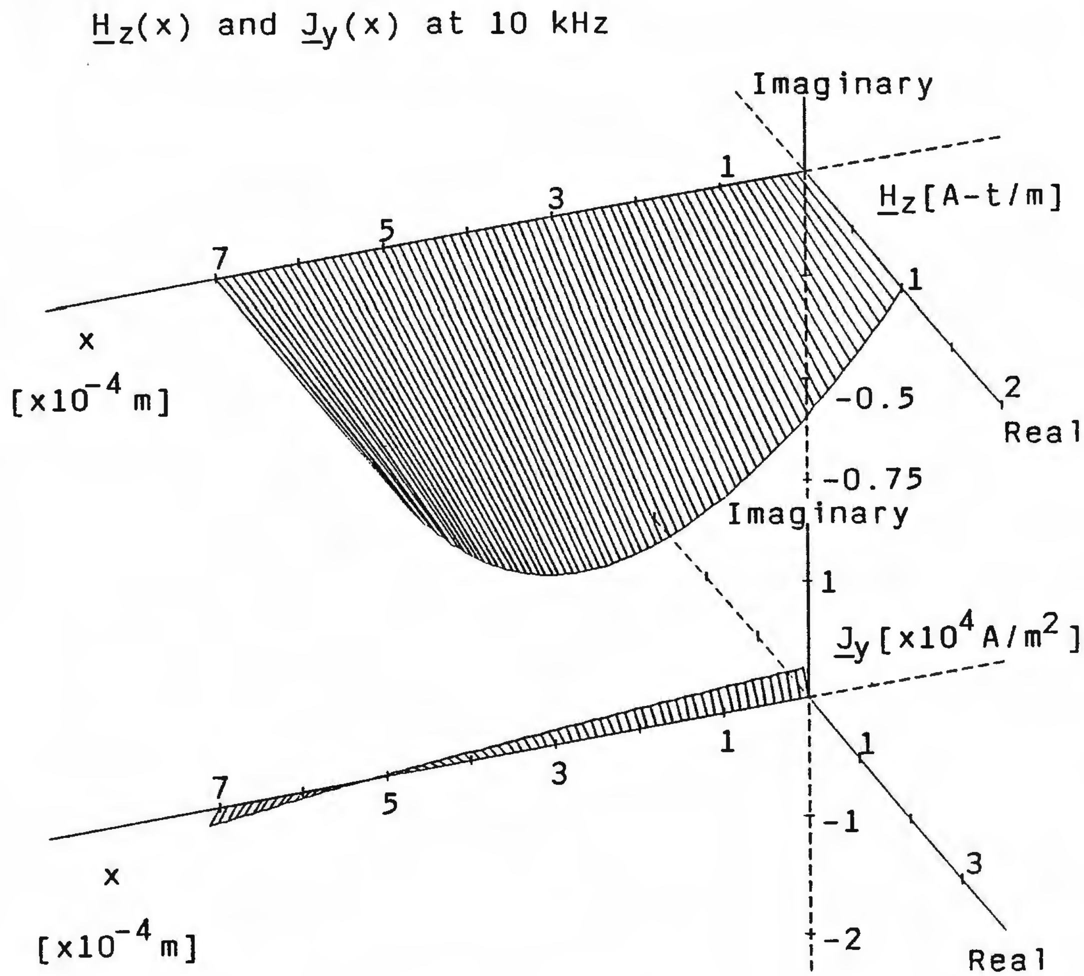

x $\times 10^{-4}$m	$\underline{H}_z(x)$ A-t/m	$\underline{J}_y(x)$ $\times 10^4$A/m^2	x $\times 10^{-4}$m	$\underline{H}_z(x)$ A-t/m	$\underline{J}_y(x)$ $\times 10^4$A/m^2
0	$1.00\angle 0.00°$	$0.217\angle 119.70°$	4	$1.54\angle -13.82°$	$0.151\angle 186.99°$
1	$1.12\angle -8.55°$	$0.182\angle 127.62°$	5	$1.68\angle -10.86°$	$0.185\angle 207.14°$
2	$1.26\angle -13.19°$	$0.154\angle 141.74°$	6	$1.83\angle -6.16°$	$0.236\angle 221.84°$
3	$1.40\angle -14.74°$	$0.141\angle 162.94°$	7	$2.00\angle 0.00°$	$0.298\angle 232.84°$

Figure 4.7: Plots of the magnetic-field-intensity phasor $\underline{H}_z(x)$ and the current-density phasor $\underline{J}_y(x)$ at an excitation frequency of 10 kHz.

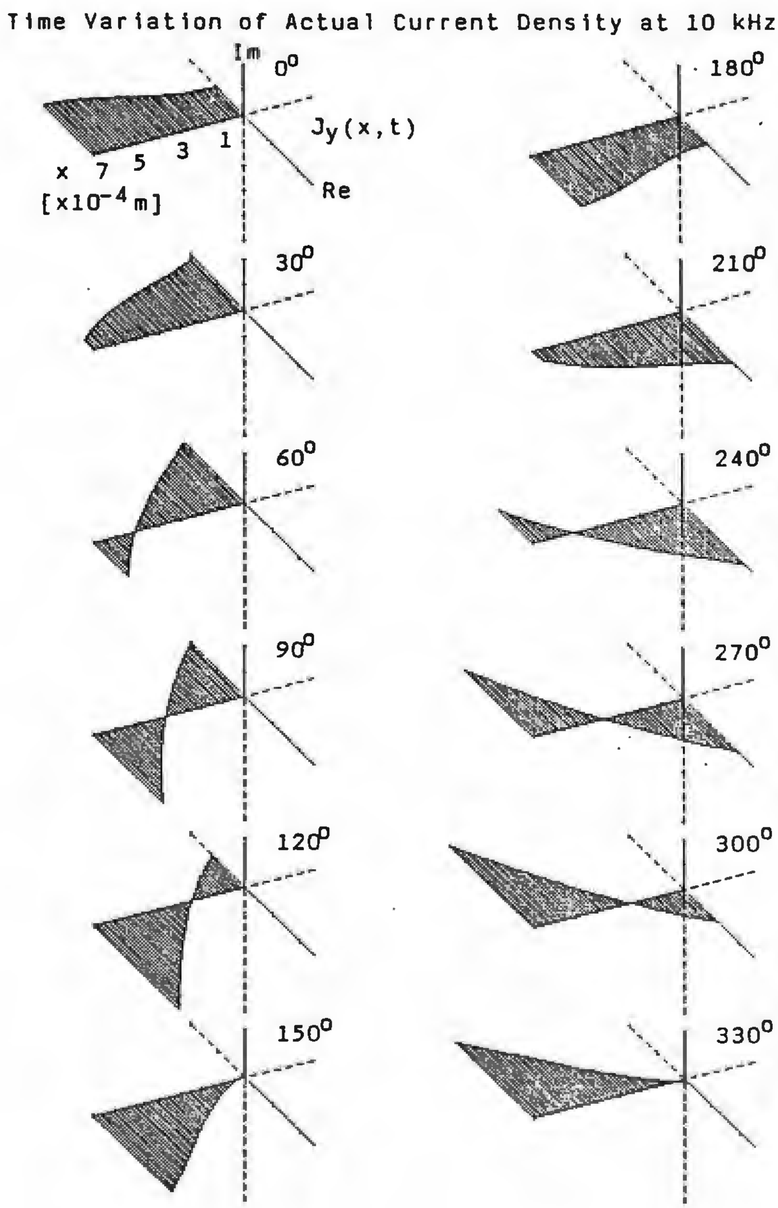

Figure 4.8: Plots of the actual current-density distribution at twelve different instants of ωt spaced evenly throughout a single cycle of oscillation at 10 kHz. The progression advances from top to bottom down the left column and then down the right.

The $\underline{H}_z(x)$ and $\underline{J}_y(x)$ phasors for the case of 100-kHz excitation frequency are plotted in Fig. 4.9, and the corresponding variation of actual current density is plotted in Figure 4.10. The variation of the magnetic-field-intensity phasors on the upper set of axes in Fig. 4.9 reveals the substantial impact of skin effect on this example layer at this frequency. The phasors near the center of the layer are now lagging in phase by more than 90° with respect to the phasors at the surfaces. There is also an attenuation in the magnitude of the $\underline{H}_z(x)$ phasors away from the surfaces of about 40% with respect to the two lower frequency cases. This is due to the magnetic field's diminishing ability to penetrate the conducting layer at higher frequencies. From the development of Appendix D, we know that this attenuation in the magnetic field is a result of energy being transferred (via the electric field) into the medium in the form of increased current density. Accordingly, we see that the current density phasors of Fig. 4.9 are, in fact, substantially larger in magnitude near the surfaces of the layer, more than 5 times that for 1 kHz at $x = 0$ and more than 9 times at $x = h_{cu}$. Moreover, since the phase angles of the current-density phasors at $x = 0$ and at $x = h_{cu}$ differ by 180°, Fig. 4.9 suggests that at every instant of time throughout a cycle the actual current will be flowing in opposite directions at $x = 0$ and at $x = h_{cu}$. This fact is evident from Fig. 4.10, which shows the time variation of the actual current density distribution at 100 kHz. Note that the current-density distribution at each point in time is approximately odd-symmetric about the center of the layer, and is slightly uneven only because the magnitude of the magnetic field intensity is greater at $x = h_{cu}$ than it is at $x = 0$. Thus, there is an imbalance of current in the $+y$- and $-y$-directions at each point in time which results in a net instantaneous current flow in either the $+y$- or the $-y$-direction. An interesting effect is seen in Fig. 4.10 at times corresponding to $\omega t = 60°$ and $\omega t = 240°$. At 60°, the current at $x = 0$ is flowing in the $-y$-direction; in the neighborhood of $x = 1 \times 10^{-4}$, the current is flowing in the $+y$-direction; then, for x between 2.6×10^{-4} and 6.3×10^{-4}, the current has reversed again and is flowing in the $-y$-direction; finally, from $x = 6.4 \times 10^{-4}$ to $x = h_{cu}$ the current is again flowing in the $+y$-direction. In other words, at this instant in time, the current undergoes three reversals in direction across the layer height from $x = 0$ to $x = h_{cu}$. At $\omega t = 240°$, we see a similar pattern since the distribution of the actual current density is a mirror image of that for $\omega t = 60°$ about the x vs Im-plane.

At this point we should emphasize that the increase in surface current densities that appears in Figs. 4.7 and 4.9 in no way suggests that there is a "larger current" in the winding layer than is present in the lowest frequency case of Fig 4.5. We can see this by taking the actual current density at any instant of time in either Fig. 4.8 or Fig. 4.10 and spatially averaging it across the winding layer to obtain the *net*, instantaneous current density. In each case, the net or average current density that we obtain is exactly the same as the almost uniform current density of Fig. 4.6 for the same instant in time. This is expected since we force the same net sinusoidal current into the layer at all of these four frequencies.

In Section 4.2, immediately following the derivation of equations (4.36) and (4.39), we make the claim that the distribution of the magnetic field intensity and current

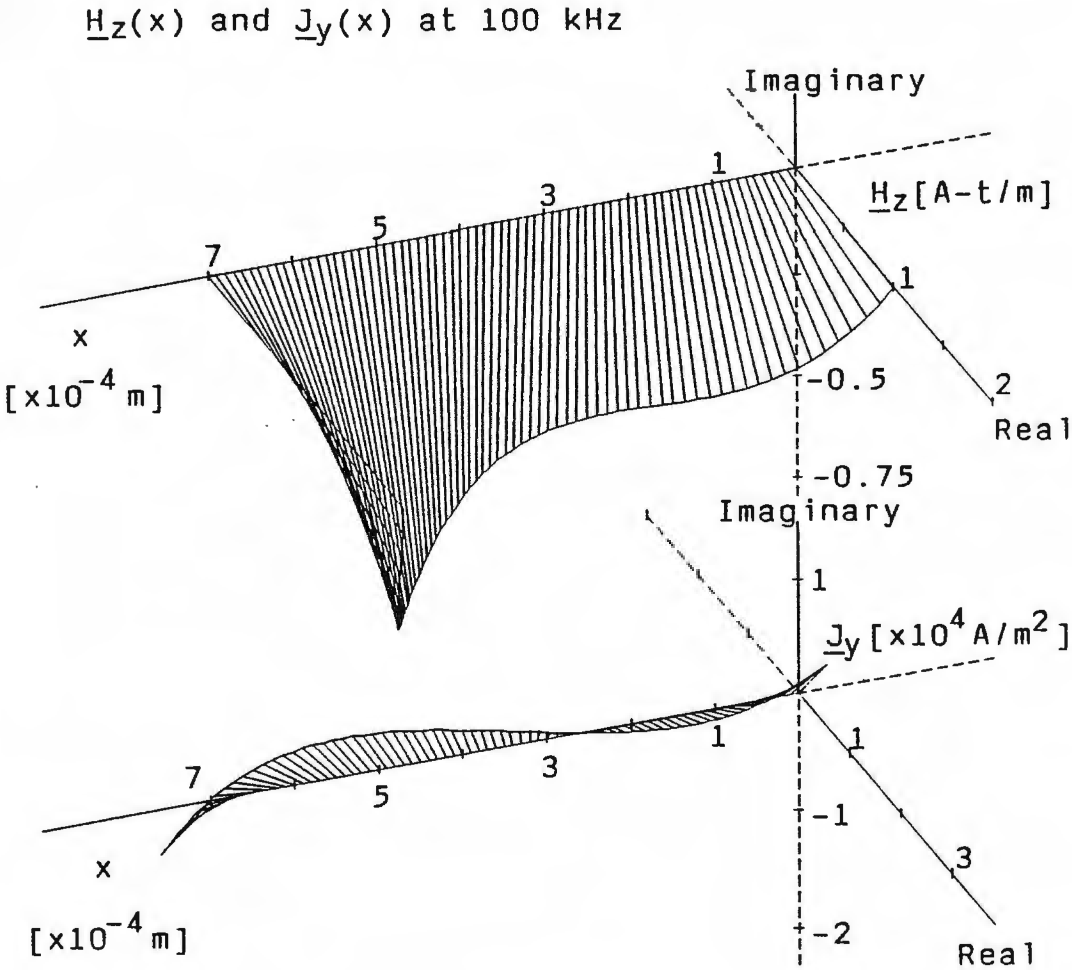

x $\times 10^{-4}$m	$\underline{H}_z(x)$ A-t/m	$\underline{J}_y(x)$ $\times 10^4$A/m^2	x $\times 10^{-4}$m	$\underline{H}_z(x)$ A-t/m	$\underline{J}_y(x)$ $\times 10^4$A/m^2
0	$1.00\angle 0.00°$	$0.755\angle 44.46°$	4	$0.68\angle -85.37°$	$0.240\angle 158.21°$
1	$0.61\angle -35.90°$	$0.503\angle 25.76°$	5	$0.85\angle -59.89°$	$0.521\angle 180.11°$
2	$0.52\angle -75.93°$	$0.286\angle 19.57°$	6	$1.25\angle -28.72°$	$0.868\angle 200.89°$
3	$0.59\angle -93.22°$	$0.094\angle 63.88°$	7	$2.00\angle 0.00°$	$1.352\angle 224.83°$

Figure 4.9: Plots of the magnetic-field-intensity phasor $\underline{H}_z(x)$ and the current-density phasor $\underline{J}_y(x)$ at an excitation frequency of 100 kHz.

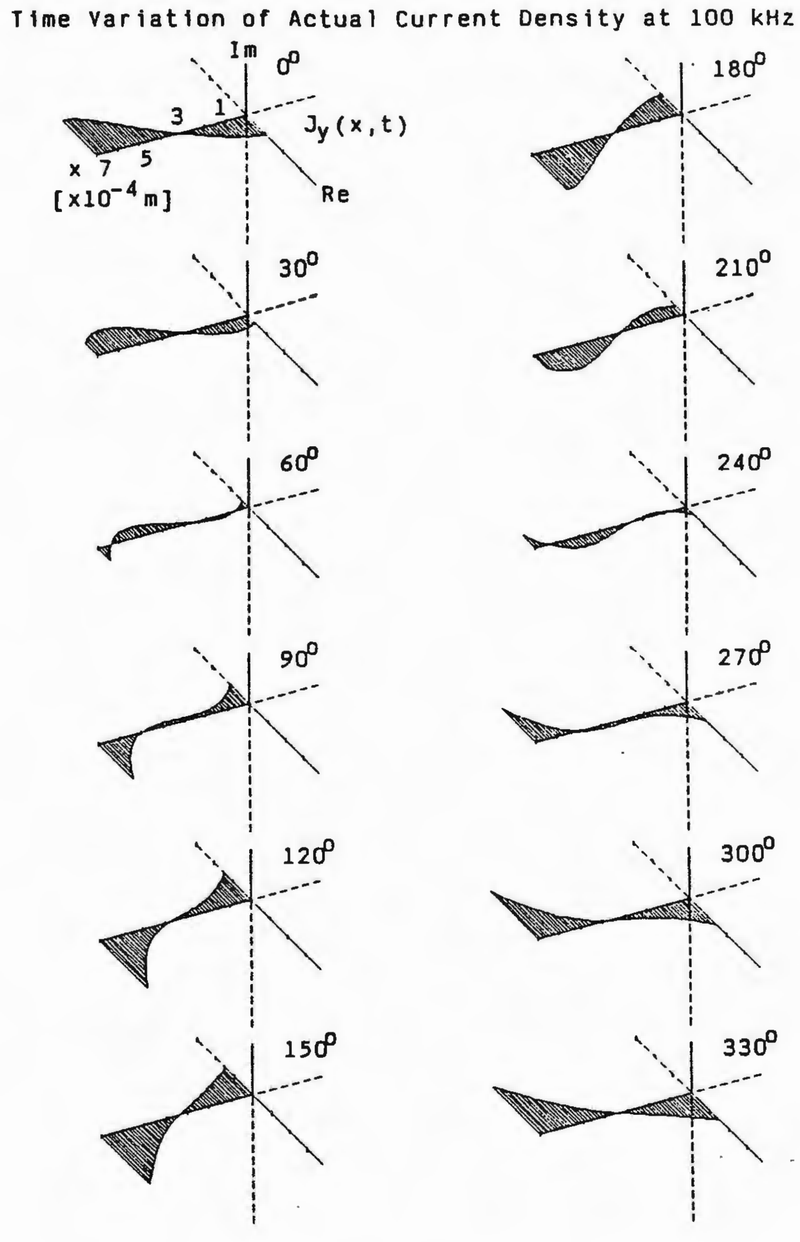

Figure 4.10: Plots of the actual current-density distribution at twelve different instants of ωt spaced evenly throughout a single cycle of oscillation at 100 kHz. The progression advances from top to bottom down the left column and then down the right.

density can be thought of as resulting from the superposition of the two independently established boundary magnetic fields—$\underline{H}_z(0)$ and $\underline{H}_z(h_{cu})$. We can graphically illustrate this fact for the case of equation (4.36) by replotting the $\underline{H}_z(x)$ distribution of Fig. 4.9 with the individual contributions of each boundary magnetic field explicitly shown. This is done in Fig. 4.11, which shows the two independent sets of magnetic-field-intensity phasors, as well as the envelope of the sum, which corresponds to the envelope seen in Fig. 4.9. The first distribution of phasors is marked by a dashed-line envelope, and it has the boundary conditions $\underline{H}_z(0) = 1\angle 0°$ and $\underline{H}_z(h_{cu}) = 0\angle 0°$. The second distribution of phasors has a solid line envelope and has the boundary conditions $\underline{H}_z(0) = 0\angle 0°$ and $\underline{H}_z(h_{cu}) = 2\angle 0°$. The envelope of the sum of these two phasor distributions at every point across the layer is represented by the dotted line. Note that near the surfaces of the layer the sum of the distributions more closely follows the distribution that has a non-zero boundary condition at that surface. Thus, there is a tendency for each of the two magnetic fields to exert a dominant influence in the interior of the layer near the surface at which it has a non-zero boundary value.

Alternatively, we can consider the distribution of the magnetic field intensity and current density to be a physical superposition of two transverse electromagnetic waves, as discussed in Appendix D. By this approach, we are able to explain in detail the distributions as they vary with frequency.

Figure 4.12 shows the distribution of $\underline{H}_z(x)$ and $\underline{J}_y(x)$ at a 1-MHz excitation frequency, and Fig. 4.13 shows the corresponding time variation of the actual current-density distribution at this frequency. On the upper set of axes in Fig. 4.12, we see that the magnitude $|\underline{H}_z(x)|$ of the magnetic field intensity drops off rapidly away from the surfaces of the layer, and the phase angle of $\underline{H}_z(x)$ near the center of the layer is now lagging as much as 270° behind the phase angle of $\underline{H}_z(x)$ at the surfaces. Once again, this sharp attenuation of the magnetic field intensity is associated with an increase in surface current density. The plot of $\underline{J}_y(x)$ in Fig. 4.12 shows that the magnitude of the current-density phasors has now dramatically increased near the surfaces by more than 14 times the 1 kHz value at $x = 0$ and more than 28 times at $x = h_{cu}$. Near the center of the layer, the magnitude of the current-density phasors has attenuated substantially to only 20% of the 1 kHz value. Note that the current-density phasors between $x = 0$ and $x \approx 2 \times 10^{-4}$ are all leading their corresponding magnetic-field-intensity phasors over this same region by a phase angle of approximately 45°. Likewise, the current-density phasors between $x \approx 5 \times 10^{-4}$ and $x = h_{cu}$ are leading their corresponding magnetic-field-intensity phasors by approximately 225°. Also, the phase angle of $\underline{H}_z(x)$ over these same regions exhibits even symmetry about the center of the layer, so that for $0 \leq x \leq 2 \times 10^{-4}$ we have

$$\angle\underline{H}_z(x) \approx \angle\underline{H}_z(h_{cu} - x) \tag{4.53}$$

where $\angle\underline{H}_z(x)$ denotes the phase angle of the phasor quantity $\underline{H}_z(x)$. As a result of this symmetry and the phase relationship between $\underline{J}_y(x)$ and $\underline{H}_z(x)$, the current density

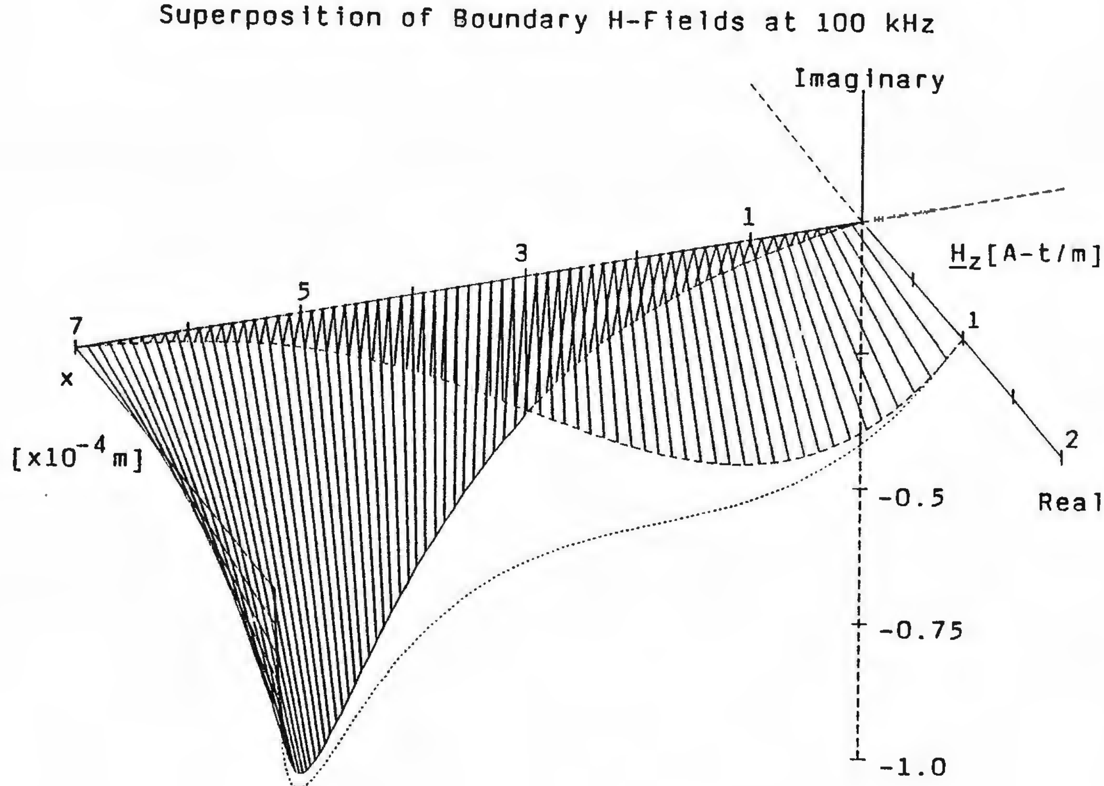

Figure 4.11: Superposition of two magnetic-field-intensity phasor distributions at 100 kHz showing the individual contributions from the magnetic fields established at each of the surfaces.

$\underline{J}_y(x)$ for $0 \leq x \leq 2 \times 10^{-4}$ must also obey

$$\angle \underline{J}_y(x) \approx \angle \underline{J}_y(h_{cu} - x) - 180^\circ \tag{4.54}$$

This means that the current-density phasors at a given distance from one surface of the layer are approximately 180° out of phase with the current-density phasors at the same distance from the other surface. Therefore, at every time instant throughout a single cycle, there must be actual currents that flow in opposite directions near the two surfaces of the layer. Figure 4.13 reveals this 180° phase difference in the current density near the two surfaces of the winding layer. Note that the actual current-density distribution at each point in time is nearly odd symmetric about the center of the layer and the imbalance in the symmetry corresponds to the net instantaneous current flowing in the layer. At frequencies and layer heights where the skin depth is even smaller with respect to h_{cu} than it is in Figs. 4.12 and 4.13, the relationship given by (4.54) holds over an increasingly large interval, and in the limit is true for $0 \leq x \leq h_{cu}/2$.

It is also interesting to observe in Fig. 4.13 that at any instant in time, as we move across the winding layer from $x = 0$ to $x = h_{cu}$, we see that the current flow undergoes several changes in direction. This dispels the notion that skin-effect currents are simply surface currents that travel in one direction on one side of the winding layer and in the opposite direction on the other side of the winding layer. For example, at time $\omega t = 60^\circ$ in Fig. 4.13, the current on the surface of the layer at $x = h_{cu}$ is flowing in the $+y$-direction, while the current just beneath this surface is flowing in the $-y$-direction and is comparable in magnitude to the current at the surface, so that the magnitude of the current density at $x = 6.27 \times 10^{-4}$ is 95% of that at $x = h_{cu}$. In fact, there are a total of five reversals of direction in the current density across the layer height from $x = 0$ to $x = h_{cu}$, although this is difficult to see given the scale used in Fig. 4.13.

From the development of Appendix D, we understand that the current density actually distributes itself according to the envelope of the electric-field component of two superposed electromagnetic waves. As each electromagnetic wave travels into the layer from one of the two surfaces, its electric field oscillates as a damped sinusoid, generating a current at each point that is proportional to the electric field at that same point. When the skin depth is small with respect to layer height ($\delta \approx 0.1 h_{cu}$ in Fig. 4.13), then there is very little interference between the two waves as they travel towards the center from opposite sides, and so the sinusoidal nature of the electric fields becomes apparent in the behavior of the current-density distribution. Therefore, it is this wavelike behavior which is responsible for the large number of direction changes in the actual current density at any instant in time.

Throughout this document, we have emphasized the fact that the importance of skin effect is in no way restricted to high-frequency applications. Indeed, skin effect can have a significant impact on the power-loss and energy-storage characteristics at what might be considered relatively low frequencies. Figure 4.14 dramatizes this fact. The example illustrated in this figure is in every way the same as the 1-kHz example of Figure 4.5 except one—that the copper height is now increased to $h_{cu} = 10 \times 10^{-3}$ m, or by a factor

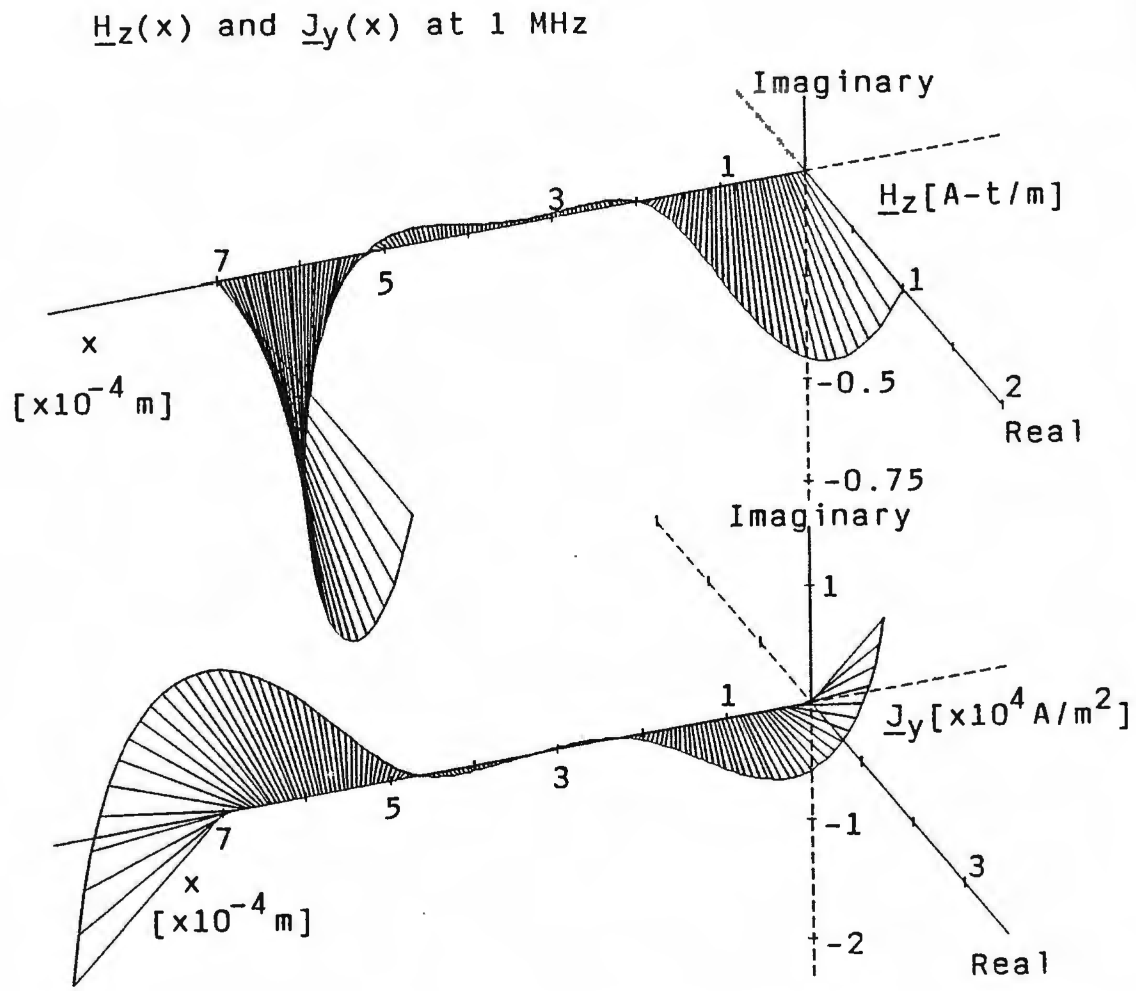

x $\times 10^{-4}$m	$\underline{H}_z(x)$ A-t/m	$\underline{J}_y(x)$ $\times 10^4$A/m^2	x $\times 10^{-4}$m	$\underline{H}_z(x)$ A-t/m	$\underline{J}_y(x)$ $\times 10^4$A/m^2
0	$1.00\angle 0.00°$	$2.049\angle 44.99°$	4	$0.03\angle -255.54°$	$0.053\angle -17.24°$
1	$0.24\angle -83.07°$	$0.481\angle -37.93°$	5	$0.11\angle -165.64°$	$0.227\angle 58.66°$
2	$0.05\angle -164.59°$	$0.114\angle -122.37°$	6	$0.47\angle -83.01°$	$0.962\angle 142.02°$
3	$0.01\angle -272.79°$	$0.028\angle -177.67°$	7	$2.00\angle 0.00°$	$4.097\angle 225.00°$

Figure 4.12: Plots of the magnetic field intensity phasor $\underline{H}_z(x)$ and the current density phasor $\underline{J}_y(x)$ at an excitation frequency of 1 MHz.

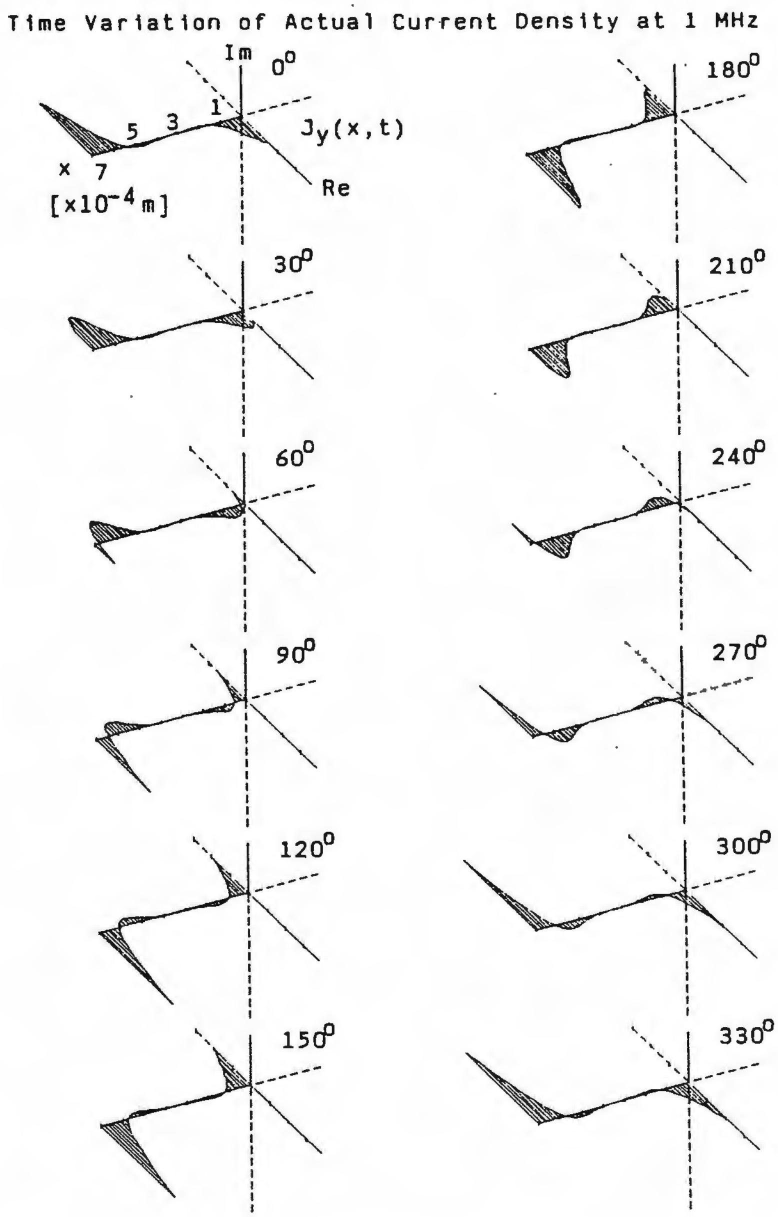

Figure 4.13: Plots of the actual current-density distribution at twelve different times (ωt) spaced evenly throughout a single cycle of oscillation at 1 MHz. The progression advances from top to bottom and then from left to right.

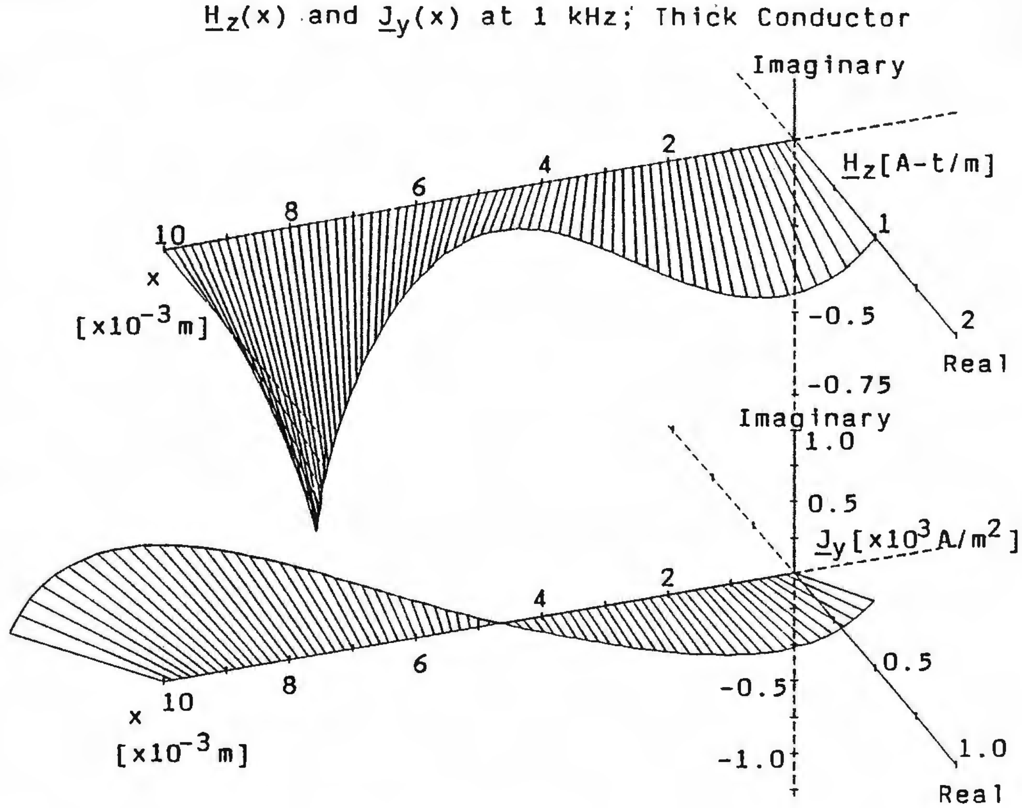

x $\times 10^{-4}$m	$\underline{H}_z(x)$ A-t/m	$\underline{J}_y(x)$ $\times 10^3$A/m^2	x $\times 10^{-4}$m	$\underline{H}_z(x)$ A-t/m	$\underline{J}_y(x)$ $\times 10^3$A/m^2
0	$1.00\angle 0.00°$	$0.652\angle 42.68°$	6	$0.36\angle -113.45°$	$0.186\angle 130.08°$
1	$0.61\angle -25.92°$	$0.429\angle 16.23°$	7	$0.50\angle -83.54°$	$0.336\angle 150.29°$
2	$0.35\angle -56.94°$	$0.291\angle -6.05°$	8	$0.78\angle -53.48°$	$0.534\angle 172.88°$
3	$0.25\angle -98.47°$	$0.184\angle -18.87°$	9	$1.25\angle -26.16°$	$0.829\angle 198.09°$
4	$0.26\angle -128.85°$	$0.084\angle -10.01°$	10	$2.00\angle 0.00°$	$1.297\angle 224.42°$
5	$0.30\angle -131.81°$	$0.065\angle 94.35°$			

Figure 4.14: Plots of the magnetic field intensity phasor $\underline{H}_z(x)$ and the current density phasor $\underline{J}_y(x)$ at an excitation frequency of 1 kHz where the thickness of the copper layer is increased to $h_{cu} = 10 \times 10^{-3}$ m.

of about 14. The scale on the plot of $\underline{J}_y(x)$ in Fig. 4.14 indicates that the current densities experienced in the thicker layer are generally smaller than those of Fig. 4.5. This is the case since the same magnetic-field boundary conditions are applied to both layers, so that the same net instantaneous current that flows in the thinner layer of Fig. 4.5 now flows through a larger volume in the layer of Fig. 4.14. Note that the magnitude of $\underline{H}_z(x)$ near the center of the layer in Fig. 4.14 is now decreased substantially to only 20% of the value at the center of the layer in Fig. 4.5. Likewise, the magnitude of $\underline{J}_y(x)$ in Fig. 4.14 is larger near the surfaces of the layer than it is at the center by 10 times at $x = 0$ and 20 times at $x = h_{cu}$. Also, since the change in the phase angle of $\underline{J}_y(x)$ is 182° from one surface to the other, we now expect that for almost all instants of time within a cycle, the current will flow in opposite directions near $x = 0$ and $x = h_{cu}$.

In comparing Figs. 4.5 and 4.14, one might be lead to wonder if there is some solid criteria by which to judge whether or not skin effect will be a significant factor at a particular excitation frequency, given that the geometry remains fixed. We can define such a *critical frequency* as one which results in a skin depth that exactly equals the height of the copper. Using the good-conductor definition of skin depth from (4.7)

$$\delta = \sqrt{\frac{2}{\omega\mu_0\sigma}} \tag{4.55}$$

we can write

$$h_{cu} = \delta = \sqrt{\frac{2}{\omega_c\mu_0\sigma}} \tag{4.56}$$

or

$$\omega_c = 2\pi f_c = \frac{2}{h_{cu}^2\,\mu_0\sigma} \tag{4.57}$$

where ω_c is the critical frequency. If we are well below this frequency, then the skin depth will be too large to affect significantly the field and current distributions. However, if we are near or above this critical frequency, then skin effect will generally be important. We can demonstrate this principle in relation to the above examples. For the example illustrated in Figs. 4.5 through 4.13, we have $h_{cu} = 7 \times 10^{-4}$, $\mu_0 = 4\pi \times 10^{-7}$, and $\sigma = 5.315 \times 10^7$ so that the critical frequency $\omega_c = 6.11 \times 10^4$ rad/s, or $f_c = 9.73$ kHz. Accordingly, we conclude from Figs. 4.5 through 4.13 that at 1 kHz there is very little effect on the field and current distributions, whereas for frequencies well above 10 kHz there is a significant effect. Similarly, for the thick layer example of Fig. 4.14, we find that $\omega_c = 299$ rad/s or $f_c = 47.7$ Hz and therefore expect that at 1 kHz there would indeed be a substantial impact of skin effect on the magnetic-field-intensity and current-density distributions.

We can further utilize the concept of critical frequency to examine the behavior of equations (4.36) and (4.39) in the limit of low frequency, where the excitation frequency is very much less than the critical frequency, or

$$\omega \ll \omega_c = \frac{2}{h_{cu}^2\,\mu_0\sigma} \tag{4.58}$$

Since (4.36) and (4.39) are in terms of complex wave number $\underline{k}$ instead of the frequency ω, we first rewrite the inequality of (4.58) in terms of the complex wave number. From (4.5) of Section 4.1.2 we can write

$$|\underline{k}| = \sqrt{\omega\mu_0\sigma} \tag{4.59}$$

and replacing the ω under the radical in (4.59) with the right-hand side of (4.58) we obtain

$$\begin{aligned} |\underline{k}| &\ll \frac{\sqrt{2}}{h_{cu}} && (4.60)\\ |\underline{k}|h_{cu} &\ll \sqrt{2} && (4.61) \end{aligned}$$

or, approximately

$$|\underline{k}|h_{cu} \ll 1 \tag{4.62}$$

Furthermore, since $0 \leq (h_{cu} - x) \leq h_{cu}$ and $0 \leq x \leq h_{cu}$, we also know that

$$|\underline{k}|(h_{cu} - x) \ll 1 \tag{4.63}$$

and

$$|\underline{k}|x \ll 1 \tag{4.64}$$

so that the inequalities of (4.62), (4.63) and (4.64) are all implied by (4.58). Expanding now the sinh terms in (4.36) yields

$$\begin{aligned} \underline{H}_z(x) &= \frac{1}{e^{\underline{k}h_{cu}} - e^{-\underline{k}h_{cu}}} \Big\{ \underline{H}_z(h_{cu}) \left[e^{\underline{k}x} - e^{-\underline{k}x} \right] \\ &\qquad + \underline{H}_z(0) \left[e^{\underline{k}(h_{cu} - x)} - e^{-\underline{k}(h_{cu} - x)} \right] \Big\} && (4.65) \end{aligned}$$

The Taylor series approximation for $e^{\underline{u}}$ is given by

$$e^{\underline{u}} \approx 1 + \underline{u} \qquad \text{for } |\underline{u}| \ll 1 \tag{4.66}$$

where $\underline{u}$ is any complex number. Using (4.62), (4.63) and (4.64) together with the approximation of (4.66), we can replace each of the exponentials in (4.65) with its corresponding linear term

$$\begin{aligned} \underline{H}_z(x) &= \frac{1}{1 + \underline{k}h_{cu} - 1 + \underline{k}h_{cu}} \Big\{ \underline{H}_z(h_{cu}) \Big[1 + \underline{k}x - 1 + \underline{k}x \Big] \\ &\qquad + \underline{H}_z(0) \Big[1 + \underline{k}h_{cu} - \underline{k}x - 1 + \underline{k}h_{cu} - \underline{k}x \Big] \Big\} \\ &= \frac{1}{2\underline{k}h_{cu}} \Big\{ \underline{H}_z(h_{cu}) \Big[2\underline{k}x \Big] + \underline{H}_z(0) \Big[2\underline{k}h_{cu} - 2\underline{k}x \Big] \Big\} \end{aligned}$$

After making cancellations and factoring, we obtain

$$\underline{H}_z(x) = \left[\frac{\underline{H}_z(h_{cu}) - \underline{H}_z(0)}{h_{cu}}\right] x + \underline{H}_z(0) \tag{4.67}$$

In a similar manner, we can apply the Taylor series approximation to the expression for the current-density phasor $\underline{J}_y(x)$ (4.39) and obtain

$$\underline{J}_y(x) = \underline{J}_y = \frac{\underline{H}_z(0) - \underline{H}_z(h_{cu})}{h_{cu}} \tag{4.68}$$

Equations (4.67) and (4.68) are the low-frequency forms for the magnetic-field-intensity and current-density distributions across the height of a layer. Naturally, the results obtained in (4.67) and (4.68) could have been obtained equally well by a direct application of Ampere's law assuming dc-excitation current. Note that the low-frequency form (4.67) of $\underline{H}_z(x)$ is the equation of a straight line corresponding to the linear distribution of $\underline{H}_z(x)$, while the low-frequency form (4.68) of $\underline{J}_y(x)$ is independent of x. This corresponds to the result obtained for the dc-case of Section 3.1.2 as well as the low-frequency-case of Fig. 4.5. Equation (4.68) is also useful in that it provides a value for the average current-density phasor $\underline{J}_y$ across the height of a layer, given the magnetic-field boundary conditions for that layer.

4.4 GRAPHICAL ILLUSTRATIONS OF $\underline{H}_z(x)$ AND $\underline{J}_y(x)$ IN AN IDEALIZED TRANSFORMER

4.4.1 Plots of Phasor Magnitudes Across Four Layers

The reader will recall that in Section 3.1.2 we introduce the concept of dc straight-line magnetic-field-intensity diagrams that are used to determine the values of magnetic field that exist at the boundaries of each winding layer in a two-layer infinite solenoid. In Section 4.1, we demonstrate that these boundary values are sufficient information to solve for both the current density and the magnetic-field intensity in the interior of an infinite current sheet. We now take the results of our infinite-current-sheet analysis and apply them to a four-layer infinite solenoid similar to the two-layer one developed in Section 3.1.2.

Figure 4.15 shows a four-layer solenoid in which the inner three layers are part of one winding and the outermost layer is a different winding. Each winding layer in the structure has a height h_{cu} of 7.0×10^{-4} m, the same as that of the single layer of Figs. 4.2 and 4.3. Each layer is separated by an air gap of 2×10^{-4} m, and the magnetic field boundary conditions for the four layers are given by $\underline{H}_z(0) = 0\angle 0°$, $\underline{H}_z(7 \times 10^{-4}) = \underline{H}_z(9 \times 10^{-4}) = 1\angle 0°$, $\underline{H}_z(16 \times 10^{-4}) = \underline{H}_z(18 \times 10^{-4}) = 2\angle 0°$, $\underline{H}_z(25 \times 10^{-4}) = \underline{H}_z(27 \times 10^{-4}) = 3\angle 0°$, and $\underline{H}_z(34 \times 10^{-4}) = 0\angle 0°$. Following the pattern used in Figs. 4.2 and 4.3, Figs. 4.16 and 4.17 show plots of the magnitude of

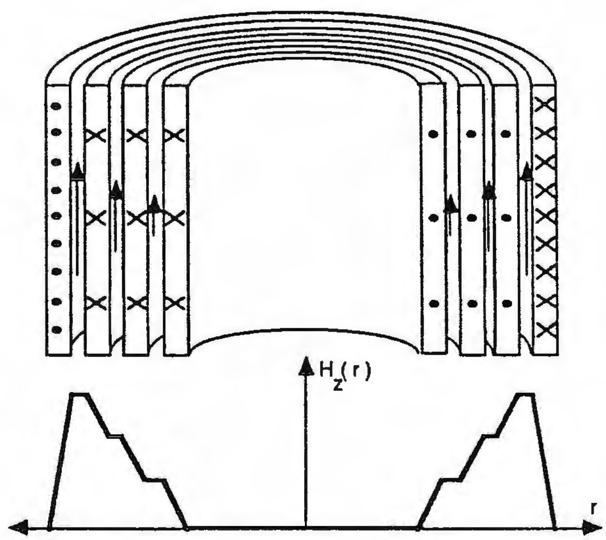

Figure 4.15: Structure of a four-layer solenoid. The three inner layers are all of one winding and the outer layer is of a different winding. The outer winding carries a current equal to the sum of the currents in the other layers.

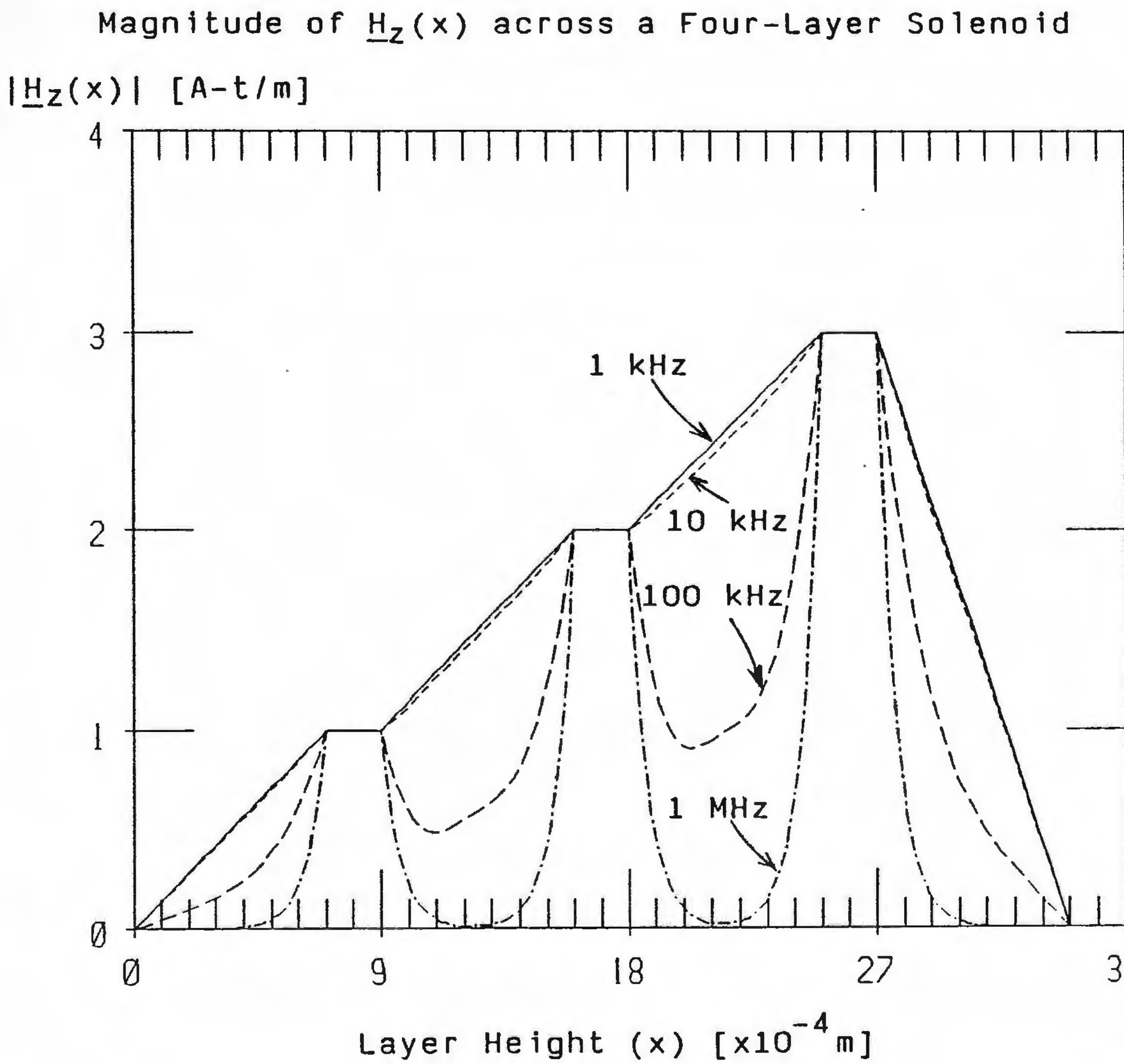

Figure 4.16: The magnitude of the magnetic-field-intensity phasor distribution for the solenoid shown in Fig. 4.15.

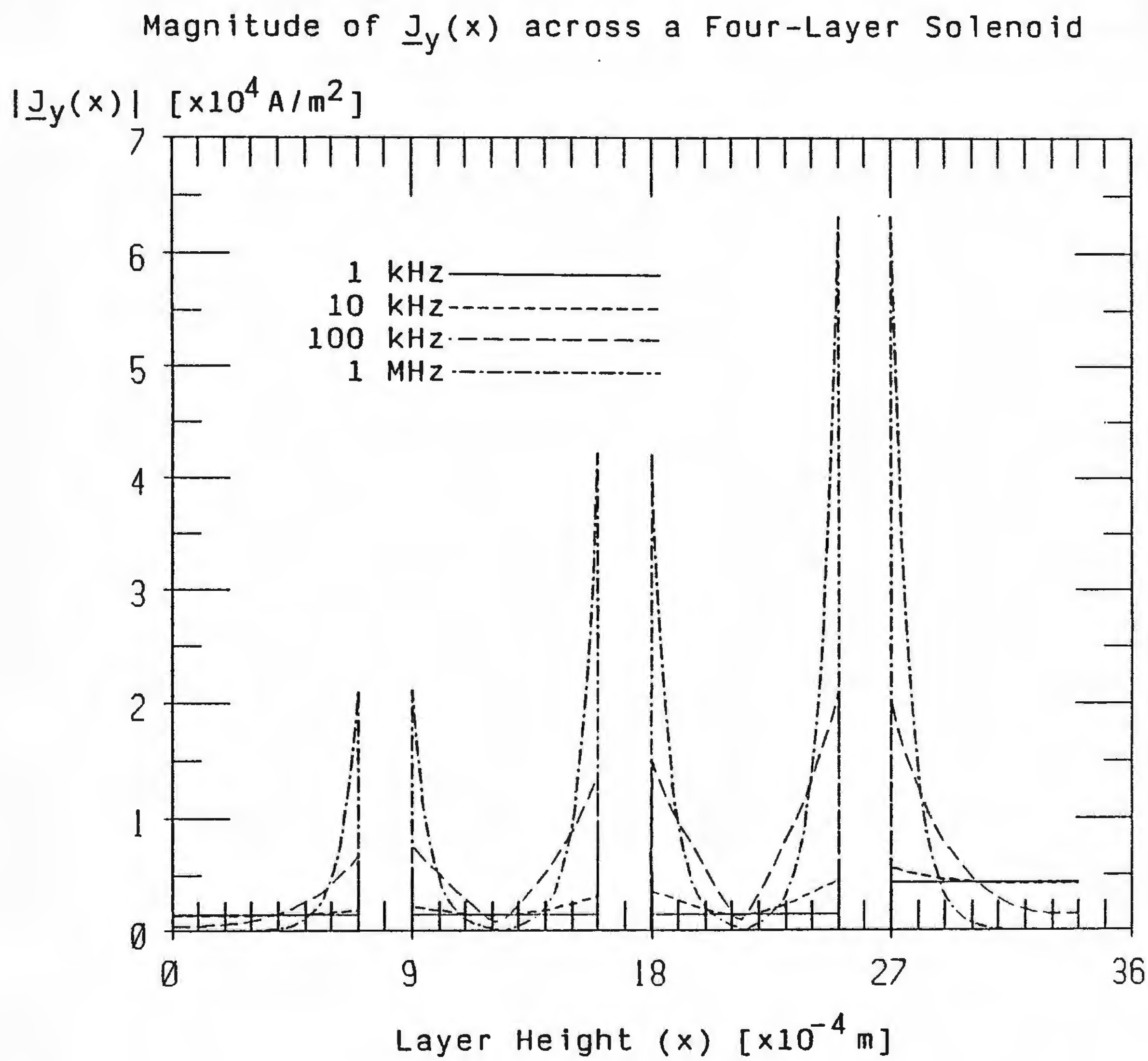

Figure 4.17: The magnitude of the current-density phasor distribution for the solenoid shown in Fig. 4.15.

the magnetic-field-intensity and current-density distributions, respectively, for the different layers of this four-layer solenoid. These plots are similar to those of Figs. 4.2 and 4.3; the magnetic-field-intensity boundary conditions are chosen so that each of the inner winding layers contributes one unit to the net magnetic field and the outer layer contributes a total of three units. Note that since all of the magnetic-field boundary conditions are in phase, we obtain from equation (4.49) that the value of β for each layer is zero, just as it is for the single layer of Sections 4.3.1 and 4.3.2. Also, we see from the limiting condition of low frequency given by (4.68) that, for any given layer, the phase angle of the net current-density phasor is either 0° or 180°, depending upon whether the magnitude of the magnetic field intensity is greater at $x = 0$ or at $x = h_{cu}$. That is, the *net* current in each of the winding layers is either in phase or 180° out of phase with the fields at the layer surfaces. In the plots of Figs. 4.16 and 4.17, the inner three layers carry a net current of one unit and the outer layer carries a net three units of current.

The four curves that are plotted in each figure show the field distributions for four different excitation frequencies ranging from one kilohertz to one megahertz. The solid-line in each figure shows the field distribution for the lowest-frequency of excitation; these solid-line plots are close to the "straight-line" field-intensity diagrams that were used earlier in Section 3.1.2 to determine the boundary conditions for the various layers. At high frequencies, we see that the magnitudes of the magnetic field intensity and current density both decrease sharply in the interior of the layers. The boundary conditions are set for the magnetic field intensity; therefore, the surface values of $|\underline{H}_z(x)|$ remain constant, while the magnitude of the current density increases dramatically on the winding-layer surfaces. By observing only the magnitudes of the current-density distributions in Fig. 4.17, it is not at all apparent that the net current in each of the three inner windings is the same for each of the four frequencies shown. For this reason, we now look at the magnetic-field-intensity and current-density phasor distributions across this same four-layer solenoid in a series of isometric plots.

4.4.2 Plots of Phasors Across Four Layers

In the immediately preceding section, we introduce an example of a four-layer solenoid that is illustrated in Fig. 4.15. Based upon the assumption that the four layers of this solenoid can be modeled by four infinite current sheets, we then provide plots of the magnitude of $\underline{H}_z(x)$ and $\underline{J}_y(x)$ in Figs. 4.16 and 4.17. It is important to realize that the four-layer infinite solenoid of Fig. 4.15 is not a transformer *per se*, since there is no magnetic core. In other words, there is nothing inherent in this structure that places any constraints whatever on the magnetic fields in any of the three inter-layer gaps, or in the center of the solenoid. Therefore, we *intentionally* choose values for these magnetic fields so that our example four-layer solenoid has the appearance of a transformer with a core material of infinite permeability. That is, we choose the values of the magnetic fields in the air spaces so that the total number of ampere-turns across the four layers is zero. In Section 4.3.2, we use isometric plots to illustrate the complete $\underline{H}_z(x)$ and $\underline{J}_y(x)$ phasors for the single-layer example originally introduced in Section 4.3.1. In the same way, we now wish to show the complete phasors across all four layers for the infinite solenoid example that is introduced in Section 4.4.1. Figures 4.18 through 4.21 contain plots of the magnetic-field-intensity and current-density phasors for this four-layer example at the same four frequencies that are used in Figs. 4.16 and 4.17 where only the magnitudes of the phasors are plotted.

Figure 4.18 shows the variation of the $\underline{H}_z(x)$ and the $\underline{J}_y(x)$ phasors across four layers at an excitation frequency of 1 kHz, and Table 4.1 contains an illustrative set of data points corresponding to the two plots in Fig. 4.18. The magnetic-field-intensity phasor distribution is plotted on the upper set of axes in Figure 4.18, while the current-density phasor distribution is plotted on the lower set of axes. The upper set of axes in Fig. 4.18 and Table 4.1 reveal that, although there is some small variation in the phase of $\underline{H}_z(x)$ (less than 2°), the magnitude of $\underline{H}_z(x)$ varies essentially linearly across each of the four layers. Note that to avoid unnecessary cluttering of the drawings, there are no magnetic-field-intensity phasors plotted in the three interlayer gaps; the solid line that would be connecting their tips is shown, however. This is because we have assumed that the magnetic field intensity in each interlayer gap is a sinusoid of constant magnitude and phase, regardless of the excitation frequency. Therefore, the magnetic-field-intensity phasor $\underline{H}_z(x)$ remains constant in the interlayer gaps and need not be plotted. Also note that the layer between $x = 9 \times 10^{-4}$ m and $x = 16 \times 10^{-4}$ m has *exactly* the same boundary conditions as the single layer that is illustrated in Section 4.3.2. Therefore, at each frequency, the layer between $x = 9 \times 10^{-4}$ m and $x = 16 \times 10^{-4}$ m exhibits the exact same $\underline{H}_z(x)$ and $\underline{J}_y(x)$ distributions as is seen for the single-layer example of Section 4.3.2.

The plot of the current-density phasors on the lower set of axes in Fig. 4.18 and the values in Table 4.1 suggest that at 1 kHz the currents in each of the four layers is almost uniformly distributed, since the magnitude and phase of $\underline{J}_y(x)$ across each layer is approximately constant. The magnitude of $\underline{J}_y(x)$ across any of the four layers varies by no more than 5%, while the phase varies by no more than 29°. Also, we see from Fig. 4.18 that the current density in the outer layer is three times greater in magnitude, and 180° out of phase with respect to the current density in each of the three inner layers. Therefore, if we consider each of our layers to consist of a single turn of conductor, then the instantaneous sum of the ampere-turns across the four layers is in fact zero.

Figures 4.19 through 4.21 show the progression of the magnetic-field-intensity and current-density phasor distributions for excitation frequencies of 10 kHz, 100 kHz and 1 MHz, and Tables 4.2 through 4.4 contain corresponding data points. The changes in the phasor distributions of a single layer as the frequency increases have already been discussed above in Section 4.3.2, and the same arguments apply to each of the four layers in this section. In general, we see that as the frequency increases, the magnitude of both $\underline{H}_z(x)$ and $\underline{J}_y(x)$ becomes attenuated near the center of each layer, while the magnitude of $\underline{J}_y(x)$ becomes much greater near the surfaces of each layer. In other words, the alternating magnetic field's diminishing ability to penetrate deep into each winding layer causes the current to be concentrated in regions near the surfaces of each

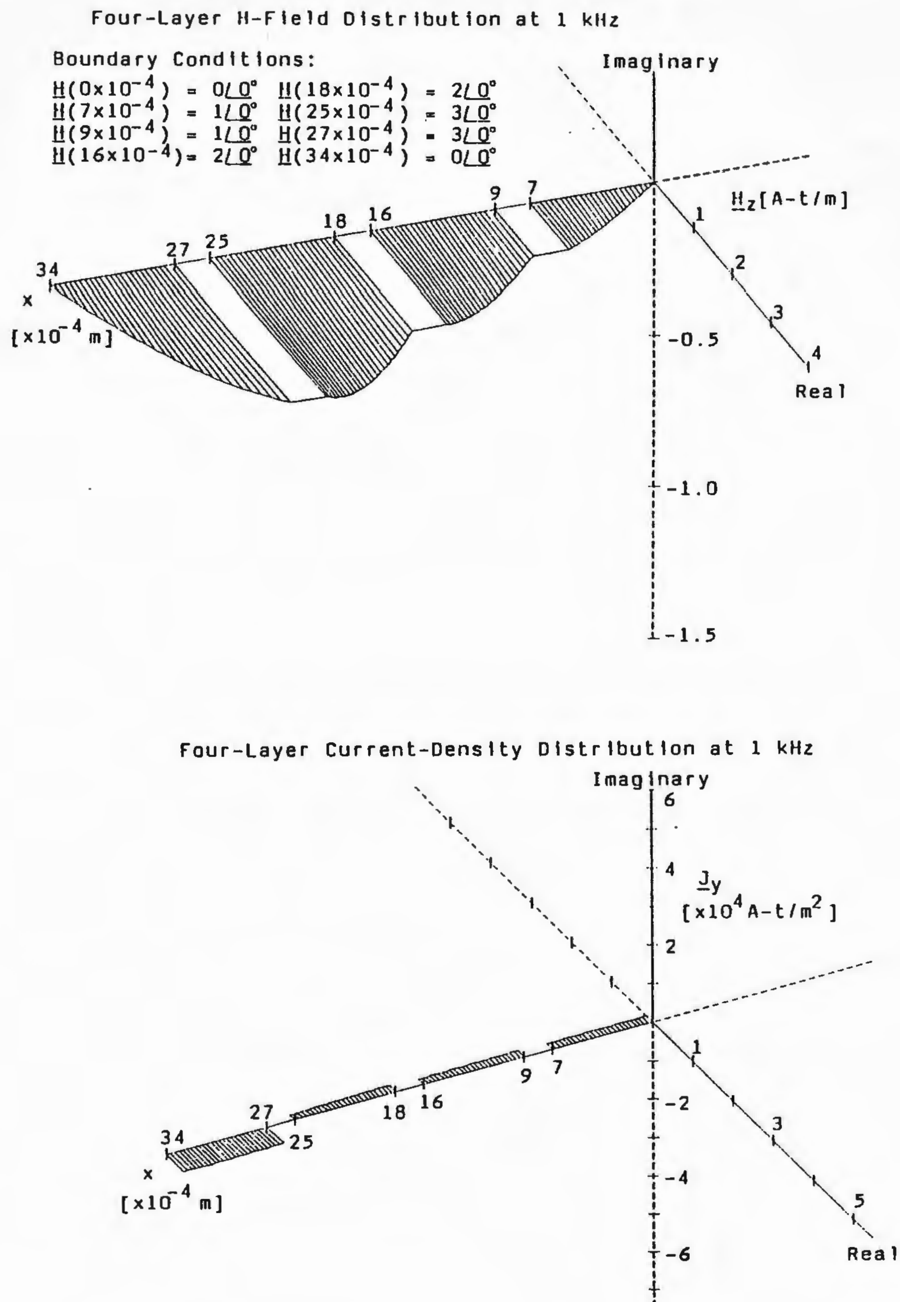

Figure 4.18: The magnetic-field-intensity and current-density phasor distributions across the four-layer solenoid of Fig. 4.15 at an excitation frequency of 1 kHz.

Table 4.1: Selected Data Points for the 1 kHz Example of Fig. 4.18

1 kHz

X	H_mag	H_phase	J_mag	J_phase
0.00000e+00	0.00000e+00	0.0000	1.42824e+03	178.0365
1.00000e-04	1.42824e-01	-1.9234	1.42824e+03	178.1568
2.00000e-04	2.85648e-01	-1.8032	1.42827e+03	178.5174
3.00000e-04	4.28474e-01	-1.6028	1.42841e+03	179.1185
4.00000e-04	5.71309e-01	-1.3223	1.42877e+03	179.9597
5.00000e-04	7.14162e-01	-0.9616	1.42955e+03	181.0406
6.00000e-04	8.57050e-01	-0.5209	1.43095e+03	182.3602
7.00000e-04	1.00000e+00	0.0000	1.43326e+03	183.9164
8.00000e-04	1.00000e+00	0.0000	0.00000e+00	0.000000
9.00000e-04	1.00000e+00	0.0000	1.43827e+03	172.1772
1.00000e-03	1.14263e+00	-0.8714	1.43322e+03	173.9600
1.10000e-03	1.28542e+00	-1.3356	1.42977e+03	175.9946
1.20000e-03	1.42825e+00	-1.4906	1.42835e+03	178.2770
1.30000e-03	1.57109e+00	-1.3988	1.42945e+03	180.8003
1.40000e-03	1.71395e+00	-1.1019	1.43359e+03	183.5545
1.50000e-03	1.85688e+00	-0.6287	1.44131e+03	186.5254
1.60000e-03	2.00000e+00	0.0000	1.45318e+03	189.6950
1.70000e-03	2.00000e+00	0.0000	0.00000e+03	0.000000
1.80000e-03	2.00000e+00	0.0000	1.46304e+03	166.4577
1.90000e-03	2.14247e+00	-0.8013	1.44581e+03	169.8144
2.00000e-03	2.28521e+00	-1.2772	1.43402e+03	173.4819
2.10000e-03	2.42803e+00	-1.4708	1.42860e+03	177.4356
2.20000e-03	2.57087e+00	-1.4158	1.43043e+03	181.6400
2.30000e-03	2.71373e+00	-1.1388	1.44037e+03	186.0494
2.40000e-03	2.85672e+00	-0.6611	1.45916e+03	190.6099
2.50000e-03	3.00000e+00	0.0000	1.48741e+03	195.2626
2.60000e-03	3.00000e+00	0.0000	0.00000e+03	0.000000
2.70000e-03	3.00000e+00	0.0000	4.29978e+03	3.9164
2.80000e-03	2.57115e+00	-0.5209	4.29285e+03	2.3602
2.90000e-03	2.14248e+00	-0.9616	4.28864e+03	1.0406
3.00000e-03	1.71393e+00	-1.3223	4.28632e+03	-0.0403
3.10000e-03	1.28542e+00	-1.6028	4.28522e+03	-0.8815
3.20000e-03	8.56943e-01	-1.8032	4.28481e+03	-1.4826
3.30000e-03	4.28471e-01	-1.9234	4.28471e+03	-1.8432
3.40000e-03	0.00000e+00	0.0000	4.28471e+03	-1.9635

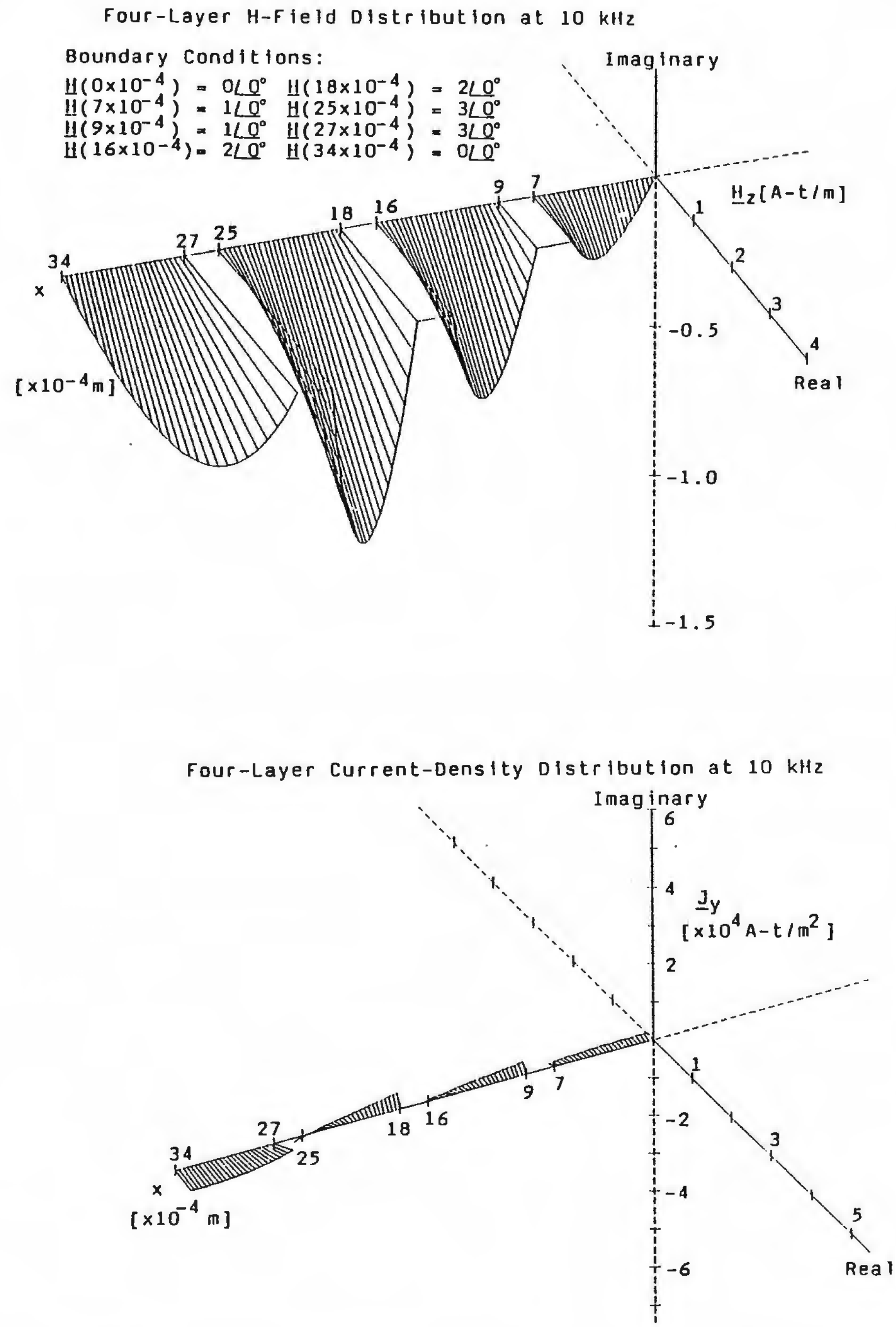

Figure 4.19: The magnetic-field-intensity and current-density phasor distributions across the four-layer solenoid of Fig. 4.15 at an excitation frequency of 10 kHz.

Table 4.2: Selected Data Points for the 10 kHz Example of Fig. 4.19

10 kHz

X	H_mag	H_phase	J_mag	J_phase
0.00000e+00	0.00000e+00	0.0000	1.39605e+03	160.5350
1.00000e-04	1.39606e-01	-19.0642	1.39625e+03	161.7372
2.00000e-04	2.79253e-01	-17.8621	1.39932e+03	165.3379
3.00000e-04	4.19145e-01	-15.8594	1.41255e+03	171.2874
4.00000e-04	5.59816e-01	-13.0592	1.44760e+03	179.4014
5.00000e-04	7.02282e-01	-9.4696	1.51902e+03	189.2615
6.00000e-04	8.48201e-01	-5.1070	1.64145e+03	200.2059
7.00000e-04	1.00000e+00	0.0000	1.82655e+03	211.4858
8.00000e-04	1.00000e+00	0.0000	0.00000e+00	0.000000
9.00000e-04	1.00000e+00	0.0000	2.16940e+03	119.7010
1.00000e-03	1.12119e+00	-8.5506	1.82064e+03	127.6220
1.10000e-03	1.25745e+00	-13.1865	1.53880e+03	141.7406
1.20000e-03	1.39771e+00	-14.7382	1.40691e+03	162.9370
1.30000e-03	1.53841e+00	-13.8219	1.51001e+03	186.9886
1.40000e-03	1.68132e+00	-10.8587	1.84820e+03	207.1418
1.50000e-03	1.83220e+00	-6.1601	2.35569e+03	221.8426
1.60000e-03	2.00000e+00	0.0000	2.97797e+03	232.8359
1.70000e-03	2.00000e+00	0.0000	0.00000e+00	0.000000
1.80000e-03	2.00000e+00	0.0000	3.40711e+03	104.1605
1.90000e-03	2.10528e+00	-7.8573	2.60577e+03	110.1328
2.00000e-03	2.23670e+00	-12.6034	1.88065e+03	124.4120
2.10000e-03	2.37636e+00	-14.5405	1.43102e+03	154.6951
2.20000e-03	2.51707e+00	-13.9915	1.59658e+03	193.8641
2.30000e-03	2.66062e+00	-11.2253	2.29856e+03	218.8485
2.40000e-03	2.81638e+00	-6.4772	3.24257e+03	232.6002
2.50000e-03	3.00000e+00	0.0000	4.30640e+03	241.7189
2.60000e-03	3.00000e+00	0.0000	0.00000e+00	0.000000
2.70000e-03	3.00000e+00	0.0000	5.47965e+03	31.4858
2.80000e-03	2.54460e+00	-5.1070	4.92434e+03	20.2059
2.90000e-03	2.10685e+00	-9.4696	4.55705e+03	9.2615
3.00000e-03	1.67945e+00	-13.0592	4.34280e+03	-0.5986
3.10000e-03	1.25744e+00	-15.8594	4.23765e+03	-8.7126
3.20000e-03	8.37758e-01	-17.8621	4.19796e+03	-14.6621
3.30000e-03	4.18818e-01	-19.0642	4.18875e+03	-18.2628
3.40000e-03	0.00000e+00	0.0000	4.18814e+03	-19.4650

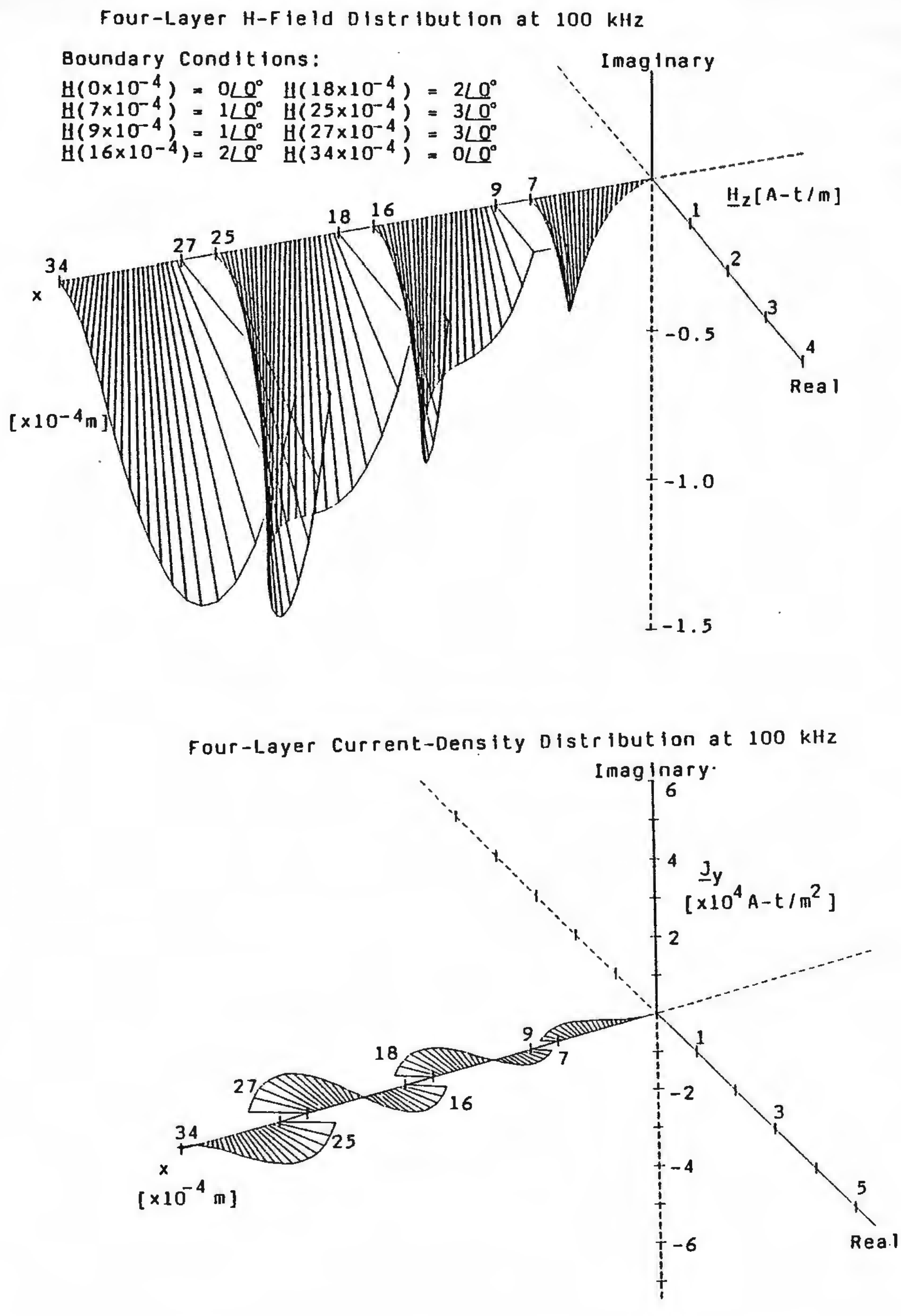

Figure 4.20: The magnetic-field-intensity and current-density phasor distributions across the four-layer solenoid of Fig. 4.15 at an excitation frequency of 100 kHz.

Table 4.3: Selected Data Points for the 100 kHz Example of Fig. 4.20

100 kHz

X	H_mag	H_phase	J_mag	J_phase
0.00000e+00	0.00000e+00	0.0000	5.25562e+02	41.2696
1.00000e-04	5.26076e-02	225.2756	5.33222e+02	53.1994
2.00000e-04	1.06749e-01	237.2053	6.37812e+02	84.5987
3.00000e-04	1.69836e-01	256.3328	9.77408e+02	118.5125
4.00000e-04	2.59097e-01	280.5344	1.60558e+03	147.0011
5.00000e-04	4.01272e-01	306.9156	2.59249e+03	173.0797
6.00000e-04	6.31702e-01	333.5756	4.11599e+03	198.9081
7.00000e-04	1.00000e+00	360.0000	6.49919e+03	224.9757
8.00000e-04	1.00000e+00	360.0000	0.00000e+00	0.000000
9.00000e-04	1.00000e+00	0.0000	7.54842e+03	44.4600
1.00000e-03	6.06942e-01	-35.8975	5.03306e+03	25.7643
1.10000e-03	5.15767e-01	-75.9305	2.85883e+03	19.5702
1.20000e-03	5.85708e-01	-93.2190	9.39182e+02	63.8825
1.30000e-03	6.76694e-01	-85.3711	2.39787e+03	158.2123
1.40000e-03	8.45511e-01	-59.8853	5.20725e+03	180.1128
1.50000e-03	1.24788e+00	-28.7183	8.67772e+03	200.8921
1.60000e-03	2.00000e+00	0.0000	1.35229e+04	224.8317
1.70000e-03	2.00000e+00	0.0000	0.00000e+00	0.000000
1.80000e-03	2.00000e+00	0.0000	1.45721e+04	44.5750
1.90000e-03	1.22306e+00	-33.4615	9.59601e+03	24.2973
2.00000e-03	9.61707e-01	-71.2844	5.47898e+03	13.5126
2.10000e-03	1.00487e+00	-91.4626	1.53561e+03	32.6161
2.20000e-03	1.09599e+00	-86.7649	3.23589e+03	163.7482
2.30000e-03	1.29345e+00	-61.9907	7.84794e+03	182.4309
2.40000e-03	1.86475e+00	-29.4952	1.32427e+04	201.5086
2.50000e-03	3.00000e+00	0.0000	2.05466e+04	224.7862
2.60000e-03	3.00000e+00	0.0000	0.00000e+00	0.000000
2.70000e-03	3.00000e+00	0.0000	1.94976e+04	44.9757
2.80000e-03	1.89510e+00	-26.4244	1.23480e+04	18.9081
2.90000e-03	1.20382e+00	-53.0844	7.77747e+03	-6.9203
3.00000e-03	7.77290e-01	-79.4656	4.81675e+03	-32.9989
3.10000e-03	5.09508e-01	-103.6672	2.93222e+03	-61.4875
3.20000e-03	3.20246e-01	-122.7947	1.91344e+03	-95.4013
3.30000e-03	1.57823e-01	-134.7244	1.59967e+03	-126.8006
3.40000e-03	0.00000e+00	0.0000	1.57668e+03	-138.7304

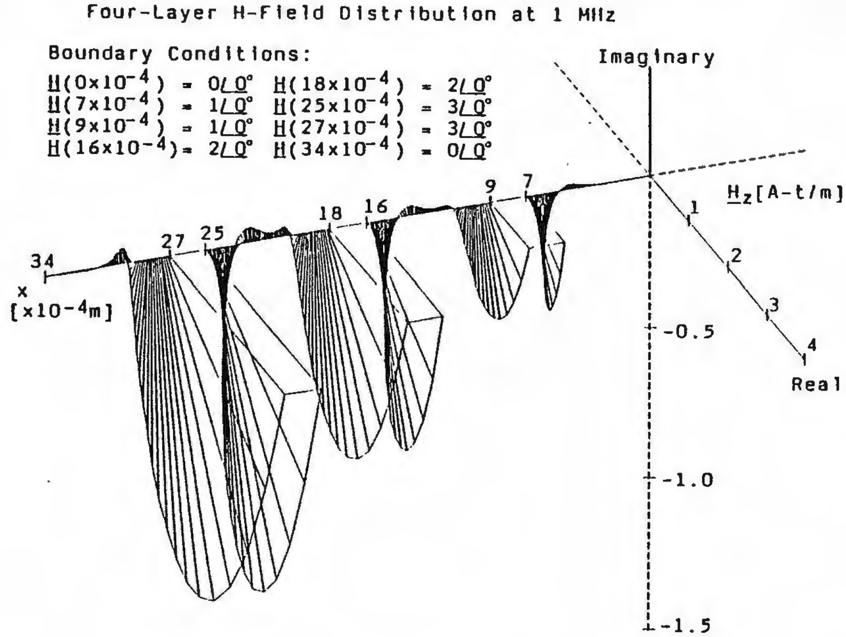

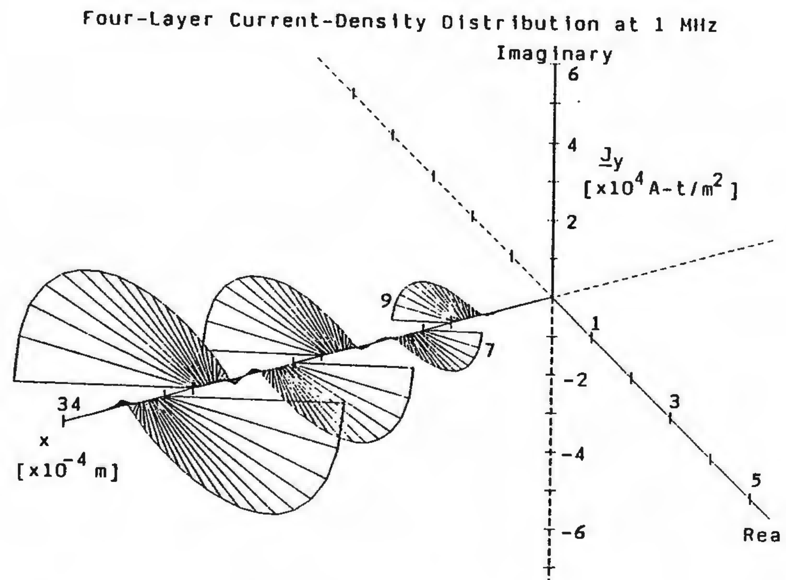

Figure 4.21: The magnetic-field-intensity and current-density phasor distributions across the four-layer solenoid of Fig. 4.15 at an excitation frequency of 1 MHz.

Table 4.4: Selected Data Points for the 1 MHz Example of Fig. 4.21

1 MHz

X	H_mag	H_phase	J_mag	J_phase
0.00000e+00	0.00000e+00	0.0000	1.61739e+00	4.0321
1.00000e-04	1.77060e-04	222.7539	3.25855e+00	86.2188
2.00000e-04	7.13443e-04	304.9407	1.46940e+01	170.1046
3.00000e-04	3.04563e-03	388.0248	6.23756e+01	253.0119
4.00000e-04	1.29633e-02	471.0133	2.65562e+02	336.0142
5.00000e-04	5.51838e-02	554.0092	1.13047e+03	419.0091
6.00000e-04	2.34912e-01	637.0046	4.81229e+03	502.0046
7.00000e-04	1.00000e+00	720.0000	2.04855e+04	585.0000
8.00000e-04	1.00000e+00	0.000000	0.00000e+00	0.00000
9.00000e-04	1.00000e+00	0.0000	2.04879e+04	44.9941
1.00000e-03	2.35119e-01	-83.0655	4.80863e+03	-37.9312
1.10000e-03	5.46902e-02	-164.5945	1.14137e+03	-122.3674
1.20000e-03	1.49809e-02	-272.7877	2.79309e+02	-177.6703
1.30000e-03	2.64715e-02	-255.5438	5.27172e+02	-17.2415
1.40000e-03	1.10115e-01	-165.6441	2.26626e+03	58.6625
1.50000e-03	4.69928e-01	-83.0129	9.62276e+03	142.0206
1.60000e-03	2.00000e+00	0.0000	4.09722e+04	224.9985
1.70000e-03	2.00000e+00	0.000000	0.00000e+00	0.00000
1.80000e-03	2.00000e+00	0.0000	4.09747e+04	44.9956
1.90000e-03	4.70135e-01	-83.0480	9.61909e+03	-37.9473
2.00000e-03	1.09621e-01	-164.9459	2.27717e+03	-122.0257
2.10000e-03	2.85219e-02	-267.5257	5.41195e+02	-183.9144
2.20000e-03	4.00918e-02	-257.6598	7.91236e+02	-14.9825
2.30000e-03	1.65047e-01	-165.5282	3.40209e+03	58.5474
2.40000e-03	7.04944e-01	-83.0188	1.44332e+04	142.0260
2.50000e-03	3.00000e+00	-0.0000	6.14589e+04	224.9980
2.60000e-03	3.00000e+00	0.000000	0.00000e+00	0.00000
2.70000e-03	3.00000e+00	-0.0000	6.14565e+04	45.0000
2.80000e-03	7.04737e-01	-82.9954	1.44369e+04	-37.9954
2.90000e-03	1.65551e-01	-165.9908	3.39140e+03	-120.9909
3.00000e-03	3.88898e-02	-248.9867	7.96685e+02	-203.9858
3.10000e-03	9.13688e-03	-331.9752	1.87127e+02	-286.9881
3.20000e-03	2.14033e-03	-415.0593	4.40821e+01	-369.8954
3.30000e-03	5.31180e-04	-497.2461	9.77566e+00	-453.7812
3.40000e-03	0.00000e+00	0.0000	4.85218e+00	-535.9679

layer. Note, however, that there is no concentration of current density near the surfaces at $x = 0$ and at $x = 34 \times 10^{-4}$ m, since there is no magnetic field impending upon these surfaces (the boundary-value magnetic fields have zero magnitude). For the low-frequency cases of Figs. 4.18 and 4.19, the non-zero current densities that appear near the surfaces at $x = 0$ and $x = 34 \times 10^{-4}$ m are due only to the magnetic fields which are present near the surfaces at $x = 7 \times 10^{-4}$ m and $x = 27 \times 10^{-4}$ m, respectively. For the high-frequency cases of Figs. 4.20 and 4.21, however, the magnetic fields near the surfaces at $x = 7 \times 10^{-4}$ m and $x = 27 \times 10^{-4}$ m cannot penetrate as deeply into their respective layers. Accordingly, the magnitude of the current density at both $x = 0$ and $x = h_{cu}$ for the 100 kHz-case is reduced to about 37% of the corresponding values for the 1 kHz-case and, for the 1 MHz-case, the current density at these two points less than 1% of the corresponding values for the 1 kHz case. In Fig. 4.21, we can plainly see the substantial impact of skin effect as the magnetic field intensity becomes restricted to regions very close to the surfaces of each layer, and the current density becomes heavily concentrated in these same regions.

A final example that we wish to consider is illustrated in Fig. 4.22. Once again, we wish to model this four layer solenoid with four infinite current sheets, and intentionally establish a four-layer total of zero ampere-turns so that the solenoid resembles a real transformer with a high-permeability core. In this case, however, we choose two of the inner winding layers to carry 1.5 units of current each, and the outer winding to carry 3 units of current. Thus, one of the inner windings is left open-circuited, so that it has zero net current. Figures 4.23 through 4.26 show the distributions of $\underline{H}_z(x)$ and $\underline{J}_y(x)$ at each of the four frequencies used in the above examples. These distributions look similar to those seen in Figs. 4.18 through 4.21. On the lower set of axes in Fig. 4.23, note that there is no current flowing in the open-circuited winding layer which lies between $x = 9 \times 10^{-4}$ m and $x = 16 \times 10^{-4}$ m. However, as the frequency increases, we begin to see some current flow; for the 1 MHz case of Fig. 4.26, there are large current densities that appear in the open-circuited layer. Nevertheless, the net current density in this layer at every instant in time is still zero (as it must be) since there is an equal amount of current flowing in both the negative and the positive directions. In fact, the time variation of the actual current-density distribution for the open-circuited layer would be similar to that shown in the twelve plots of Fig 4.13, but would instead exhibit *precisely* odd symmetry about the center of the layer at each point in time.

The fact that such large currents can flow in an open-circuited conductor is not so surprising if we consider the fundamental origin of ac currents in a conductor. In Appendix D we show that it is the electric-field component of an electromagnetic wave that causes the sinusoidal currents to flow in a winding layer. If we focus on the open-circuited layer of Fig. 4.26, then we can say that the resulting distribution of magnetic field intensity and current density across this layer actually consists of a superposition of two transverse electromagnetic (TEM) waves. One wave originates at $x = 9 \times 10^{-4}$ m and travels to the left, while the other wave originates at $x = 16 \times 10^{-4}$ m and travels to the right. We know that the projection of the current-density phasors in the open-circuited

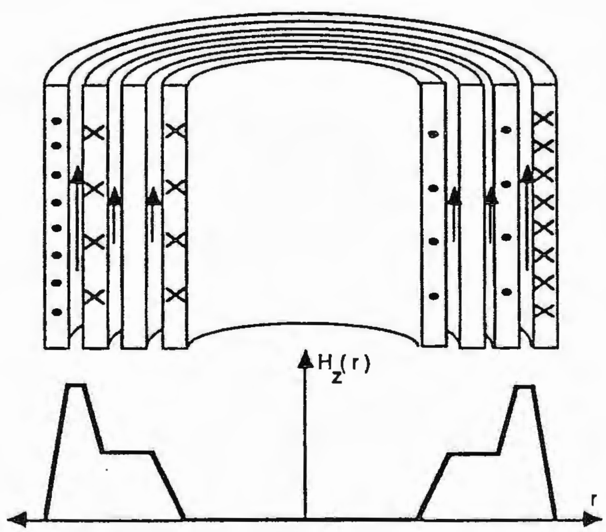

Figure 4.22: Structure of a four-layer solenoid. Two of the three inner layers are of the same winding while the other inner layer is left open circuited. The outer layer carries a current equal to the sum of the currents in the two current-carrying inner layers.

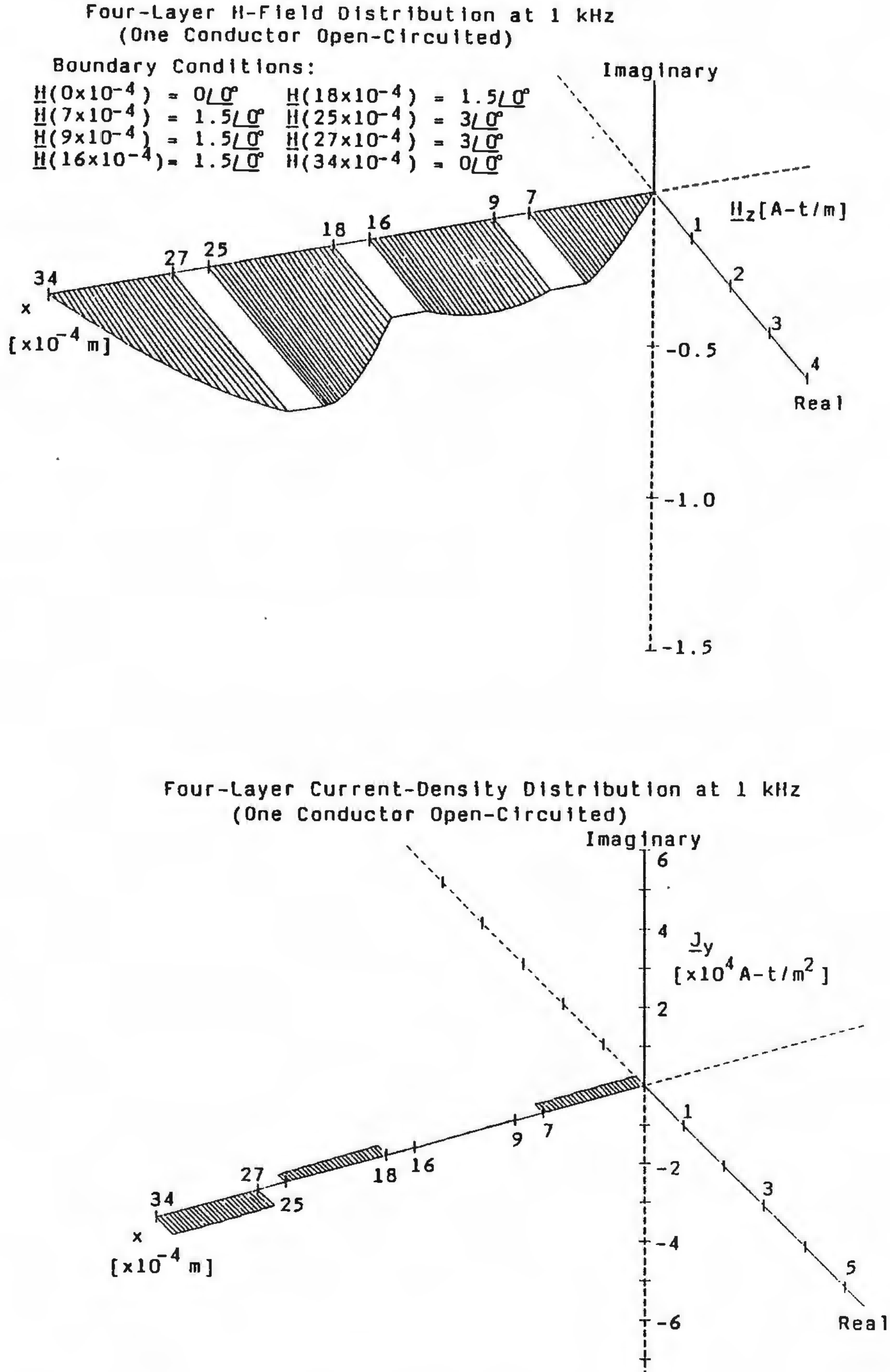

Figure 4.23: The magnetic-field-intensity and current-density phasor distributions across the four-layer solenoid of Fig. 4.22 at an excitation frequency of 1 kHz.

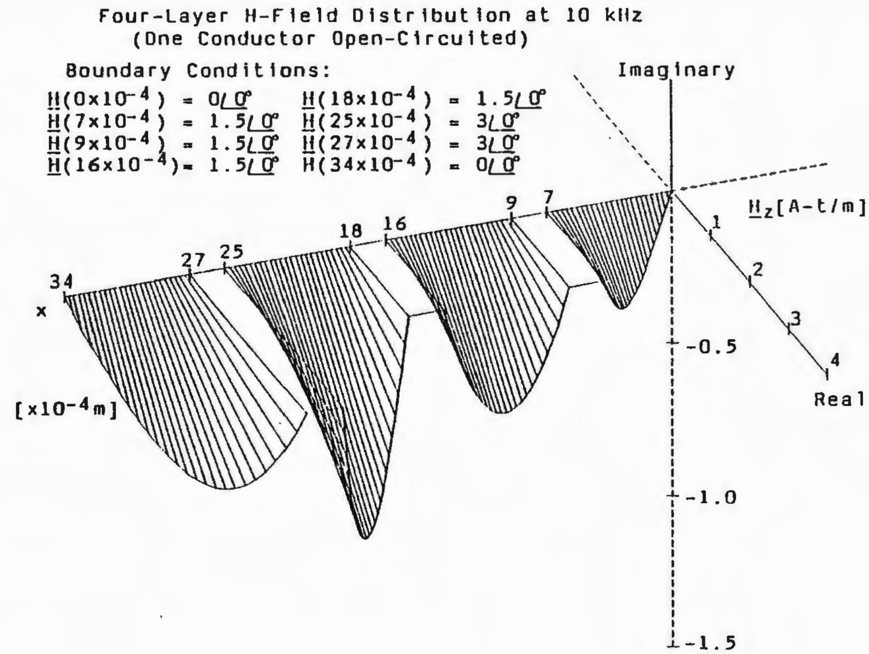

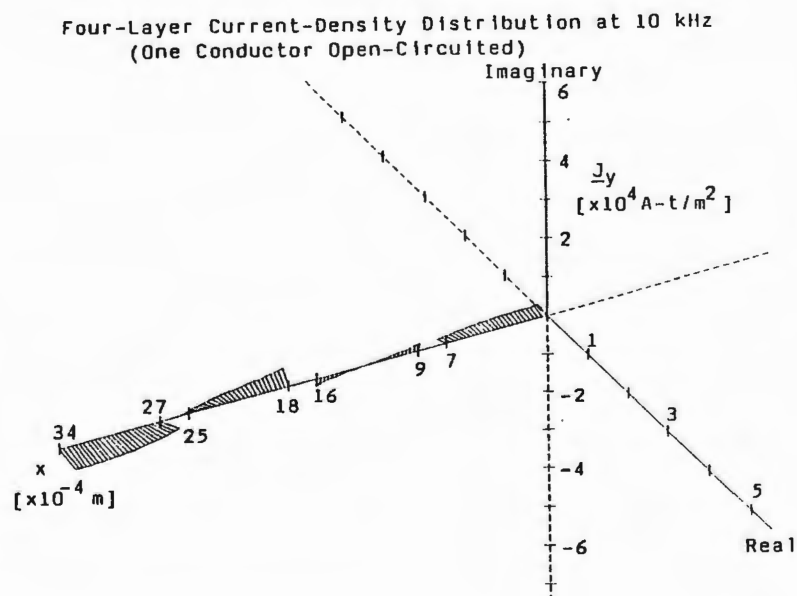

Figure 4.24: The magnetic-field-intensity and current-density phasor distributions across the four-layer solenoid of Fig. 4.22 at an excitation frequency of 10 kHz.

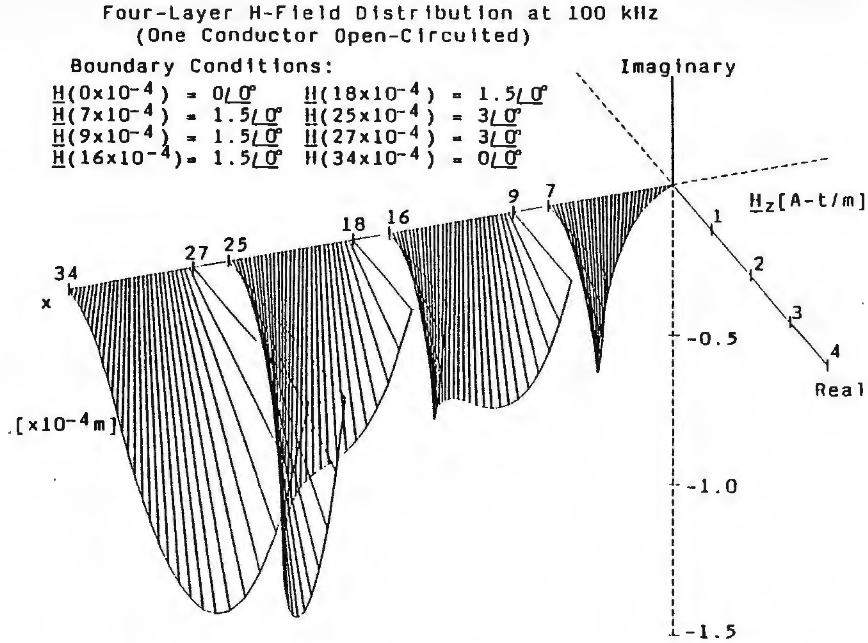

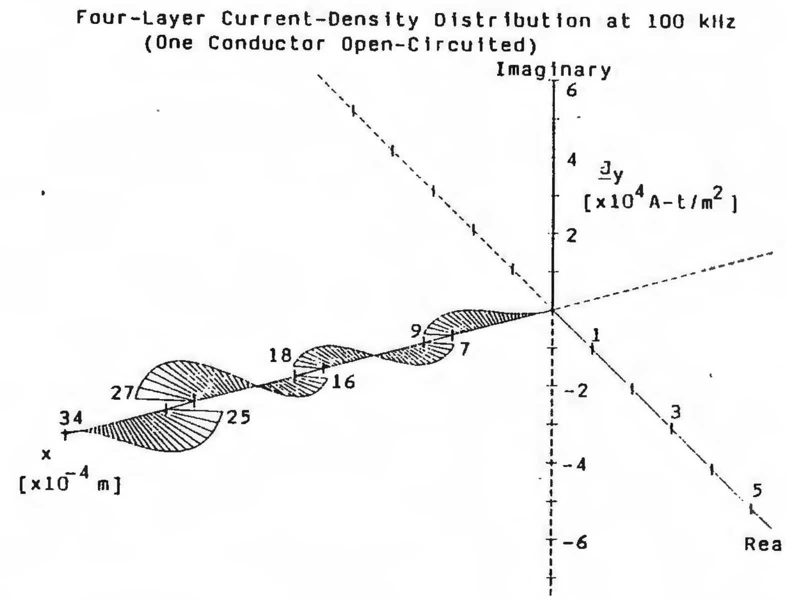

Figure 4.25: The magnetic-field-intensity and current-density phasor distributions across the four-layer solenoid of Fig. 4.22 at an excitation frequency of 100 kHz.

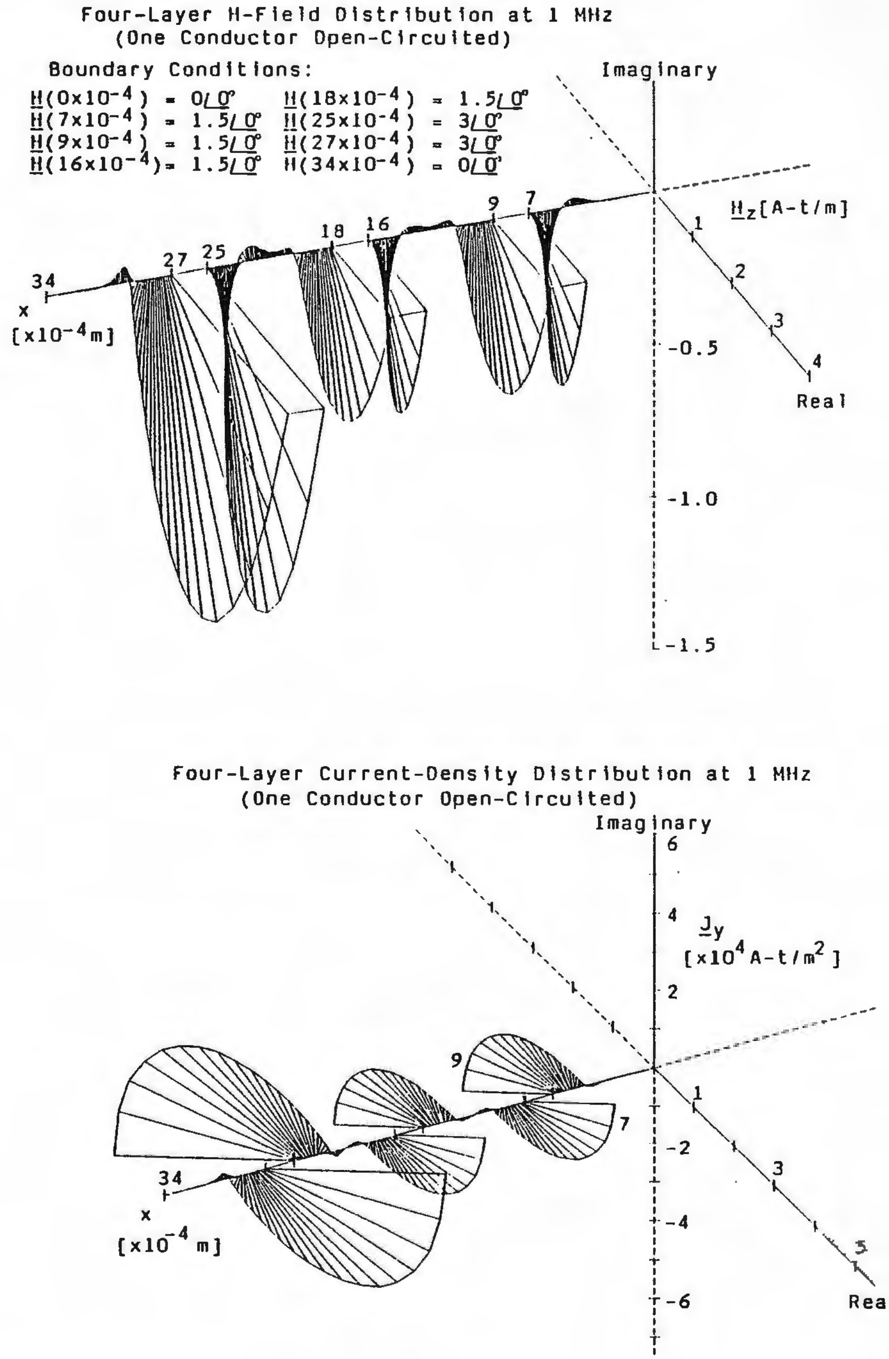

Figure 4.26: The magnetic-field-intensity and current-density phasor distributions across the four-layer solenoid of Fig. 4.22 at an excitation frequency of 1 MHz.

layer of Fig. 4.26 onto the x vs Re plane is proportional to the actual current-density distribution at the instant in time $\omega t = 0$. This particular distribution of real current density is actually a result of the fact that at that instant, the wave traveling to the left tends to generate a current that primarily flows in the $+y$-direction, while the wave traveling to the right tends to generate a current that primarily flows in the $-y$-direction. At low frequencies, where the wavelength of each TEM wave is much greater than the copper height h_{cu}, the influence of each wave extends completely across the layer, and, since the waves have opposing influences, there is no current density (Fig. 4.23). However, at higher frequencies, each of the TEM waves is almost completely attenuated before reaching the other side, and therefore each wave acts alone to generate current density in the appropriate direction near the surface from which it originates (Fig. 4.26).

The above examples and illustrations are intended to provide the reader with a better understanding of equations (4.36) and (4.39). In addition, by incorporating some of the basic physical principles that are developed in Appendix D, it may also be possible for the reader to gain greater insight into the fundamental origin and nature of skin effect and eddy currents. In either case, the above graphical illustrations emphasize the fact that skin effect can have a significant influence in determining the distributions of the magnetic field intensity and current density in the winding layer of a transformer. Our next logical step is to determine the effect of these distributions on the energy-storage and power-loss characteristics of a winding layer.

4.5 COMPUTATION OF POWER DISSIPATION AND ENERGY-STORAGE IN WINDING LAYERS FROM THE FIELD SOLUTIONS

4.5.1 Overview

In Section 4.2, expressions for the magnetic field intensity $\underline{H}_z$ and the current density $\underline{J}_y$ for any infinite current sheet are derived and presented in (4.50) and (4.51), respectively, as functions of the boundary conditions for the magnetic field intensity on the surfaces of the current sheet. In Section 3.1.2, it is shown that each layer of conductors in a transformer can be effectively modeled by an infinite current sheet. Thus, (4.50) and (4.51) describe the magnetic field intensity and the current density, respectively, at every point throughout the volume of any conductor layer in the transformer winding space. Such expressions can be utilized to calculate a value for the impedance between any two transformer windings. The development of an expression for the ac impedance requires the calculation of the ac winding resistance and the ac leakage inductance of the transformer under the appropriate winding-excitation conditions. Several additional new ideas apply to these calculations in general and are worth being emphasized at this point.

Providing the magnetizing inductance is relatively large, reflection indicates that the only reasonable use of the term *leakage inductance* is with reference to the total inductance that exists between *two windings taken as a pair*. For a simple two-winding transformer, there is only one such leakage inductance; in more complicated devices, however, there is a leakage inductance between each pair of windings. Therefore, in calculating formulae for leakage inductance in transformers, we want to keep in mind that the formulae are written for situations where only two windings of the device carry a net current. This is the same situation that exists when measuring the short-circuit impedance of a transformer in the laboratory. In such a test, one winding is short-circuited and one winding is excited from a source; if the device has any other windings, they are left open-circuited. The expressions that we derive for the impedance between two windings in the following discussion are based on such a *short-circuit test* condition.

The calculation of impedance can be divided into a calculation of the real and imaginary parts of the impedance. We derive separate expressions for both the resistive and the inductive components of the impedance between any two windings.

After the field solution has been obtained for the magnetic field intensity and the current density, the next step is to apply the field solution to model a transformer. Depending on the model assumed for the transformer—two models are proposed in Chapters 7 and 8—the various parameters associated with the equivalent model can be estimated either through laboratory measurements or through calculation based on the solutions to the magnetic field intensity and the current density derived in this chapter. It is shown in Chapter 5 that the estimation of the model parameters centers on the computation of the power losses and on the energy stored in the magnetic field in the space occupied by the winding layers. Hence, the calculation of the power losses and the energy stored in the winding layers is a crucial step in obtaining parameters for such models.

In general, the instantaneous power loss per unit volume $p_d(t)$ at a point is given by (3.16) and the instantaneous energy stored in the magnetic field per unit volume $w_m(t)$ at a point is given by (3.17). They are repeated here for convenience.

$$p_d(t) = \frac{|\mathbf{J}(t)|^2}{\sigma} \tag{4.69}$$

$$w_m(t) = \frac{\mu_0\,|\mathbf{H}(t)|^2}{2} \tag{4.70}$$

The total instantaneous conduction loss $P_n(t)$ and the total instantaneous energy $W_n(t)$ stored in the magnetic field in the n^{th} conducting layer are then equal, respectively, to the volume integrals of $p_d(t)$ and $w_m(t)$ over the volume occupied by the n^{th} layer.

$$P_n(t) = \iiint_{V_n} p_d(t)\,d\nu = \iiint_{V_n} \frac{|\mathbf{J}(t)|^2}{\sigma}\,d\nu \tag{4.71}$$

$$W_n(t) = \iiint_{V_n} w_m(t)\,d\nu = \iiint_{V_n} \frac{\mu_0\,|\mathbf{H}(t)|^2}{2}\,d\nu \tag{4.72}$$

where the subscript V_n in the integration symbol is used to remind us that this volume integral is carried out over the winding space occupied by the n^{th} layer. Since the current density in the air space between winding layers is equal to zero, the resistive portion of the leakage impedance can be computed entirely from the power loss P_n in the winding layers. On the other hand, the magnetic field intensity is not equal to zero in the air space between winding layers. Therefore, the estimation of the reactive portion of the leakage impedance requires not only the computation of W_n, the energy stored in the magnetic field in the winding layers, but also the computation of the energy stored in the magnetic field in the air space between winding layers. The computation of the energy stored in the air space will be discussed in more detail in Section 5.2.5.2.

As will be shown later in Sections 4.5.2 and 4.5.3, it is easier in the case of sinusoidal excitation to work with the average power loss and average energy storage over one period T of the sinusoid. Taking the average of the instantaneous conducting loss $P_n(t)$ and the instantaneous energy storage $W_n(t)$ defined in (4.71) and (4.72) then gives

$$\langle P_n \rangle = \frac{1}{T}\int_T \iiint_{V_n} \frac{|\mathbf{J}(t)|^2}{\sigma}\, d\nu\, dt \tag{4.73}$$

$$\langle W_n \rangle = \frac{1}{T}\int_T \iiint_{V_n} \frac{\mu_0\,|\mathbf{H}(t)|^2}{2}\, d\nu\, dt \tag{4.74}$$

where the symbols $\langle P_n \rangle$ and $\langle W_n \rangle$ are used to represent the power loss and the energy storage in the space of the n^{th} winding layer, respectively, averaged over one period of excitation. The integration with respect to volume and the integration with respect to time can be interchanged:

$$\langle P_n \rangle = \iiint_{V_n} \left(\frac{1}{T}\int_T \frac{|\mathbf{J}(t)|^2}{\sigma}\, dt\right) d\nu \tag{4.75}$$

$$\langle W_n \rangle = \iiint_{V_n} \left(\frac{1}{T}\int_T \frac{\mu_0\,|\mathbf{H}(t)|^2}{2}\, dt\right) d\nu \tag{4.76}$$

By defining the results of the integration with respect to time as

$$\langle p_d \rangle = \frac{1}{T}\int_T \frac{|\mathbf{J}(t)|^2}{\sigma}\, dt \tag{4.77}$$

$$\langle w_m \rangle = \frac{1}{T}\int_T \frac{\mu_0\,|\mathbf{H}(t)|^2}{2}\, dt \tag{4.78}$$

where $\langle p_d \rangle$ and $\langle w_m \rangle$ are the average power loss per unit volume and the average energy storage per unit volume, respectively, the average power dissipated and the average energy storage in the volume of the n^{th} layer can be rewritten as:

$$\langle P_n \rangle = \iiint_{V_n} \langle p_d \rangle\, d\nu \tag{4.79}$$

$$\langle W_n \rangle = \iiint_{V_n} \langle w_m \rangle \, d\nu \tag{4.80}$$

For the n^{th} winding layer, the height x varies from zero to h_{cu}, the depth y varies from zero to the mean length of turn for the n^{th} layer ℓ_{T_n}, and the breadth z varies from zero to b_{win}. The terms *height*, *breadth*, and *depth* are defined in Section 2.1. The integrations in (4.79) and (4.80) become

$$\langle P_n \rangle = \int_0^{b_{win}} \int_0^{\ell_{T_n}} \int_0^{h_{cu}} \langle p_d \rangle \, dx \, dy \, dz \tag{4.81}$$

$$\langle W_n \rangle = \int_0^{b_{win}} \int_0^{\ell_{T_n}} \int_0^{h_{cu}} \langle w_m \rangle \, dx \, dy \, dz \tag{4.82}$$

The expressions derived for the phasors of the magnetic field intensity and for the current density, (4.50) and (4.51), indicate that the magnetic field intensity and the current density are dependent on the height x but not on the depth y nor the breadth z. This implies that the average loss density $\langle p_d \rangle$ and the average energy storage density $\langle w_m \rangle$ are dependent on x but not on y nor z. As a result, it is advantageous to evaluate the volume integrals in (4.81) and (4.82) in two steps; the first step is a single integration in the x-direction, and the second step is a double integration involving the y- and z-directions. Let us define the results of the integrations with respect to x as:

$$\langle Q_J \rangle = \int_0^{h_{cu}} \langle p_d \rangle \, dx \tag{4.83}$$

$$\langle Q_H \rangle = \int_0^{h_{cu}} \langle w_m \rangle \, dx \tag{4.84}$$

Then the double integration with respect to y and z becomes trivial multiplication processes as the integrands $\langle Q_J \rangle$ and $\langle Q_H \rangle$ are independent of y and z, giving

$$\begin{aligned} \langle P_n \rangle &= \int_0^{b_{win}} \int_0^{\ell_{T_n}} \langle Q_J \rangle \, dy \, dz \\ &= b_{win} \, \ell_{T_n} \, \langle Q_J \rangle \end{aligned} \tag{4.85}$$

$$\begin{aligned} \langle W_n \rangle &= \int_0^{b_{win}} \int_0^{\ell_{T_n}} \langle Q_H \rangle \, dy \, dz \\ &= b_{win} \, \ell_{T_n} \, \langle Q_H \rangle \end{aligned} \tag{4.86}$$

The benefit of evaluating the integral over the x coordinate first is that the resulting formulae yield the average power dissipation $\langle Q_J \rangle$ and the average energy storage $\langle Q_H \rangle$

per square meter of conductor in the y-z plane. These expressions are written in terms of the boundary conditions so that the results are general for any winding layer. Once the integrations have been evaluated over the height (x-coordinate) of a current sheet, the results can be multiplied by the depth and breadth of the winding layer to get the complete volume integrals. The derivation of $\langle Q_J \rangle$ and $\langle Q_H \rangle$ are presented in details in the next two sections.

J.P. Vandelac and P. Ziogas follow a procedure such as this to calculate the total power dissipation in a winding layer [19]; M.P. Perry in [13] evaluates the integration only over the layer height to derive expressions for power dissipation *per square meter of conductor in the breadth-depth plane.* These two analyses are both dependent on the actual currents in the transformer windings under load, and neither of them address the inductance of the windings at all. Their techniques are general and form the basis for the discussion here, but we do not follow the application of their results directly since we are interested in determining the load-independent circuit impedances. The type of analysis that both of these authors pursue is aimed more at a quantification of total winding *losses* than toward the development of a *circuit model* which can be used to predict the transformer terminal voltage characteristics. In the next sections, we present the main points of the solution for both average power loss $\langle Q_J \rangle$ and average energy storage $\langle Q_H \rangle$ per square meter in the y-z plane in a winding layer. The results of this solution for a single layer are then used to calculate the characteristic impedances of a multiwinding transformer.

4.5.2 Average Power Dissipation Per Square Meter of an Infinite Current Sheet

Equation (4.77) defines, for the case of periodic excitation, the average power dissipated per unit volume as

$$\langle p_d \rangle = \frac{1}{T} \int_T \frac{|\mathbf{J}(t)|^2}{\sigma}\, dt \tag{4.87}$$

where $\mathbf{J}(t)$ is the instantaneous current density at any point in an infinite current sheet. Since the current density in our model transformer has a nonzero component only in the y-direction, (4.87) can be further simplified to

$$\langle p_d \rangle = \frac{1}{T} \int_T \frac{|J_y(t)|^2}{\sigma}\, dt \tag{4.88}$$

The solutions for the current density and the magnetic field intensity derived in the previous sections, however, are in the form of phasor variables. Although the equivalent time-domain functions can always be computed from the phasor variables, one can take advantage of the complex arithmetic and work directly with the phasor variables. First, consider that the excitation is at an angular frequency ω where $\omega = 2\pi/T$. Since the excitation is sinusoidal, the current density $J_y(t)$ and its corresponding phasor representation $\underline{J}_y$ can be assumed to take the forms of

$$J_y(t) = \sqrt{2}\,|\underline{J}_y|\,\cos(\omega t + \theta_J) \tag{4.89}$$

$$\underline{J}_y = |\underline{J}_y|\,e^{j\,\theta_J} \tag{4.90}$$

where $|\underline{J}_y|$, the magnitude of $\underline{J}_y$, is also the rms value of the current density. It is understood that the current density is also a function of the height x and its dependence on x is not explicitly shown here. Substituting (4.89) into (4.88) and carrying out the integration with respect to time yields

$$\begin{aligned}\langle p_d\rangle &= \frac{1}{T}\int_T \frac{2\,|\underline{J}_y|^2\cos^2(\omega t+\theta_J)}{\sigma}\,dt \\ &= \frac{|\underline{J}_y|^2}{\sigma}\end{aligned} \tag{4.91}$$

By definition, the product of the phasor $\underline{J}_y$ and its complex conjugate $\underline{J}_y^*$ gives the square of the magnitude of the phasor

$$\underline{J}_y\underline{J}_y^* = |\underline{J}_y|^2 \tag{4.92}$$

Hence, it is possible to express the average loss density $\langle p_d\rangle$ at a point in terms of the phasor of $J_y(t)$ as

$$\langle p_d\rangle = \frac{\underline{J}_y\,\underline{J}_y^*}{\sigma} \tag{4.93}$$

It is shown in the analysis of the infinite current sheet that the current density $\mathbf{J}$ has a nonzero component $\underline{J}_y$ in the y-direction which varies with respect to the height x. Reinserting the dependence of $\underline{J}_y$ on the height x gives

$$\langle p_d\rangle = \frac{\underline{J}_y(x)\,\underline{J}_y^*(x)}{\sigma} \tag{4.94}$$

As indicated earlier in (4.83), the integration of $\langle p_d\rangle$ from $x = 0$ to $x = h_{cu}$ yields the average power dissipated per square meter of current sheet in the y-z plane, designated as $\langle Q_J\rangle$, to match the symbol used in [13,19]. For ease of expressing the solution for the current density and the magnetic field intensity, we have introduced a variable $\mathcal{X}$ earlier in (4.40). Depending on the magnitude of the magnetic field intensity on the boundaries of the conductor, $\mathcal{X}$ is defined either as $\mathcal{X} = x$ or $\mathcal{X} = h_{cu} - x$. Instead of integrating (4.94) with respect to x, the average power dissipated in watts per square meter $\langle Q_J\rangle$ can also be obtained by integrating

$$\langle p_d\rangle = \frac{\underline{J}_y(\mathcal{X})\,\underline{J}_y^*(\mathcal{X})}{\sigma} \tag{4.95}$$

from $\chi = 0$ to $\chi = h_{cu}$. That is,

$$\begin{aligned} \langle Q_J \rangle &= \int_0^{h_{cu}} \frac{\underline{J}_y(\chi)\,\underline{J}_y^*(\chi)}{\sigma}\,d\chi \\ &= \frac{1}{\sigma}\int_0^{h_{cu}} \underline{J}_y(\chi)\,\underline{J}_y^*(\chi)\,d\chi \end{aligned} \tag{4.96}$$

To evaluate this integral, we must expand the product of the complex conjugates inside the integrand. This is done in detail in Appendix E; the results of this expansion are restated here. In order to simplify the form of the following expressions, we introduce the relationships

$$\Delta = \frac{h_{cu}}{\delta} \tag{4.97}$$

$$w = \frac{\chi}{\delta} \tag{4.98}$$

$$\begin{aligned} v &= \frac{h_{cu} - \chi}{\delta} \\ &= \Delta - w \end{aligned} \tag{4.99}$$

The variables w and v above are used simply to make the derivation given in Appendix E easier to read. The variable Δ also serves to simplify the derivation, but it has a physical interpretation that is important to understand.

Equation (4.97) above states that Δ *is the height of a winding layer in units of skin depth.* Bear in mind that the skin depth of a conducting layer depends upon the frequency of the transformer excitation. We show in the expressions below that the power dissipated and energy stored in any winding layer of a transformer is a function of the boundary values of the magnetic field intensity $\underline{H}_z(\chi = 0)$ and $\underline{H}_z(\chi = h_{cu})$, the skin depth δ of the conducting material at the excitation frequency, and Δ, the height of the layer normalized to the skin depth of the material.

This fact is important because it reminds us that it is not simply the frequency of the current in a transformer that causes the ac resistance and ac inductance effects in the device. Rather, it is the size of the conductors of the windings *relative to the skin depth of the conductive material for the particular frequency of excitation.* In other words, the so-called high-frequency effects that we are addressing in this document can occur at any excitation frequency provided the conductor size is large enough. Let us examine the case of 60-Hz power transmission lines. At 60°C, for example, the conductivity of annealed copper wire is $\sigma = 5.315 \times 10^7\,\mathrm{S/m}$. Together with $\omega = 120\pi$ and $\mu_0 = 4\pi \times 10^{-7}\,\mathrm{H/m}$, this gives a skin depth δ of 8.9 mm according to (4.7). Hence, there is a practical limit on the effectiveness of the size of conductors used in 60-Hz power transmission lines and power bus bars [21, p.201].

Returning to the integration of the average power-density function expressed by (4.96), the equation for the current density (4.51) is used in Appendix E to derive

$$
\begin{aligned}
\underline{J}_y(\chi)\underline{J}_y^*(\chi) &= \frac{|\underline{k}|^2\,|\underline{H}_z(\chi = h_{cu})|^2}{(\cosh 2\Delta - \cos 2\Delta)} \\
&\times \Big\{ (\cosh 2w + \cos 2w) \\
&+ (\alpha^2+\beta^2)(\cosh 2v + \cos 2v) \\
&- 2\alpha\Big(\cosh\Delta\cos(\Delta - 2w) + \cosh(\Delta - 2w)\cos\Delta\Big) \\
&+ 2\beta\Big(\sinh\Delta\sin(\Delta - 2w) + \sinh(\Delta - 2w)\sin\Delta\Big) \Big\}
\end{aligned} \tag{4.100}
$$

To see how the product $\underline{J}_y(\chi)\underline{J}_y^*(\chi)$ varies as a function of χ, v and w need to be eliminated from the above equation. From (4.98), we have $w = \chi/\delta$. From (4.99) we have $v = \Delta - w = \Delta - (\chi/\delta)$. So this product of $\underline{J}_y(\chi)\underline{J}_y^*(\chi)$ can be rewritten as:

$$
\begin{aligned}
\underline{J}_y(\chi)\underline{J}_y^*(\chi) &= \frac{|\underline{k}|^2\,|\underline{H}_z(\chi = h_{cu})|^2}{(\cosh 2\Delta - \cos 2\Delta)} \\
&\times \Bigg\{ \left[\cosh\left(\frac{2\chi}{\delta}\right) + \cos\left(\frac{2\chi}{\delta}\right)\right] \\
&+ \left(\alpha^2+\beta^2\right)\left[\cosh\left(2\Delta - \frac{2\chi}{\delta}\right) + \cos\left(2\Delta - \frac{2\chi}{\delta}\right)\right] \\
&- 2\alpha\left[\cosh\Delta\cos\left(\Delta - \frac{2\chi}{\delta}\right) + \cosh\left(\Delta - \frac{2\chi}{\delta}\right)\cos\Delta\right] \\
&+ 2\beta\left[\sinh\Delta\sin\left(\Delta - \frac{2\chi}{\delta}\right) + \sinh\left(\Delta - \frac{2\chi}{\delta}\right)\sin\Delta\right] \Bigg\}
\end{aligned} \tag{4.101}
$$

The details in the integration of (4.101) from $\chi = 0$ to $\chi = h_{cu}$ are shown in Appendix G, and the results are restated here:

$$
\begin{aligned}
\int_0^{h_{cu}} \underline{J}_y(\chi)\underline{J}_y^*(\chi)\,d\chi &= \frac{|\underline{k}|^2\,|\underline{H}_z(\chi = h_{cu})|^2\,\delta}{2\,(\cosh 2\Delta - \cos 2\Delta)} \\
&\times \Big\{ (1+\alpha^2+\beta^2)(\sinh 2\Delta + \sin 2\Delta) \\
&- 4\alpha(\sinh\Delta\cos\Delta + \cosh\Delta\sin\Delta) \Big\}
\end{aligned} \tag{4.102}
$$

Defining F_1 and F_2 as

$$
F_1(\Delta) = \frac{\sinh 2\Delta + \sin 2\Delta}{\cosh 2\Delta - \cos 2\Delta} \tag{4.103}
$$

$$F_2(\Delta) = \frac{\sinh\Delta\cos\Delta + \cosh\Delta\sin\Delta}{\cosh 2\Delta - \cos 2\Delta} \tag{4.104}$$

and recalling from (4.6) that $\underline{k} = (1+j)/\delta$, or $|\underline{k}|^2 = 2/\delta^2$, we can write the final result from (4.96) for the average power dissipation per square meter $\langle Q_J \rangle$ in the y-z plane as

$$\boxed{\begin{aligned} \langle Q_J \rangle &= \frac{|\underline{H}_z(\chi = h_{cu})|^2}{\sigma\delta}\left[(1+\alpha^2+\beta^2)F_1(\Delta) - 4\alpha F_2(\Delta)\right] \\ &= \frac{|\underline{H}_z(\chi = h_{cu})|^2}{\sigma\delta}\langle Q'_J(\alpha,\beta,\Delta)\rangle \end{aligned}} \tag{4.105}$$

where

$$\boxed{\langle Q'_J(\alpha,\beta,\Delta)\rangle = (1+\alpha^2+\beta^2)F_1(\Delta) - 4\alpha F_2(\Delta)} \tag{4.106}$$

These two equations essentially state the same result given by Vandelac and Ziogas in equation (A-17) of [19].

Since the functions $F_1(\Delta)$ and $F_2(\Delta)$ depend only on the parameter Δ, they are generally applicable to a winding layer of arbitrary height h_{cu} driven at an arbitrary excitation frequency ω. The plots of $F_1(\Delta)$ and $F_2(\Delta)$ are provided in Fig. 4.27. Once the conductivity σ and the frequency of excitation ω are known, the skin depth δ can be computed from (4.7). Then Δ, the height of a winding layer in units of skin depth, can be computed from h_{cu} and δ from (4.97). The functional values of F_1 and F_2 can be read directly from Fig. 4.27. Given the boundary conditions on the magnetic field intensity phasors $\underline{H}_z(\chi = 0)$ and $\underline{H}_z(\chi = h_{cu})$, the parameters α and β can be computed according to (4.48) and (4.49). With the knowledge of the parameters α and β, and the values of F_1 and F_2, $\langle Q'_J \rangle$ can be computed from (4.106). Finally, the average power dissipation per square meter $\langle Q_J \rangle$ in the y-z plane is computed according to (4.105). When Δ is large, the functions F_1 and F_2 approach to their respective limits:

$$\lim_{\Delta\to\infty} F_1(\Delta) = 1 \tag{4.107}$$

$$\lim_{\Delta\to\infty} F_2(\Delta) = 0 \tag{4.108}$$

To obtain a quick estimation of $\langle Q'_J \rangle$ in such a situation, F_1 and F_2 can be approximated by one and zero, respectively. The error introduced to $\langle Q'_J \rangle$ through such approximations is less than 10% for $\Delta \geq 2.2$ and less than 5% for $\Delta \geq 4.1$ for all values of α and β.

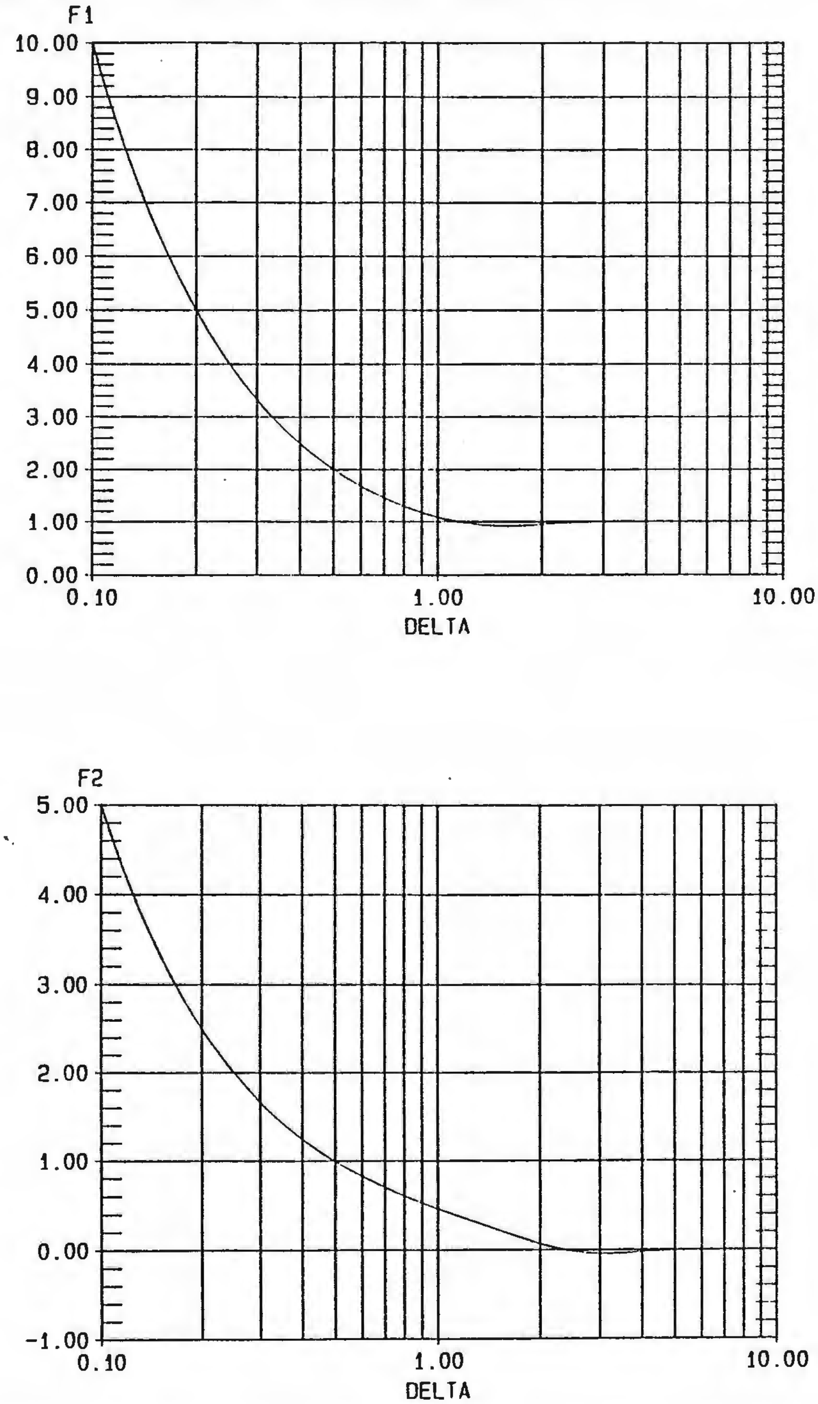

Figure 4.27: The variation of (a) F_1 and (b) F_2 with respect to Δ.

4.5.3 Average Energy Storage Per Square Meter of an Infinite Current Sheet

We can carry out a completely parallel derivation for $\langle Q_H \rangle$, the average energy stored in the magnetic field per square meter in the y-z plane. The starting point of this derivation is (4.78), which is restated here:

$$\langle w_m \rangle = \frac{1}{T}\int_T \frac{\mu_0 \, |\mathbf{H}(t)|^2}{2} \, dt \tag{4.109}$$

Since the magnetic field intensity in our model transformer has a nonzero component only in the z-direction, the above equation can be further simplified to

$$\langle w_m \rangle = \frac{1}{T}\int_T \frac{\mu_0 \, |H_z(t)|^2}{2} \, dt \tag{4.110}$$

With the excitation being sinusoidal, the magnetic field intensity $H_z(t)$ and its corresponding phasor representation $\underline{H}_z$ can be assumed to take the forms of

$$H_z(t) = \sqrt{2}\, |\underline{H}_z| \cos(\omega t + \theta_H) \tag{4.111}$$

$$\underline{H}_z = |\underline{H}_z| \, e^{j\,\theta_H} \tag{4.112}$$

where $|\underline{H}_z|$, the magnitude of $\underline{H}_z$, is also the rms value of the magnetic field intensity. It is understood that the magnetic field intensity is also a function of the height x and its dependence on x is not explicitly shown here. Substituting (4.111) into (4.110) and carrying out the integration with respect to time yields

$$\begin{aligned} \langle w_m \rangle &= \frac{1}{T}\int_T \mu_0 \, |\underline{H}_z|^2 \cos^2(\omega t + \theta_H) \, dt \\ &= \frac{\mu_0 \, |\underline{H}_z|^2}{2} \end{aligned} \tag{4.113}$$

By definition, the product of the phasor $\underline{H}_z$ and its complex conjugate $\underline{H}_z^*$ gives the square of the magnitude of the phasor $|\underline{H}_z|^2$. Hence, the average energy storage density $\langle w_m \rangle$ can be written as

$$\langle w_m \rangle = \frac{\mu_0 \, \underline{H}_z \underline{H}_z^*}{2} \tag{4.114}$$

Reinserting the dependence of $\underline{H}_z$ on the height x gives

$$\langle w_m \rangle = \frac{\mu_0 \, \underline{H}_z(x) \underline{H}_z^*(x)}{2} \tag{4.115}$$

The per cycle average of the energy stored in the magnetic field in joules per square meter of winding layer $\langle Q_H \rangle$ in the y-z plane can then be obtained by integrating $\langle w_m \rangle$ from $x = 0$ to $x = h_{cu}$

$$\begin{aligned} \langle Q_H \rangle &= \int_0^{h_{cu}} \frac{\mu_0 \underline{H}_z(x) \underline{H}_z^*(x)}{2}\, dx \\ &= \frac{\mu_0}{2} \int_0^{h_{cu}} \underline{H}_z(x) \underline{H}_z^*(x)\, dx \end{aligned} \tag{4.116}$$

Since the solution for $\underline{H}_z$ is derived earlier in terms of the variable χ, the above integration can also be carried out with respect to the variable χ for $\chi = 0$ and $\chi = h_{cu}$

$$\langle Q_H \rangle = \frac{\mu_0}{2} \int_0^{h_{cu}} \underline{H}_z(\chi) \underline{H}_z^*(\chi)\, d\chi \tag{4.117}$$

Using the same simplifying definitions for Δ, w, and v given in (4.97), (4.98), and (4.99), we show in Appendix F that the product $\underline{H}_z(\chi)\underline{H}_z^*(\chi)$ is equal to

$$\begin{aligned} \underline{H}_z(\chi)\underline{H}_z^*(\chi) &= \frac{|\underline{H}_z(\chi = h_{cu})|^2}{\cosh 2\Delta - \cos 2\Delta} \\ &\times \Bigg\{ (\cosh 2w - \cos 2w) \\ &+ (\alpha^2 + \beta^2)(\cosh 2v - \cos 2v) \\ &+ 2\alpha \Big[\cosh \Delta \cos(\Delta - 2w) - \cosh(\Delta - 2w) \cos \Delta\Big] \\ &- 2\beta \Big[\sinh \Delta \sin(\Delta - 2w) - \sinh(\Delta - 2w) \sin \Delta\Big] \Bigg\} \end{aligned} \tag{4.118}$$

From (4.98), we have $w = \chi/\delta$. From (4.99) we have $v = \Delta - w = \Delta - (\chi/\delta)$. So this product of $\underline{H}_z(\chi)\underline{H}_z^*(\chi)$ can be rewritten as:

$$\begin{aligned} \underline{H}_z(\chi)\underline{H}_z^*(\chi) &= \frac{|\underline{H}_z(\chi = h_{cu})|^2}{(\cosh 2\Delta - \cos 2\Delta)} \\ &\times \Bigg\{ \left[\cosh\left(\frac{2\chi}{\delta}\right) - \cos\left(\frac{2\chi}{\delta}\right)\right] \\ &+ \left(\alpha^2 + \beta^2\right)\left[\cosh\left(2\Delta - \frac{2\chi}{\delta}\right) - \cos\left(2\Delta - \frac{2\chi}{\delta}\right)\right] \\ &+ 2\alpha\left[\cosh \Delta \cos\left(\Delta - \frac{2\chi}{\delta}\right) - \cosh\left(\Delta - \frac{2\chi}{\delta}\right) \cos \Delta\right] \\ &- 2\beta\left[\sinh \Delta \sin\left(\Delta - \frac{2\chi}{\delta}\right) - \sinh\left(\Delta - \frac{2\chi}{\delta}\right) \sin \Delta\right] \Bigg\} \end{aligned} \tag{4.119}$$

The details in the integration of the above equation from $\mathcal{X} = 0$ to $\mathcal{X} = h_{cu}$ are shown in Appendix H, and the results are repeated here for convenience:

$$\begin{aligned}\int_0^{h_{cu}} \underline{H}_z(\mathcal{X})\underline{H}_z^*(\mathcal{X})\, d\mathcal{X} &= \frac{|\underline{H}_z(\mathcal{X} = h_{cu})|^2\, \delta}{2\,(\cosh 2\Delta - \cos 2\Delta)} \\ &\quad \times \Big\{ (1 + \alpha^2 + \beta^2)(\sinh 2\Delta - \sin 2\Delta) \\ &\quad - 4\alpha(\sinh\Delta\cos\Delta - \cosh\Delta\sin\Delta) \Big\} \qquad (4.120)\end{aligned}$$

To help visualizing the dependence of $\langle Q_H \rangle$, the per cycle average of the energy storage per square meter in the y-z plane, on the variable Δ, we define F_3 and F_4 as

$$F_3(\Delta) = \frac{\sinh 2\Delta - \sin 2\Delta}{\cosh 2\Delta - \cos 2\Delta} \qquad (4.121)$$

$$F_4(\Delta) = \frac{\sinh\Delta\cos\Delta - \cosh\Delta\sin\Delta}{\cosh 2\Delta - \cos 2\Delta} \qquad (4.122)$$

Substituting (4.120), (4.121), and (4.122) into (4.117), we can write the final result for the per cycle average of the energy storage per square meter in the y-z plane $\langle Q_H \rangle$ as,

$$\boxed{\begin{aligned}\langle Q_H \rangle &= \frac{\mu_0 \delta |\underline{H}_z(\mathcal{X} = h_{cu})|^2}{4} \left[(1 + \alpha^2 + \beta^2)F_3(\Delta) - 4\alpha F_4(\Delta)\right] \\ &= \frac{\mu_0 \delta |\underline{H}_z(\mathcal{X} = h_{cu})|^2}{4} \langle Q'_H(\alpha, \beta, \Delta)\rangle\end{aligned}} \qquad (4.123)$$

where

$$\boxed{\langle Q'_H(\alpha,\beta,\Delta)\rangle = (1 + \alpha^2 + \beta^2)F_3(\Delta) - 4\alpha F_4(\Delta)} \qquad (4.124)$$

The plots of the two functions $F_3(\Delta)$ and $F_4(\Delta)$ are provided in Fig. 4.28. Once the conductivity σ and the frequency of excitation ω are known, the skin depth δ can be computed from (4.7). Then Δ, the height of a winding layer in units of skin depth, can be computed from h_{cu} and δ from (4.97). The functional values of F_3 and F_4 can be read directly from Fig. 4.28. Given the boundary conditions on the magnetic field intensity phasors $\underline{H}_z(\mathcal{X} = 0)$ and $\underline{H}_z(\mathcal{X} = h_{cu})$, the parameters α and β can be computed according to (4.48) and (4.49). With the knowledge of the parameters α and β, and the values of F_3 and F_4, $\langle Q'_H \rangle$ can be computed from (4.124). Finally, the average energy

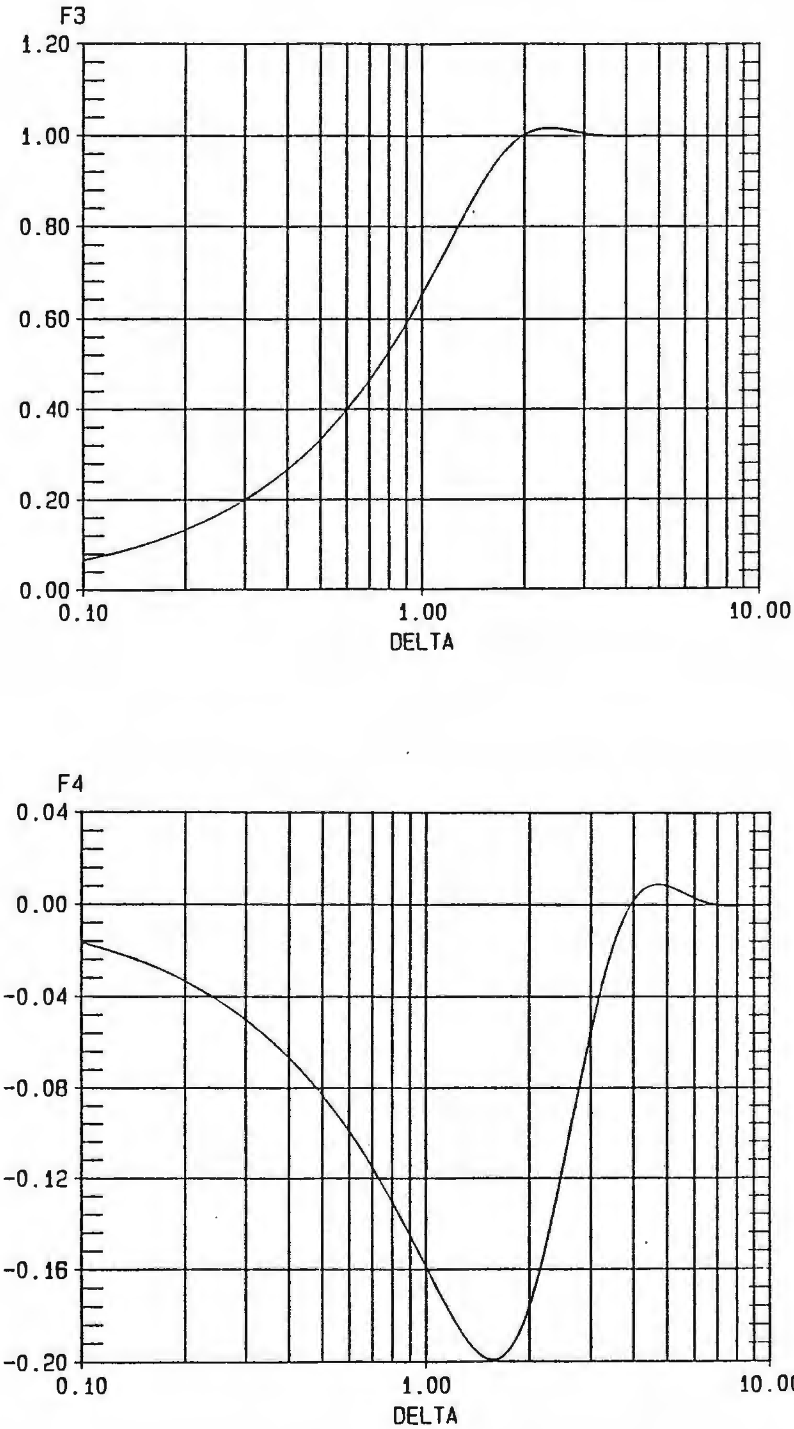

Figure 4.28: The variation of (a) F_3 and (b) F_4 with respect to Δ.

storage per square meter $\langle Q_H \rangle$ in the y-z plane is computed according to (4.123). Similar to F_1 and F_2, the functions F_3 and F_4 approach to the limiting values of

$$\lim_{\Delta \to \infty} F_3(\Delta) = 1 \tag{4.125}$$

$$\lim_{\Delta \to \infty} F_4(\Delta) = 0 \tag{4.126}$$

To obtain a quick estimation of $\langle Q'_H \rangle$ in such a situation, F_3 and F_4 can be approximated by one and zero, respectively. The error introduced to $\langle Q'_H \rangle$ through such approximations is less than 10% for $\Delta \geq 3.1$ and less than 5% for $\Delta \geq 3.4$ for all values of α and β.

4.6 SUMMARY OF THE FIELD SOLUTION FOR AN INFINITE CURRENT SHEET

4.6.1 Introduction of Layer Porosity η Into the Equations

Before making further use of the equations derived in this chapter, we should pause to restate some of the underlying assumptions that limit their domain of application. In Chapters 1 through 3, we make a series of simplifying assumptions concerning the structure of a transformer that eventually lead us to the infinite current sheet model of this chapter. These assumptions and their resulting implications may be summarized as follows :

1. Assume that the discrete conductors that make up the transformer windings may be modeled by an equivalent foil that entirely fills the window breadth.
   Implications: Layer porosity must be introduced, and each layer may now be treated as a one-turn solenoid.
2. Assume that the transformer has a pot core of infinite magnetic permeability.
   Implications: Only the leakage flux due to finite conductor thickness and finite interlayer gaps appears in the model, and we may now treat the solenoid that models a winding layer as an infinite solenoid.
3. Assume for the purpose of field solution that a small portion of the surface of an infinite solenoid may be modeled by a flat sheet of conductor that extends infinitely in both the breadth and the depth directions.
   Implications: The calculation of the fields is greatly simplified, but the validity of the resulting equations is limited by the curvature in the windings of the transformer to be modeled.

It is important to note that the infinite current sheet model that is obtained from assumption 3 above is for the purpose of obtaining the field solution *only*, and the equations that result from this model are to be used in conjunction with the model of assumption 2. However, before applying the equations of this chapter to a physical transformer, we must incorporate the concept of layer porosity. In Section 2.2.1.3, we argue that the introduction of layer porosity as a multiplicative factor insures that the dc resistance of the model winding is the same as that of the original winding that it replaces. This multiplicative factor appears as an effective decrease in conductivity. Based upon equation (2.2), we can define an effective conductivity σ_{eff} as

$$\sigma_{\mathit{eff}} = \eta\sigma \tag{4.127}$$

Thus, we can incorporate the layer porosity into the equations of this chapter simply by using the numerical value of σ_{eff} as determined by (4.127) instead of the intrinsic conductivity of the conductors. In the next section, we restate all of the significant equations of this chapter, and incorporate the use of σ_{eff} wherever appropriate.

4.6.2 Restatement of Significant Equations

Using the definition of effective conductivity σ_{eff} given in (4.127), we can restate the significant equations derived in this chapter as follows:

The complex wave number $\underline{k}$ is given by

$$\boxed{\underline{k} \approx \sqrt{j\omega\mu_o\sigma_{\mathit{eff}}}} \tag{4.128}$$

The skin depth δ is given by

$$\boxed{\delta = \sqrt{\frac{2}{\omega\mu_o\sigma_{\mathit{eff}}}}} \tag{4.129}$$

The magnetic-field-intensity and current-density phasor distributions across the height of a layer are given by

$$\boxed{\underline{H}_z(x) = \frac{1}{\sinh \underline{k}h_{cu}}\left[\underline{H}_z(h_{cu}) \sinh \underline{k}x + \underline{H}_z(0) \sinh \underline{k}(h_{cu} - x)\right]} \tag{4.130}$$

$$\boxed{\underline{J}_y(x) = \frac{-\underline{k}}{\sinh \underline{k}h_{cu}}\left[\underline{H}_z(h_{cu}) \cosh \underline{k}x - \underline{H}_z(0) \cosh \underline{k}(h_{cu} - x)\right]} \tag{4.131}$$

or, if we define χ as

$$\chi = \begin{cases} x & \text{if } |\underline{H}_z(x = h_{cu})| \geq |\underline{H}_z(x = 0)| \\ h_{cu} - x & \text{if } |\underline{H}_z(x = h_{cu})| < |\underline{H}_z(x = 0)| \end{cases} \tag{4.132}$$

and $\underline{\Gamma}$ as

$$\underline{\Gamma} = \alpha + j\beta = \frac{\underline{H}_z(\mathcal{X} = 0)}{\underline{H}_z(\mathcal{X} = h_{cu})} \tag{4.133}$$

then we can rewrite the distributions of (4.130) and (4.131) as

$$\boxed{\underline{H}_z(\mathcal{X}) = \frac{\underline{H}_z(\mathcal{X} = h_{cu})}{\sinh \underline{k} h_{cu}} \Big[\sinh \underline{k}\mathcal{X} + (\alpha + j\beta) \sinh \underline{k}(h_{cu} - \mathcal{X})\Big]} \tag{4.134}$$

$$\boxed{\underline{J}_y(\mathcal{X}) = \frac{(-1)^{\varepsilon}\, \underline{k}\, \underline{H}_z(\mathcal{X} = h_{cu})}{\sinh \underline{k} h_{cu}} \Big[\cosh \underline{k}\mathcal{X} - (\alpha + j\beta) \cosh \underline{k}(h_{cu} - \mathcal{X})\Big]} \tag{4.135}$$

where

$$\varepsilon = \begin{cases} 1 & \text{if } |\underline{H}_z(x = h_{cu})| \ \geq \ |\underline{H}_z(x = 0)| \\ 0 & \text{if } |\underline{H}_z(x = h_{cu})| \ < \ |\underline{H}_z(x = 0)| \end{cases} \tag{4.136}$$

If we define Δ as

$$\Delta = \frac{h_{cu}}{\delta} \tag{4.137}$$

and F_1,F_2,F_3 and F_4 as

$$F_1(\Delta) = \frac{\sinh 2\Delta + \sin 2\Delta}{\cosh 2\Delta - \cos 2\Delta} \tag{4.138}$$

$$F_2(\Delta) = \frac{\sinh \Delta \cos \Delta + \cosh \Delta \sin \Delta}{\cosh 2\Delta - \cos 2\Delta} \tag{4.139}$$

$$F_3(\Delta) = \frac{\sinh 2\Delta - \sin 2\Delta}{\cosh 2\Delta - \cos 2\Delta} \tag{4.140}$$

$$F_4(\Delta) = \frac{\sinh \Delta \cos \Delta - \cosh \Delta \sin \Delta}{\cosh 2\Delta - \cos 2\Delta} \tag{4.141}$$

then we can use (4.134) and (4.135) above to write the average power dissipation per square meter in the y-z plane as

$$\boxed{\begin{aligned} \langle Q_J \rangle &= \frac{|\underline{H}_z(\mathcal{X} = h_{cu})|^2}{\sigma_{\mathit{eff}}\, \delta} \Big[(1 + \alpha^2 + \beta^2) F_1(\Delta) - 4\alpha F_2(\Delta)\Big] \\ &= \frac{|\underline{H}_z(\mathcal{X} = h_{cu})|^2}{\sigma_{\mathit{eff}}\, \delta} \langle Q'_J(\alpha, \beta, \Delta) \rangle \end{aligned}} \tag{4.142}$$

where

$$\boxed{\langle Q'_J(\alpha,\beta,\Delta)\rangle = (1+\alpha^2+\beta^2)F_1(\Delta) - 4\alpha F_2(\Delta)} \tag{4.143}$$

Likewise, the average energy storage per square meter in the y-z plane is given by

$$\begin{aligned} \langle Q_H\rangle &= \frac{\mu_0\delta|\underline{H}_z(\mathcal{X}=h_{cu})|^2}{4}\left[(1+\alpha^2+\beta^2)F_3(\Delta) - 4\alpha F_4(\Delta)\right] \\ &= \frac{\mu_0\delta|\underline{H}_z(\mathcal{X}=h_{cu})|^2}{4}\langle Q'_H(\alpha,\beta,\Delta)\rangle \end{aligned} \tag{4.144}$$

where

$$\boxed{\langle Q'_H(\alpha,\beta,\Delta)\rangle = (1+\alpha^2+\beta^2)F_3(\Delta) - 4\alpha F_4(\Delta)} \tag{4.145}$$

The above equations, together with the assumptions and the derivations that have produced them, form the mathematical framework for the modeling of a multiwinding transformer for high-frequency applications. Using these equations, we are now in a position to obtain expressions for the short-circuit impedances that exist between two windings of a multiwinding transformer.

RIDLEY WORKS®

Nothing Compares

www.ridleyworks.com

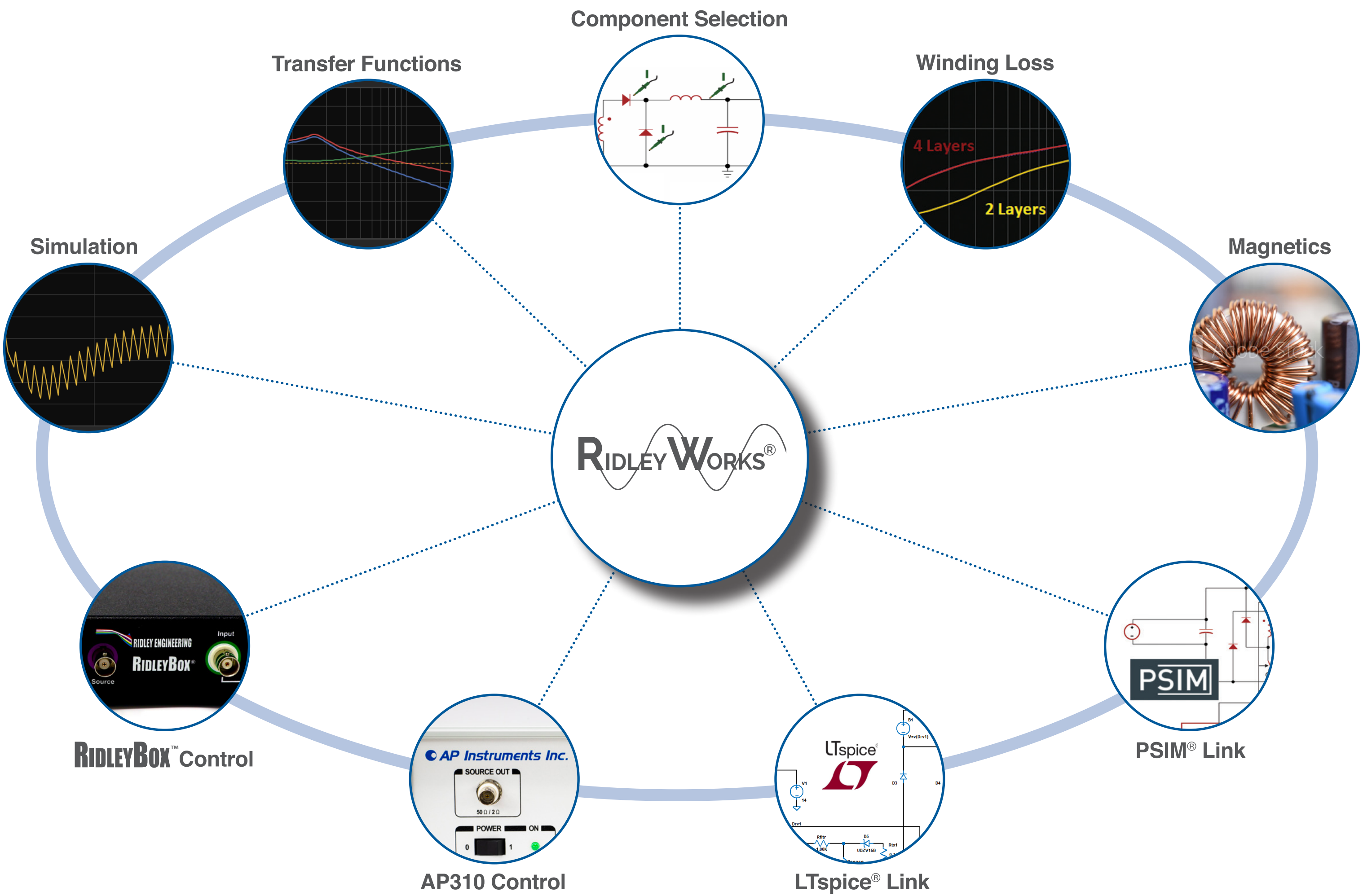
Component Selection
Transfer Functions
Winding Loss
4 Layers
2 Layers
Simulation
Magnetics
RidleyWorks®
RidleyBox™ Control
PSIM® Link
AP310 Control
LTspice® Link
AP Instruments Inc.
SOURCE OUT
POWER
ON
RIDLEY ENGINEERING
RidleyBox®
Input
Source
PSIM
LTspice